

COMPUTATIONAL IMAGING USING ELECTROMAGNETIC OPTICS

by

ANURAG SATISH AGRAWAL

B.Tech., Indian Institute of Technology Delhi, 2006

M.S., University of Colorado Boulder, 2010

A thesis submitted to the
Faculty of the Graduate School of the
University of Colorado in partial fulfillment
of the requirement for the degree of
Doctor of Philosophy
Department of Electrical Engineering
2014

This thesis entitled:
Computational Imaging using Electromagnetic Optics
written by Anurag Satish Agrawal
has been approved for the Department of Electrical, Computer and Energy Engineering

(Rafael Piestun)

(Robert Mcleod)

Date_____

The final copy of this thesis has been examined by the signatories, and we
Find that both the content and the form meet acceptable presentation standards
Of scholarly work in the above mentioned discipline.

Agrawal, Anurag Satish (Ph.D., Electrical, Computer and Energy Engineering)

Computational Imaging using Electromagnetic Optics

Thesis directed by Professor Rafael Piestun

Modern optical imaging systems make extensive use of computational power for analog pre-processing, analog to digital conversion and digital post-processing. The joint design of these elements can be used to optimize the information throughput of optical imaging systems. This paradigm, termed computational optical imaging, aims at optimizing the output of optical systems in the form of imaging metrics, multidimensional imaging, feature detection, compressive sensing, etc. However, most optical imaging systems rely on the scalar wave theory of light to analyze these modern systems. Light, being an electromagnetic wave is vectorial in nature leading to significant errors in the scalar model when the propagation medium is anisotropic, inhomogeneous or non-linear. Electromagnetic optics, on the other hand, is an all-encompassing theory of light in the classical limit that takes into account the coupled nature of electric and magnetic fields.

In this respect, the effects of anisotropic emission from a fixed dipole emitter on high numerical aperture super-resolution microscopy are investigated. Wide field microscope configurations that allow simultaneous acquisition and measurement of the 3D position and orientation parameters of multiple fixed dipole emitters are proposed. The performance limits of these systems for the 5D imaging of fixed dipole emitters are quantified through comparison of the Cramer-Rao lower bounds in a photon limited environment. Further, experimental validation is provided for simultaneously estimating the 5D dipole parameters using the double-helix phase mask. Binary multi-level fabrication of efficient phase modulation elements to engineer the Green's tensor response of the system to a dipole input is demonstrated.

High numerical aperture objectives give rise to steep incident angles on lens surfaces, leading to resolution losses in imaging systems due to aberrations caused by the incorrect assumption of linearity between the incident and refracted angles at material interfaces. A new paradigm, termed infinitely refraction-linear artificial material (IRAM), is proposed to tackle this problem. IRAM maintain the linear relationship between incident and refracted angles beyond the paraxial limit. The inherent anisotropic material parameter requirements for IRAM are summarized. The performance of IRAM lenses is compared to that of conventional isotropic lenses by simulating the diffraction limited spot size of these lenses in Zemax. It is shown that with proper design IRAMs have the potential to improve the resolution of optical imaging systems. Further, another class of artificial metamaterials that use magnetic resonance to realize exotic optical properties is discussed as candidates for super-resolution using the super-lensing effect.

This thesis is dedicated to

My Parents (Satish and Jayshree)

My Wife (Debolina)

My siblings (Neelam and Aniket)

Acknowledgements

First and foremost I would like to express my sincere gratitude to my advisor Prof. Rafael Piestun for the continuous support of my doctoral study and research, for his patience, motivation, enthusiasm, and immense knowledge. He has always inspired me to work independently while providing the necessary support and guidance at every step. I have learnt lots of things about “optical imaging science” and “life in general” from him. The most important of which is to keep calm and work on.

I would also like to acknowledge the thesis committee members Dr. Wounjhang Park, Dr. Robert Mcleod, Dr. Kelvin Wagner, and Dr. Ivan Smalyukh for taking the time to supervise my dissertation and for all the helpful discussions over the years. My undergraduate professors at IIT Delhi introduced me to optical sciences and I am grateful towards them for doing so.

Research can be carried out in an uninterrupted and effective manner if it is supported by funding sources. I thankfully acknowledge support from NSF awards (DBI-0852885, ECCS-1028714) and DARPA award BAA-11-26. During the course of my research I have had a few important collaborations that I would like to mention. The work on aperiodic metamaterials was done in collaboration with Prof. Wounjhang Park. The single-molecule experiments were performed in collaboration with Prof. W.E. Moerner’s group at Stanford. The IRAM work was done in collaboration with Edward Dowski, Ascentia Imaging. I would also like to thank Aubrey Shapero, an NNIN-REU intern for his valuable contribution towards phase mask fabrication.

My experience at University of Colorado, Boulder was enriched by the interactions with extremely talented but humble colleagues. The senior members of Rafael’s group Pavani Prasanna, Tim Gerke, and Jer Brown helped me get familiarized with the research environment.

My experience working with Sean Quirin and Ginni Sharma was extremely rewarding. I would also like to thank other members of Rafael's group Don, Tony, Antonio, Liang and Haiyan for their valuable feedback of my work.

I came to Boulder in 2006 and during these 8 years, I have made some really good friends within whose company the experience of living in a foreign country was made comfortable and enjoyable. I would like to take this opportunity to thank them all.

My family has always been the biggest supporters of my career and I thank them for selflessly fulfilling my every need including financial support during my initial years at University of Colorado Boulder. A special thanks to my uncle Dinesh Agrawal who has been my role model. Last, but not the least I would like to thank my best friend and my wife Debolina. Thank you for supporting me all these years and for years to come. This would not have been possible without you.

Table of contents

Acknowledgements	vi
Table of contents	viii
Table of Figures.....	xi
Chapter 1 Introduction.....	1
<i>1.1 Historical perspective of imaging.....</i>	<i>3</i>
<i>1.2 Electromagnetic Optics.....</i>	<i>8</i>
<i>1.3 Motivation and main contributions.....</i>	<i>12</i>
Chapter 2 5D imaging: 3D localization and orientation estimation of single- molecules.....	16
<i>2.1 Introduction.....</i>	<i>16</i>
<i>2.2 Optical system model and analysis.....</i>	<i>19</i>
<i>2.3 Cramer-Rao Lower Bound.....</i>	<i>26</i>
<i>2.4 Experimental validation using a double-helix mask.....</i>	<i>37</i>
<i>2.5 Engineering the Green's tensor using a spiral (vortex) phase mask.....</i>	<i>48</i>
<i>2.6 Conclusion and Outlook</i>	<i>53</i>
<i>Appendix 2A Localization of Isotropic emitter vs. Point emitter</i>	<i>53</i>
Chapter 3 Phase masks as a diffractive optical element (DOE)	58
<i>3.1 Introduction.....</i>	<i>58</i>
<i>3.2 Diffraction efficiency of DOE.....</i>	<i>59</i>

3.3 Alignment of binary masks.....	61
3.4 Fabrication of the phase mask.....	62
3.5 Fabricated mask testing.....	66
3.6 Conclusion	68
Chapter 4 Negative Permeability with Arrays of Aperiodic Silver Nanoclusters	69
4.1 Introduction.....	69
4.2 Requirements for negative refractive index.....	69
4.3 Design of the aperiodic metamaterial.....	70
4.4 Effective parameter calculation.....	73
4.5 Performance comparison of periodic and aperiodic structures.....	77
4.6 Perturbation analysis.....	78
4.7 Steady state field distributions.....	80
4.8 Conclusion	81
Chapter 5 Infinitely-Refractive Linear material (IRAM): a new optical design paradigm for non-paraxial imaging.....	83
5.1 Introduction.....	83
5.2 Gaussian Approximation	84
5.3 IRAM theory.....	90
5.4 Uniaxial crystals as PLRM.....	95
5.5 Conclusion	108

<i>Appendix 5A Properties of Uniaxial Crystals.....</i>	<i>108</i>
<i>Appendix 5B Curved Uniaxial surfaces as IRAM.....</i>	<i>113</i>
<i>Appendix 5C Calcite as an IRAM.....</i>	<i>119</i>
<i>Appendix 5D IRAM implementation using Chiral materials.....</i>	<i>122</i>
Chapter 6 Conclusion and Outlook.....	127
Bibliography	130

Table of Figures

Fig. 1.1 Schematic of a modern computational optical imaging system: It generally consists of controlled illumination; spherical/aspherical lenses; SLM, phase masks, holograms, etc. for signal modulation; detector and a signal processing and reconstruction unit. The goal of a modern system is to jointly optimize all these components to increase its information throughput. The optimization can be either active or passive depending on the application..... 1

Fig. 1.2 Far-field super-resolution: Conventional image vs. super-resolved image. The figure shows the working of far-field super-resolution system where sparse subsets are imaged separately and later combined to form an image that is not limited by diffraction. Also shown on the bottom left is the image using a conventional microscope. 6

Fig. 1.3 PSF engineering: The figure shows the PSF for the standard and non-standard apertures as the point object is defocused within a 1 micron depth range. The standard aperture's PSF is the well-known airy-disc that blurs with defocus. Astigmatism introduces asymmetry in the transverse focus. Introduction of the double-helix phase mask causes the PSF to split into two symmetric lobes that rotate as a function of defocus. The cubic phase is used to extend the depth of field by creating a PSF that remains constant with defocus. 8

Fig. 1.4 (a) Shows the electromagnetic spectrum ranging from very low frequency ($\sim 10^3$ Hz) to gamma rays (10^{21} Hz). Optical frequency covers a small region of this spectrum with wavelengths ranging from the infrared (10^{12} Hz) to the ultra-violet (10^{16} Hz). Visible light covers wavelength ranges from $\sim 200\text{nm}$ to $\sim 800\text{nm}$ (b) Shows the various theories of optics in a Venn diagram. Ray Optics is an approximation of Wave Optics which is the scalar approximation of Electromagnetic Optics..... 9

Fig. 2.1 Point Spread Function Engineering versus Green’s tensor engineering: (a) The PSF is the response of the system to a point source whereas the Green’s tensor is the response of the system to a dipole input. The output of the Green’s tensor system is a vector function of the dipole orientation. Each of the rows, shown at the output, corresponds to a unique dipole orientation, showing the total intensity and the intensity of two transverse orthogonal components of the electric field. (b) The position and orientation of a dipole with respect to an objective lens defines the input space. The origin (0,0,0) is at the focal point of the objective lens with the z-axis parallel to the optical axis. Here (x_0, y_0, z_0) represent the position of the dipole and (Θ, Φ) represent the polar and azimuthal orientation angles respectively..... 19

Fig. 2.2 Simulation of the dipole spread function along three representative orientations: I is the detected total Intensity (single channel system), $|E_x|^2$, $|E_y|^2$, $|E_1|^2$, and $|E_2|^2$ (left to right) correspond to images obtained in two-channel systems when using either orthogonal polarizers ($|E_x|^2$, $|E_y|^2$) or a quarter waveplate with orthogonal polarizer (see text for details), whereas $|E_x^{DH}|^2$ and $|E_y^{DH}|^2$ represent the intensity distributions of the two orthogonal linear polarizations using the double-helix phase mask (DH). In (a), the dipole is at the focal plane, while in (b) it is located $0.2 \mu\text{m}$ from the focal plane. The dipole is oriented along (from top to bottom) \hat{y} ($\Theta=90^\circ, \Phi=90^\circ$), \hat{z} ($\Theta=0^\circ, \Phi=0^\circ$) and $\Theta=45^\circ, \Phi=45^\circ$ 22

Fig. 2.3 Schematic of the systems considered for dipole location and orientation estimation: (a) A traditional microscope system with a signal processing unit for Green’s function engineering. Category A shows three signal processing units that focus at the same plane whereas Category B shows the three signal processing units that focus at two different planes leading to a bifocal system. Parts (b) and (e), represent systems that measures the total intensity, parts (c) and (f) represent systems with two orthogonal polarization channels, imaging

the intensities $|E_x|^2$ and $|E_y|^2$ separately, and parts (d) and (g) represent the systems with two polarization channels imaging the intensities of the elliptical polarizations components, $(|E_x+iE_y|^2)/2$ and $(|iE_x+E_y|^2)/2$ separately. (h) Shows the linear polarization system with a double-helix phase mask in the Fourier plane. (i) Shows the five dipole orientations used to compare these six systems on a unit sphere. TL - tube lens, L1, L2 -relay lenses, OL1 - objective lens, DM – dichroic mirror, PBS – polarizing beam splitter, QWP – Quarter wave plates with fast axis along 45° from x-axis..... 24

Fig. 2.4 Flowchart for calculating the Fisher Information matrix, Cramer-Rao lower bounds and standard deviation for a general imaging system consisting of a single channel or polarization-sensitive system with multiple channels..... 29

Fig. 2.5 Estimation error bounds as a function of defocus: (a) Average of volume localization - $\sigma_{3D}(4\pi/3 \cdot \sigma_x \cdot \sigma_y \cdot \sigma_z)$ (b) Average of Solid angle error - $\sigma_\Omega(\sin \Theta \cdot \sigma_\Theta \cdot \sigma_\Phi)$ for the five representative dipole orientations with respect to the axial position of the dipole. For the bifocal systems, the two focal planes were offset by $0.4 \mu\text{m}$ and the x -axis represents the center of the two planes. The legends represent the systems compared here, namely single measurement-total intensity (TI np: solid blue), linear polarization (Lin pol: green o), elliptical polarization (Elp pol: red dash-dot), bi-focal total intensity (Bf-TI np: solid cyan), bi-focal with linear polarization (Bf-Lin pol: magenta dash), bi-focal with elliptical polarization (Bf-Elp pol: yellow +), and linear polarization system that used a double helix phase mask in the Fourier plane (PS-DH-Lin pol: black Δ). 33

Fig. 2.6 Estimation error bounds as a function of dipole orientation angle: (a) Volume localization - $\sigma_{3D}(4\pi/3 \cdot \sigma_x \cdot \sigma_y \cdot \sigma_z)$ and (b) Solid angle error - $\sigma_\Omega(\sin \Theta \cdot \sigma_\Theta \cdot \sigma_\Phi)$ as a function of the azimuthal angle Φ (top row) and polar angle Θ (bottom plot). For the plots of category A,

where system collects information from a single focal plane chosen at a defocus $z_0 = 0.1\mu\text{m}$. For plot against Φ the angle $\Theta = 90^\circ$ and for the plots against Θ the angle Φ was chosen to be 0° . For the bifocal systems, the two focal planes were offset by $0.4\mu\text{m}$ and the x -axis represents the center of the two planes. The legends represent the systems compared here, namely single measurement- total intensity (TI np: solid blue), linear polarization (Lin pol: green o), elliptical polarization (Elp pol: red dash-dot), bi-focal total intensity (Bf-TI np: solid cyan), bi-focal with linear polarization (Bf-Lin pol: magenta dash), bi-focal with elliptical polarization (Bf-Elp pol: yellow +), and linear polarization system that used a double helix phase mask in the Fourier plane (PS-DH-Lin pol: black Δ). 35

Fig. 2.7 3D localization and orientation estimation design via the *CRLB*: Parts (a) and (c) show the volume localization lower bound- $\sigma_{3D}(4\pi/3 \cdot \sigma_x \cdot \sigma_y \cdot \sigma_z)$. Parts (b) and (d) show the solid angle lower bound error - $\sigma_\Omega(\sin \Theta \cdot \sigma_\Theta \cdot \sigma_\Phi)$ as a function of the polar angle Θ and defocus (z_0). Each system considered here is represented by a unique color and for each system (color), the two surface plots represent the maximum and the minimum error calculated over all azimuthal angles Φ . The systems compared in the above plots are the single channel total intensity system (TI np: blue surface), Linear polarization system (Lin Pol: green surface), bifocal linear polarization system (Bf-Lin Pol: red surface), bifocal elliptical polarization system (Bf-Elp Pol: brown surface), linear polarization with the DH mask (PS-DH: yellow surface), and the DH system for the isotropic emitter (Iso-DH: cyan surface). For the bifocal system, the two focal planes are separated by the distance $dz=0.4 \mu\text{m}$ and z_0 represents the center of the two planes. 37

Fig. 2.8 DH-PSF imaging system. (A) $4f$ optical system schematic, where IIP is the intermediate image plane formed by a standard inverted microscope, L1 and L2 are focal-length-

matched achromatic lenses, DH-PSF PM is the DH-PSF phase mask, and IP is the resulting image plane that is recorded on an EMCCD camera. The sample for the experiments described consisted of DCDHF-N-6 molecules (middle inset) embedded in a thin layer of PMMA (left inset). Orientation angles (Θ , Φ) are defined in the right inset and have ranges $[0, 90^\circ]$ and $[-180, 180^\circ]$, respectively. (B) The high efficiency dual-polarization detection DH-PSF setup used for these experiments (inverted microscope omitted for simplicity). The collected fluorescence is split by a polarizing beamsplitter (PBS) into reflected (R, blue) and transmitted (T, red) channels. Input Cartesian unit vectors $(\hat{x}_{input}, \hat{y}_{input})$ define molecular orientation (Θ , Φ) and are propagated differently through the various reflections in the two polarization channels $((\hat{x}_R, \hat{y}_R)$ and (\hat{x}_T, \hat{y}_T)). The two electric field polarization axes \bar{E}_R and \bar{E}_T are projected identically onto the phase mask (inset). The inset shows how each polarization axis (blue and red arrows) is oriented relative to the mask's axis of phase discontinuities (dashed orange) when the mask is upright (i; polarization perpendicular to discontinuities) and rotated (ii; polarization parallel to discontinuities). (C-D) Two side-on views of the SLM portion of the setup, showing the square pyramidal mirror (figure extracted from [45])..... 39

Fig. 2.9 Lower bound of the precision (standard deviation) for estimating the azimuthal angle (σ_ϕ), polar angle (σ_θ), and the 3D position (σ_{3D}) w.r.t to the polar angle theta (Θ). Blue solid curves represent the standard PSF case and dashed red curves represent the DH case. The plots on the left are shown for zero background whereas the ones on the right have background of 5 photons per pixel. The standard PSF case is defocused by 100nm, and the DH case is in focus. The polar angle in both cases is $\Phi=45^\circ$ 41

Fig. 2.10 Lower bound of the precision (standard deviation) for estimating the azimuthal angle (σ_ϕ) polar angle (σ_θ), and the 3D position (σ_{3D}) w.r.t to defocus (z_0) for a dipole oriented along (A) $\Theta=90^\circ$, $\Phi=90^\circ$ and (B) $\Theta=45^\circ$, $\Phi=45^\circ$. Blue solid curves represent the standard PSF case and dashed red curves represent the DH case. The plots on the left are shown for zero background whereas the ones on the right have background of 5 photons per pixel. 43

Fig. 2.11 Surface plots showing the lower bound of the precision (standard deviation) for estimating the 3D position (σ_{3D}) and solid angle (σ_Ω) w.r.t to defocus (z_0) and is polar angle (Θ). (A) Zero background noise. (B) Background of 5 photons/pixel. Blue surfaces represent the standard clear aperture system whereas the green surfaces represent the 4-channel double helix system used for this experiment..... 44

Fig. 2.12 Orientation fitting results for example molecule 1 (left column) and example molecule 2 (right column). All scale bars 1 μm . (A) Four example DH-PSF images (which constitute one measurement of orientation) of molecule 1 at $z \approx -250$ nm as it appears in each of four mask orientation/polarization channel combinations: parallel/transmitted (red), perpendicular/ transmitted (gold), parallel/reflected (green), and perpendicular/reflected (blue). Note that only one lobe is easily visible in the red and gold channels. (B) The transmitted (top) and reflected (bottom) polarization defocused standard PSF images used for independent orientation measurement. (C) The equivalent of (A) for example molecule 2 at $z \approx 0$ nm. (D) The equivalent of (B) for example molecule 2. (E-F) Each measurement of LD (scatter) and the predicted LD based on the mean fit orientation (solid) for each molecule. (G-H) Each measurement of LA in each channel (color code same as in A) and the overlaid predicted LA for the mean fit orientation. (I-J) Histograms of Θ and Φ extracted from DH-PSF based measurements. Magenta line is Gaussian fit, which gives mean values ($\Theta_{DH-PSF} = 42^\circ \pm 12^\circ$, Φ_{DH-

$_{PSF} = -76^\circ \pm 7^\circ$) (error is S.D.) for molecule 1 and ($\Theta_{DH-PSF} = 61^\circ \pm 2^\circ$, $\Phi_{DH-PSF} = 141^\circ \pm 4^\circ$) for molecule 2. Purple arrow denotes orientation extracted from defocused imaging: ($\Theta_{defocus} = 40^\circ \pm 2^\circ$, $\Phi_{defocus} = -81^\circ \pm 4^\circ$) for molecule 1 and ($\Theta_{defocus} = 63^\circ \pm 3^\circ$, $\Phi_{defocus} = 143^\circ \pm 5^\circ$) for molecule 2 (figure extracted from [45])..... 47

Fig. 2.13 Simulation of PSF of a spiral (vortex) phase mask: (a) Phase of the spiral phase mask. (b) PSF of the spiral phase as a function of defocus. 49

Fig. 2.14 Simulation of the dipole spread function along three representative orientations using Vortex phase mask: (I) is the detected total Intensity (single channel system), $|Ex|^2$, $|Ey|^2$, (left to right) correspond to images obtained in two-channel systems when using orthogonal polarizers. In (a), the dipole is at the focal plane, while in (b) it is located $0.2 \mu\text{m}$ from the focal plane. The dipole is oriented along (from top to bottom) \hat{z} ($\Theta=0^\circ \Phi=0^\circ$), $\Theta=45^\circ \Phi=45^\circ$, and \hat{y} ($\Theta=90^\circ \Phi=90^\circ$)..... 50

Fig. 2.15 Estimation error bounds for the vortex phase mask: The figure shows the lower bound of the standard deviation for the vortex phase mask (dashed red), DHPSF (dot-dashed green) and the two channel linear polarization system (solid blue). The top row represents the error bounds as a function of defocus and the bottom row shows them as a function of polar angle Θ . The left column is the average of the volume standard deviation along the five representative orientations shown in Fig. 2.3(i). The right column is the solid angle standard deviation..... 51

Fig. 2.16 Surface plots of the error bounds for vortex phase mask and DHPSF: The plot shows the volume (left) and solid angle standard deviation for vortex phase mask and DHPSF as a function of polar angle (Θ) and defocus (z_0)..... 52

Fig. 2.17 Experimental images using the vortex phase mask: The experimental setup is similar to the one shown in Fig. 2.8(A). The fabricated vortex phase mask DOE was used instead of the SLM. (a) and (b) shows the image of fiduciary beads with a standard clear aperture and a vortex phase mask respectively at a defocus of 1.2 microns. (c) Shows the image of DCDHF-N-6 molecules embedded in PMMA creating fixed dipole emitters..... 53

Fig. 2.18 Comparison of *CRLB* for 3D localization for a fixed dipole and an isotropic emitter: The 3D volume localization lower bound- $\sigma_{3D}(4\pi/3 \cdot \sigma_x \cdot \sigma_y \cdot \sigma_z)$ is plotted as a function of the polar angle Θ and defocus distance (z_0). The systems compared in the above plots are the linear polarization with the DH mask (PS-DH: blue surface), and the DH system for the isotropic emitter (Iso-DH: green surface). For this comparison it is assumed that both emitters emit the same number of photons leading to varying number of detected photons. 56

Fig. 3.1 Multiple steps in typical binary multi-exposure lithography. The number of discrete levels is 2^M , where M is the number of binary amplitude masks used. 60

Fig. 3.2 Diffraction efficiency (η) as a function of number of discrete phase levels used to approximate a continuous profile..... 60

Fig. 3.3 Design of the binary amplitude mask. (a) Design showing the amplitude mask to create an aperture in chromium mask and the four binary amplitude masks required to generate the 16-level phase mask. (b) Coarse alignment markers used to align the phase mask in the center of the aperture. (b) Fine alignment markers used to align the binary amplitude masks on each other. 62

Fig. 3.4 Step-by-step procedure for exposing a single binary amplitude mask: The steps involved in each of the exposure steps is shown. The substrate used here is quartz; photo-resist is the positive Clariant AZ4210. The photo-resist is spin-coated for 30s at 6000 rpm to create a

~1.8 micron thick layer. UV light is exposed onto the photoresist for 12s using a 160W light source. The exposed mask is developed in a 1:4 solution of AZ400K and DI water for 2 minutes. Reactive ion etching used to etch in glass whereas chemical etching using CR-7S is used to etch away chromium to create a circular aperture. The photo-resist is stripped using acetone in the final step..... 63

Fig. 3.5 Profilometry measurement of vortex phase mask: A white light interferometer is used to measure the depth profile of the fabricated vortex phase mask. The figure shows (a) 2d cross section of the fabricated mask. (b) The 1d depth variation is shown along the white line in (a). (c) Using the depth profile the relative phase difference is calculated. (d) 3d view of the fabricated phase mask. 67

Fig. 3.6 CRLB comparison of the ideal vs. fabricated vortex mask: Lower bounds of the (a) volume standard deviation and (b) solid angle standard deviation for the ideal vortex phase mask (green) and the fabricated vortex mask (red) is shown for the single channel total intensity system (solid) and the linear polarization system (dashed). 68

Fig. 4.1 Metamaterial structures for magnetic resonance: The structures compared are (a) Aperiodic unit cell (b) Periodic unit cell. The nanowires have a diameter of 10nm and are composed of silver. The islands in both cases are arranged periodically with a period of 70nm. 73

Fig. 4.2 (a) Simulation conditions for the FEM. Perfect Electric Conductor (PEC) and Periodic Boundary Conditions (PBC) are applied to the top and bottom surfaces of the unit cell. (Rf) and (Tr) are the planes in the far field (900nm for a $\lambda_{\text{resonance}}$ of 350nm) where the reflection and transmission coefficients are respectively evaluated. (1) and (2) are two different reference planes used to determine the reflection coefficient and hence the effective refractive index. (b) Real part of the effective refractive index over a broad frequency range for reference plane at

distance 35nm (black) and 30nm(blue) from the center of the unit cell for the aperiodic structure
(c) Effective impedance for the corresponding aperiodic structure where the number of periods in the propagation direction are 1 (blue), 3 (black) and 5(red) 74

Fig. 4.3 Comparison of the effective permeability of the aperiodic structure for a range of incident angles: (a) Effective permeability as a function of frequency for incidence angles ranging from 10° to 40° in 10° intervals. The resonance feature is retained. (b) Effective permeability at 8.47×10^{14} Hz for incidence angles ranging from 0° to 75° in 5° intervals. The chosen frequency is the one at which the effective permeability is the strongest negative for normal incidence..... 76

Fig. 4.4 Validation of effective medium approach and comparison of effective permeabilities: (a) Photonic band structure of the aperiodic configuration using effective parameters (blue line) and using rigorous photonic band structure calculation (blue dots). (b) Comparison of effective permeability for the aperiodic structure (blue) and for a periodic structure with wire spacing 11nm (black) and 11.4 nm (green). The inset shows the effective permeability for a single unit cell of the aperiodic structure. Solid(-) and dashed(--) lines represent the real and imaginary parts of the effective permeability respectively. 77

Fig. 4.5 Sensitivity analysis: The plots show the effective permeability at the resonance frequency after perturbation of (a) the structure with the aperiodic unit cell, and (b) the structure with the periodic unit cell (wire spacing is 11nm)..... 79

Fig. 4.6 Magnetic field distributions and electric field vector plots for the aperiodic and periodic structures at their respective resonance frequencies ($f_{\text{resonance}}$). The color map represents the relative strength of the magnetic fields. (a), (b) and (c) represent the original, best case (perturbed structure that yields lowest μ'), and worst case (perturbed structure that yields

highest μ') designs for the periodic structure whereas (d), (e) and (f) represent the corresponding designs for the aperiodic structure. 81

Fig. 5.1 Zemax simulation of a perfect paraxial lens: The lens focal length was chosen to be 50mm. (a) The object and image are $2f$ away from the lens. (b) The diffraction encircled energy shows that all the power is within the diffraction limited spot size. (c) Airy disc is shown in black and the system is not limited by aberrations (d) Cross-section of the diffraction limited PSF..... 86

Fig. 5.2 Isotropic thin lens in the paraxial regime: The maximum angle of incidence is given by $\tan^{-1}(4/10) \approx 22^\circ$. (b) Most of the energy is contained in the diffraction limited spot which is also seen in (c). The rms spot size is $1.8 \mu\text{m}$ and the airy disc radius is $2.4 \mu\text{m}$ 88

Fig. 5.3 Isotropic lens for large incidence angles (63°). (a) and (b) show the results with only the image distance optimized whereas in (c) and (d) both the surface curvature and the image distance was optimized. The rms spot size (and airy disc size) for the two cases are $3727 \mu\text{m}$ ($0.6 \mu\text{m}$) and $1031 \mu\text{m}$ ($0.73 \mu\text{m}$)..... 89

Fig. 5.4 Phase Linear-Refractive Material (PLRM) – (a) Schematic of the linear relationship between the angles of incidence and refraction. (b) Variation of the refractive index for a PLRM with respect to the incident angle (θ_i) for two different linearity constants. (c) Refractive index variation as a function of phase-refraction angle (θ_r). (d) The effective index surfaces for these materials. PLRMs guarantee that the direction of the refracted k -vector is in a linear angular relationship with the incident k -vector..... 91

Fig. 5.5: Linear Poynting material (LPM). (a) Schematic of the relationship between angle of incidence and angle of Poynting vector (b) Schematic of a hypothetical k -surface relationship between air (green curve) and an LPM (red curve). The dotted lines represent

conservation of transverse momentum (k_x) (c) The index curves for LPM calculated at increasing approximation and showing convergence to the solution..... 93

Fig. 5.6 Index ellipse of the eo-ray refracted at an angle θ_e . The c -axis is along the surface normal. 96

Fig. 5.7 PLRM vs. negative uniaxial material: (a) Comparison of the effective index curve for PLRM (solid blue and red) with effective index of the eo-wave (dashed blue and red) and o-wave (dashed black) of a uniaxial material. The linearity constants considered for PLRM are $K=1.2$ (blue) and $K=1.5$ (red). The o- and eo- refractive index are chosen to roughly match the index of PLRM. The phase-refraction (solid) and Poynting vector angles (dashed) for PLRM (blue) and the o- (black) and eo-wave (red) for the uniaxial material are shown in (b) $K=1.2$ and (c) $K=1.5$ 98

Fig. 5.8 Uniaxial thin lens in the paraxial regime: The maximum angle of incidence is given by $\tan^{-1}(4/10) \approx 22^\circ$. (b) Most of the energy is contained in the diffraction limited spot which is also seen in (c). The rms spot size is $0.57 \mu\text{m}$ and the airy disc radius is $1.579 \mu\text{m}$ 101

Fig. 5.9 Uniaxial thin lens for large incidence angles (63°): (a) and (b) show the results with only the image distance optimized whereas in (c) and (d) both the surface curvature and the image distance were optimized. The rms spot size (and airy disc size) for the two cases are $1641 \mu\text{m}$ ($0.49 \mu\text{m}$) and $495 \mu\text{m}$ ($0.52 \mu\text{m}$). 102

Fig. 5.10 Artificial dielectric lenses improve spot size for highly nonparaxial rays. The left plot shows the extraordinary rays rms spot size as a function of the difference between ordinary and extraordinary indices Δn . The right plots show the spot size for the ordinary rays. Interestingly, both rays improve spot size for large fields of view..... 104

Fig. 5.11 RMS spot size as a function of relative birefringence: Left plots are for extraordinary rays while right plots are for ordinary rays. 105

Fig. 5.12 Seidel aberrations as a function of relative birefringence 105

Fig. 5.13 Comparison of Mars rover navigation lens with alternative IRAM lens: The three columns show the full view, zoomed view of the lens system and the spot diagram for the navigation lens on the Mars Rover. Row A shows the original configuration consisting of four lenses. Row B shows the configuration that uses two IRAM lenses instead. A reduction in spot size is observed using the alternative IRAM configuration..... 107

Fig. 5.14 Refraction at the interface of a negative uniaxial material: (a) Schematic of the incident and refraction angles at the interface between air and a negative uniaxial material. (b) k -space diagram at the interface. This is also used as a graphical solution to find the phase-refraction angles and the direction of energy propagation..... 111

Fig. 5.15 Schematic of convex and concave spherical surfaces: The source is considered to be on-axis at a distance f from the surface. The angle of incidence at the surface is $\theta_i + \theta_R$ for the convex surface and $|\theta_i - \theta_R|$ for the concave surface. The normal from the point of incidence to the optical axis has a height of h and the distance between the surface and the normal is h_R . 114

Fig. 5.16 Maximum allowable incidence angle θ_i that is refracted as a function of parameter α for the convex (blue) and the concave (green) case 116

Fig. 5.17 Linear refraction performance at a spherical interface with a birefringent material. The c -axis is along the propagation direction both convex (black) and concave (blue) curved surfaces are considered. Three different ratios of source distance to the radius of the lens $\alpha = 0.1, 0.5$ and 5 (left to right) are shown. The uniaxial materials considered are $n_o=1.2, n_e=1.08$ (top row) and $n_o=1.5, n_e=1.2$ (bottom row). The dots (.) represent ideal PLRM, the solid (-) lines

represent the eo-wave phase vector direction for the uniaxial material and the dashed (--) lines represent the o-wave phase vector direction. 118

Fig. 5.18 PLRM vs. calcite (Flat interface): (a) Comparison of the effective index curve for an ideal PLRM (solid blue) with effective index of the eo-wave (green) and o-wave (black) of calcite. The ordinary and extra-ordinary refractive indices of calcite are $n_o=1.658$ and $n_e=1.486$. The linearity constant considered for PLRM is $K=1.658$ (blue) (b) The phase refraction angles (solid) and Poynting vector angles (dashed) for an ideal PLRM (blue), o-ray (black) and eo-ray (red) for calcite. 120

Fig. 5.19 Linear refraction performance at a spherical interface with calcite. The c -axis is along the propagation direction for both convex (black) and concave (blue) curved surfaces. Three different ratios of source distance to the curvature of the surface, $\alpha = 0.1, 0.5$ and 5 (left to right) are shown. The dots (.) represent ideal PLRM, the solid (-) lines represent the eo-wave phase vector direction for calcite and the dashed (--) lines represent the o-wave phase vector direction. 121

Fig. 5.20 Linear refraction performance at a planar interface with a uniaxial bi-anisotropic material: Phase-refraction angle as a function of angle of incidence with increasing chirality for (a) $n_o=1.2, n_e=1.15$ and (b) $n_o=1.5, n_e=1.25$ 126

Chapter 1 Introduction

Optical Imaging in the classical sense can be thought of as establishing an isomorphism between a source and its output. The three basic components of any conventional imaging system are an optical electromagnetic source, an optical system that maps that source to an output and a sensor array. However, the technological progress and inventions of the past few decades have revolutionized the imaging world in a way that a more modern definition is necessary in order to encompass the emergent field of computational optical imaging. Computational optical imaging, can be generalized as the modulation, transfer, collection, and processing of an optical signal, originating from an object due to emission, absorption, reflection, or scattering, in order to extract valuable and specific information about the (possibly inaccessible) object.

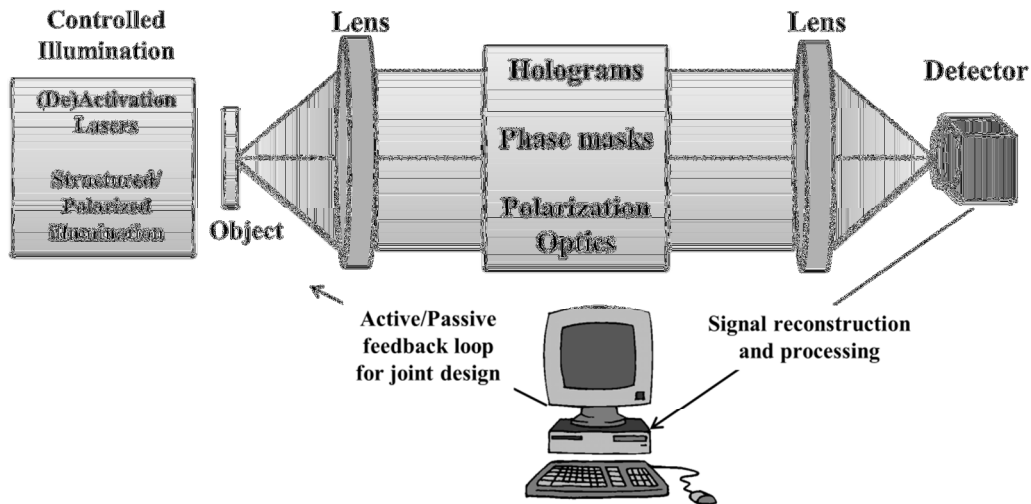


Fig. 1.1 Schematic of a modern computational optical imaging system: It generally consists of controlled illumination; spherical/aspherical lenses; SLM, phase masks, holograms, etc. for signal modulation; detector and a signal processing and reconstruction unit. The goal of a modern system is to jointly optimize all these components to increase its information throughput. The optimization can be either active or passive depending on the application.

Modern computational optical imaging systems typically are composed of five components: controlled illumination; passive devices like spherical/aspherical lenses; Spatial

light modulator (SLM), phase masks, holograms, etc. for signal modulation; detectors; and a signal reconstruction and processing unit (see Fig. 1.1). The rationale behind this approach stems from the fact that a joint design of these elements can provide gains in information[1]–[8].

For decades, geometrical optics and scalar wave optics have been the prime theories used to design and explain most of the imaging phenomena. However, as we push the limit of optics towards subwavelength designs, single molecule imaging, novel optical metamaterials, etc., the complexity of optical components has increased, requiring a more rigorous and fundamental approach, namely electromagnetic optics. In electromagnetic optics, the vectorial nature of light is not neglected as opposed to the scalar approximation in wave optics. For example, high numerical aperture objectives with $NA \sim 1.4$ are commonplace in single molecule fluorescence experiments and it can be shown that unlike the predictions of the scalar theory the point spread function (PSF) of high NA systems is non-symmetrical in the transverse plane[9]. Also, in single molecule experiments, when the fluorescence protein is rotationally immobile, the emission pattern is anisotropic and resembles that of a dipole. The impulse response due to anisotropic emission also requires a complete vectorial theory of optics. In the past decade, there has been tremendous interest in exploring a new regime of artificial materials, known as metamaterials that exhibit properties not readily available in nature and can be used as building blocks for exotic lenses. Owing to the fact that metamaterials derive their properties from structure rather than composition, most metamaterials are inhomogeneous, anisotropic and spatially dispersive. On the contrary, the scalar approximation of electromagnetic optics holds when the medium is isotropic and homogeneous and thus there is a need to study these materials from the perspective of the vector theory.

1.1 Historical perspective of imaging

The advent and progress of computational optical imaging has been long coming and can be attributed to the various revolutions in imaging[10].

The three main components of any traditional optical imaging system are an input, a mapping device and a detector (ex: the human eye). The input most likely is either a remote source or a source whose information cannot be collected directly. The earliest form of imaging device was the pin-hole camera, also known as Camera Obscura. The main issue with the pin-hole setup was the poor light-collection efficiency thus requiring extremely long exposures. Although, lenses were in existence over 2700 years ago, they were mainly used as a burning device by focusing the sun's light. The use of lenses for imaging wasn't realized until Brewster used it to take the first photograph in 1800. This led to the first revolution in imaging: the birth of simple optical instruments like the microscope and telescope. These devices were mainly used to enhance human vision. The fact that readily available glass is extremely transmissive in the visible spectrum made it so that a plethora of such optical imaging devices were conceived. However, storing and exchanging images was still a challenge.

The second revolution in imaging came with the invention of the photographic film. Up until the invention of the film, most image exchanges occurred through man-made traces. The first use of the photochemical process was made by Niepece and later improved by Daguerre. The exposure times required were long and only stationary subjects could be captured. In the latter years, huge improvements were made to the film and its development process. With the introduction of flash photography and faster optical elements, dynamic scenes could now be imaged. From there on photographic films served a three-fold purpose of sensing of an image, storing an image and as a modulation device for optical information processing. Although, the

film did a pretty good job in all three areas, with the advent of electronic sensors, a more homogeneous optical processing device was in order. There are mainly two types of light modulators in use today: one's that use liquid crystals and other that use deformable mirrors. These electronic modulators have almost completely replaced the photographic film for optical information processing purposes.

The third revolution came about with the invention of the active sensor pixel. This can be attributed to the advent of the CCD/CMOS sensors[11]. These sensors generally consist of two dimensional arrays of active pixels that act as photo-detectors. In both types of sensors, an electronic charge is generated when the light hits an active pixel creating a voltage at that pixel. The electronic circuitry in the detector then converts this voltage into digital values. The electronic sensor has helped in the seamless integration of a complete optical imaging system, where image detection can be done on much faster time scales than previously possible.

We are now entering a new revolution of imaging termed as computational optical imaging. The miniaturization of computers combined with the ever increasing processing power and data storage capacity has been a key factor in the development of computational optical imaging systems. The earliest use of computers was in digitizing analog data to produce digital images that could be easily stored, reproduced and transmitted; thus giving birth to new disciplines such as machine vision and digital image processing. It was soon realized that apart from just analyzing captured images, computers can be utilized as a pre-processing tool as well. Thus, the goal of a computational optical imaging system is to jointly optimize the analog preprocessing, analog-to-digital conversion and the digital post-processing for gains in information. This gain can be in the form of imaging metrics (spatial resolution, depth of field, field of view, etc.); multidimensional imaging (2D to 3D images, spectral/polarization map etc.);

feature detection (object shape, size, color, etc.); compressive sensing, etc. In this thesis I will mainly be focusing on the imaging metrics aspect of computational optical imaging, specifically on spatial resolution. The following few sub-sections will elaborate on a few key terms that will be used throughout this work.

1.1.1 Diffraction limit

The resolution of all optical imaging systems is limited by what is known as the diffraction limit. This limit can be attributed to the fact that information about subwavelength features is encoded in the form evanescent waves. These waves decay exponentially and all the information about structures smaller than the wavelength of light is lost in the far-field. Due to the pioneering work of Abbe[12] and Rayleigh[13], the resolution limit due to diffraction was established to the order of $\sim\lambda/2$, λ being the wavelength of light. Thus for visible light, the smallest resolvable features are on the order of $\sim 200\text{-}400\text{nm}$.

1.1.2 Optical Aberrations

The diffraction limit is a fundamental limit and assumes a perfect optical imaging system. However, achieving this fundamental limit is also challenging due to imperfections introduced by optical lenses. These imperfections manifest themselves as optical aberrations and can be broadly divided into chromatic and Seidel aberrations. Chromatic aberrations are the result of the wavelength dependence of refractive index leading to a wavelength dependent shift in the focal point. On the other hand, Seidel or wavefront aberrations are a result of the paraxial approximation used in the design of lenses. In the paraxial limit, the sine of the angle of ray of light at an interface is approximated to the angle itself. Thus the higher order terms of the sine function are neglected. For rays, that subtend large angles at optical lenses, this approximation fails leading to third and higher order aberrations. Aberrations have the effect of further degrading the spatial resolution of optical systems.

1.1.3 Optical super-resolution

“Super-resolution”, as the name suggests implies resolution beyond the diffraction limit. In the last couple of decades there have been significant breakthroughs in overcoming the diffraction limit. By altering the source or the optical systems itself, it is now possible to resolve subwavelength features in certain systems. The phenomena of super-resolution can be mainly divided in two categories as: far-field and near field super-resolution.

Far-field super-resolution

The recent emergence of “super-resolution” far-field optical microscopy techniques has provided a means for attaining resolution beyond the diffraction limit (~250 nm) in noninvasive fluorescence imaging of biological structures[14], [15]. A subset of these techniques (STORM[16], PALM[17], f-PALM[18], PAINT[19], and BLINK[20]) relies on precise localization of sparse subsets of single-molecule emitters to surpass the diffraction limit by up to an order of magnitude (precisions of tens of nm).

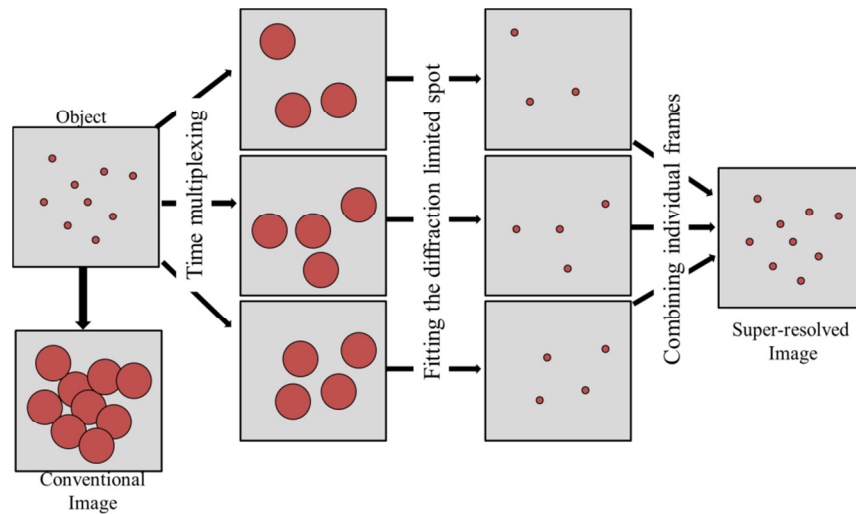


Fig. 1.2 Far-field super-resolution: Conventional image vs. super-resolved image. The figure shows the working of far-field super-resolution system where sparse subsets are imaged separately and later combined to form an image that is not limited by diffraction. Also shown on the bottom left is the image using a conventional microscope.

These methods typically employ image fitting that assumes an isotropic emission pattern from the single emitters as well as control of the emitter concentration. Fig. 1.2 illustrates the general working principle of the function super-resolution method. Computational techniques are used in post-processing time-multiplexed images, image-fitting, and for addressing correspondence issues between multiple frames.

Near-field Super-resolution:

This method refers to imaging beyond the diffraction limit by extracting information that would otherwise be lost in the evanescent waves. Since evanescent waves decay on the order of wavelength of light, these techniques generally work in the near field. Microscopy methods such as (apertureless) near-field scanning optical microscopy (A/NSOM), 4pi microscopy, superlens, etc., fall under the category of near-field super-resolution methods. Of these, superlens microscopy requires use of novel metamaterial lenses[21]–[26] whose properties are derived from its structure rather than just its composition. Thus the shape, size, arrangement and composition provide many degrees of freedom for optimizing the properties of metamaterials using computational techniques.

1.1.4 Point spread function (PSF) engineering

PSF engineering refers to the modulation of the impulse response of an optical system in order to recover some information that was previously inaccessible. As an example, PSF engineering can be used as a means to extract or extend the depth information of optical systems. As shown in Fig. 1.3, the PSF of a standard optical system consisting of a circular aperture is the well-known airy-disc. As the point object moves away from focus, the airy-disc gets blurred further making it challenging to estimate the position of the object for photon-limited systems.

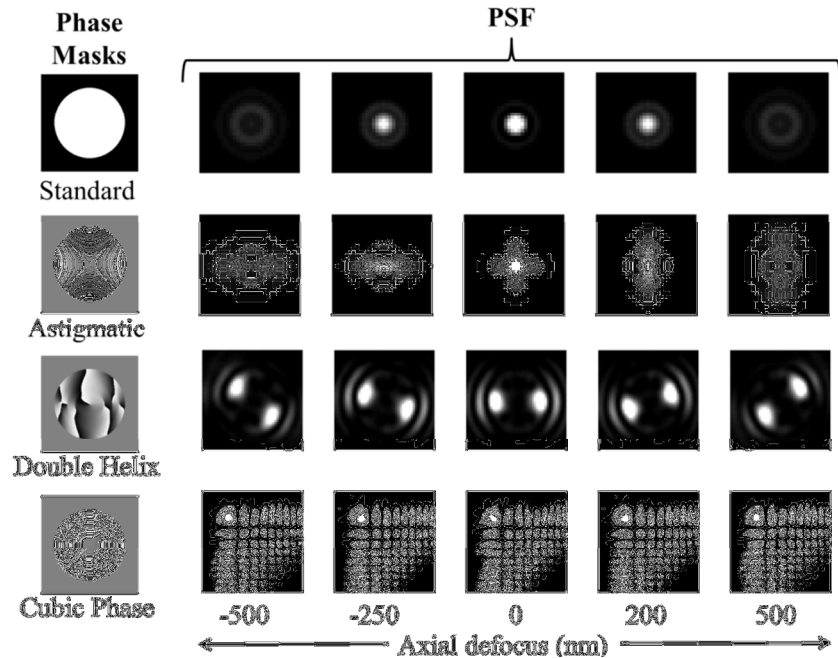


Fig. 1.3 PSF engineering: The figure shows the PSF for the standard and non-standard apertures as the point object is defocused within a 1 micron depth range. The standard aperture's PSF is the well-known airy-disc that blurs with defocus. Astigmatism introduces asymmetry in the transverse focus. Introduction of the double-helix phase mask causes the PSF to split into two symmetric lobes that rotate as a function of defocus. The cubic phase is used to extend the depth of field by creating a PSF that remains constant with defocus.

By inserting an appropriate amplitude/phase element in the pupil it is possible to modify the behavior of the PSF. Astigmatic PSF[27], [28], as the name suggests, introduces asymmetry in the response of the PSF making it possible to distinguish between positive and negative defocus. The double-helix phase mask[29]–[31] consists of phase discontinuities placed in a way that the energy is redistributed between two lobes that rotate as a function of axial defocus. The transverse position of the point object can be found by finding the center of the two-lobed pattern, whereas the angle between the two lobes determines the amount and direction of defocus. The cubic-phase mask[32] differs from the astigmatic and double-helix in the sense that it is primarily used to extend the depth of field. As shown in the figure, the PSF remains constant as a function of defocus and by deconvolving the constant PSF with the obtained image it is possible to obtain an image that remains relatively sharp for a large depth of field.

1.2 Electromagnetic Optics

In the classical sense, light is just a form of electromagnetic radiation and follows the same laws as all other electromagnetic waves and is governed by Maxwell's equations. Thus light consists of electric and magnetic vector fields that are coupled together and are in general perpendicular to the direction of propagation of light. The entire electromagnetic spectrum covering waves from low frequency radio waves to ultra-high frequency gamma rays is shown in Fig. 1.4(a). Optics, in general, deals with radiation that lies between the UV and Infrared. The spectrum between 400 to 800 nm is termed as visible light.

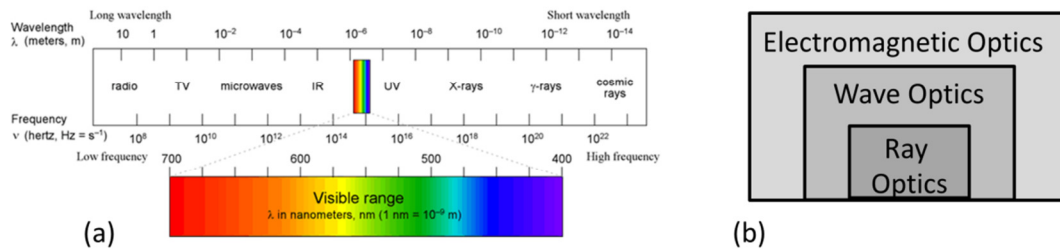


Fig. 1.4 (a) Shows the electromagnetic spectrum ranging from very low frequency ($\sim 10^3$ Hz) to gamma rays (10^{21} Hz). Optical frequency covers a small region of this spectrum with wavelengths ranging from the infrared (10^{12} Hz) to the ultra-violet (10^{16} Hz). Visible light covers wavelength ranges from ~ 200 nm to ~ 800 nm (b) Shows the various theories of optics in a Venn diagram. Ray Optics is an approximation of Wave Optics which is the scalar approximation of Electromagnetic Optics..

There are several different theories that can be used to describe the nature of light. Each theory has its advantages and disadvantages in terms of its simplicity and applicability. Although, it is not always obvious which theory should be used, apriori knowledge about the problem at hand can prove to be extremely viable. A Venn diagram of different approximate theories of optics is shown in Fig. 1.4(b). The most simplified theory of light is called ray optics also commonly known as geometrical optics. The underlying assumption of ray optics is that the phase and amplitude changes of the light wave occur on spatial scales much larger than its

wavelength, and a set of geometrical rules can adequately describe the nature of light. Thus in the ray-optics limit the wavelength of light is assumed to be zero. Using ray optics it can be shown that in a constant medium, light rays always travel in straight lines. Another major result of ray optics is the Snell's law that relates the incident angle of a ray to the reflected/refracted angle near dielectric boundaries. Ray optics can also be used to find the location of an image in an imaging system but the effects of diffraction cannot be explained using ray optics.

Wave optics or physical optics is a more comprehensive description of electromagnetic waves and it also encompasses ray optics. Optical phenomena like diffraction and interference can be easily explained using the wave nature of light. The finite wavelength of light is an important factor in determining the outcomes of the wave theory and structures that are on the order of wavelength of light can be studied using wave optics. Although wave optics can explain most physical phenomena, a major assumption is that the vectorial nature of light can be replaced by a simpler scalar assumption based on the fact that the coupling between the various vector fields is small.

Electromagnetic optics, on the other hand, is that branch of optics that takes into consideration the vectorial nature of light and is an all-encompassing theory in the classical limit. However, certain phenomena require a more rigorous theory comprising of the quantum nature of light. This can be termed as quantum optics but is out of the scope of this thesis. Electromagnetic optics is important to explain several optical phenomena such as a complete description of light at boundaries of dielectric media, propagation inside non-linear and/or dispersive media, magnetically active metamaterials, polarization effects, etc. Thus, electromagnetic optics encompasses wave optics which in turn encompasses ray optics. To illustrate the

difference between scalar and vector optics let's look at Maxwell's equations. In absence of free charge the four Maxwell's equations are given by

$$\nabla \times \vec{E} = -\mu \frac{\partial \vec{H}}{\partial t} \quad (1.1)$$

$$\nabla \times \vec{H} = \varepsilon \frac{\partial \vec{E}}{\partial t} \quad (1.2)$$

$$\nabla \cdot \varepsilon \vec{E} = 0 \quad (1.3)$$

$$\nabla \cdot \mu \vec{H} = 0 \quad (1.4)$$

Here, \vec{E} and \vec{H} are the vector electric and magnetic fields respectively with components in the x , y and z directions. The medium in which the wave propagates is characterized completely by its permittivity ε and permeability μ . Note that the fields are a function of space and time. For a linear, isotropic, non-dispersive and homogeneous medium, it can be shown that by taking the curl of eq. (1.1) (1.2) and substituting eq. (1.3) (1.4) we obtain the vector wave equations given by

$$\nabla^2 \vec{E} - \frac{n^2}{c^2} \frac{\partial^2 \vec{E}}{\partial t^2} = 0 \quad (1.5)$$

$$\nabla^2 \vec{H} - \frac{n^2}{c^2} \frac{\partial^2 \vec{H}}{\partial t^2} = 0 \quad (1.6)$$

Where, the refractive index of the medium is defined by $n = \sqrt{\varepsilon\mu/\varepsilon_0\mu_0}$ and c is the speed of light given by $c = 1/\sqrt{\varepsilon_0\mu_0}$. From the above equations it is clear that each component of the electric and magnetic field satisfies the wave equation individually with no coupling between the various fields and the scalar form can be written as

$$\nabla^2 u(\vec{r}, t) - \frac{n^2}{c^2} \frac{\partial^2 u(\vec{r}, t)}{\partial t^2} = 0 \quad (1.7)$$

Where, $u(\vec{r}, t)$ represents the scalar field components and is a function of position and time. Thus as long as the propagation medium is linear, isotropic, non-dispersive, and homogeneous, the scalar approximation of the wave equation is generally valid. However, when

one or more of the above four conditions is not satisfied, a coupling is introduced between the various scalar terms rendering the scalar optics approximation invalid. The scalar approximation also introduces errors when boundary conditions are introduced and thus care has to be taken while applying the scalar theory at the edges of apertures. Although, the scalar theory of light finds applications in a wide variety of scenarios and has been successfully applied to a wide variety of imaging problems, there is a need to study polarization based modern imaging systems using the electromagnetic optics approach. In the following section, I will elaborate on the situations where the vector approach is needed and this also forms the basis of the main motivation behind this thesis.

1.3 Motivation and main contributions

1.3.1 Anisotropic emission of molecular dipoles

As shown in section 1.1.3, far-field “super-resolution” methods have been able to overcome the diffraction limit by isolating single molecules and fitting them to find the true position of the molecules, thus improving the resolution by an order of magnitude. The major assumption for single-molecule fitting is that the emission pattern of single molecules is adequately described by the scalar Green’s function of a point source, i.e. a spherical wave. However, anisotropic single-molecule emission patterns arise from the transition dipole moment when the dipole is rotationally immobile, depending highly on the molecule’s three-dimensional (3D) orientation and z position. For point dipoles, it is important to consider the dyadic Green’s function that takes into account the polarization of the molecular dipoles. Failure to account for this fact can lead to significant lateral (x, y) mislocalizations (up to ~50-200 nm)[33], [34]. This systematic error can cause distortions in the reconstructed images, which can translate into degraded resolution.

The 3D orientation and location of individual molecules also serves as an important marker for the local environment and the state of a molecule. The photo-physical properties of individual fluorophores depend on both the orientation and location of the molecule with respect to its environment. Therefore, direct measurement of these properties is of interest[35], [36] for sampling the local environment, detecting chemical reactions, measuring molecular motions, sensing conformational changes and as a means to realize optical resolution beyond the diffraction limit[16]–[18], [27], [37]. Furthermore, using wide-field microscopy for single-molecule detection allows for parallelized information throughput from a three-dimensional volume, potentially containing many events of interest. Therefore dipole localization and orientation estimation is important for biological sensing and imaging. However, previously reported single-molecule orientation techniques normally operate within a reduced depth of defocus [38]–[40] and/or on one molecule at a time[40], [41] , significantly limiting their applicability. While some of these techniques could be extended to operate in a longer field of view, our study shows that they are not optimal or sensitive enough. These limitations restrict the number of available degrees of freedom to analyze a three dimensional (3D) volume including a multitude of molecules.

The joint imaging of the 3D location and 2D orientation[42]–[47] is termed as 5D imaging of single-molecules and is presented in Chapter 2. We propose and analyze wide field microscope configurations to simultaneously measure the position and orientation of multiple fixed dipole emitters. Examination of the images of radiating dipoles reveals how information transfer and precise detection can be improved. We use an information theoretic analysis to quantify the performance limits of position and orientation estimation through comparison of the Cramer-Rao lower bound (*CRLB*) in a photon limited environment. Further, experimental

verification is provided for simultaneously estimating the position and orientation of fixed dipoles using the double-helix phase mask. The fabrication of efficient phase masks as diffractive optical elements using the binary multi-level exposure method on glass substrates is demonstrated in Chapter 3.

1.3.2 Magnetic resonance required for NIM using metamaterials

Metamaterials are artificially structured materials whose properties can be engineered by altering the shape, size and composition of the structural units composing it. In the long wavelength limit; where the wavelength of light is much greater than the periodicity of these units; metamaterials can be assigned macroscopic optical constants. Such materials, if properly designed, can exhibit non-conventional properties, like negative refractive index[48], [49] and ultra-low refractive index[50], [51]. This could lead to applications such as imaging with subwavelength resolution using a flat lens[48], optical nanocircuits[52], and cloaking[53]–[57]. In this regard, materials that exhibit magnetic resonance have recently attracted interest for synthesizing exotic optical properties of metamaterials. However, none of the known naturally occurring materials are magnetic near optical frequencies. In Chapter 4, we present a metamaterial architecture that exhibits strong magnetic resonance at optical frequencies[58], [59]. The metamaterials structure proposed here consists of silver nano-wires whose properties depend on the polarization of the incoming light making wave optics an incomplete theory to characterize the properties of metamaterials.

1.3.3 Infinitely refraction-linear artificial materials (IRAM)

Classical optical imaging systems consist of a series of refracting (or reflecting) surfaces interfacing among homogeneous isotropic materials that generally have a common axis of rotational symmetry. The surfaces are used to bend light rays originating in an object according to the laws of geometrical optics to form an image. According to the Gaussian optics

approximation[60], the angle that a ray from a point object makes with the optical axis or a surface normal is considered small so that the law of refraction takes a simple form. The rays traced in this approximation are called paraxial rays and all the rays diverging from a point object and propagating through the system converge to a point named the Gaussian image point. However, if the rays are traced according to the exact geometrical optics laws, they generally do not converge to an image point resulting in aberrations.

Traditional optical design aims at correcting such aberrations via multiple surface and/or multiple material systems that meet a set of performance requirements and constraints[60]. Modern lens design can also take advantage of aspheric[61], graded index[62], diffractive or holographic lenses[63] to reduce aberrations and overall complexity and size. Techniques that incorporate these uncommon lenses have become increasingly attractive for high-end applications such as medical endoscopes or lightwave communications, while pervasive in consumer electronics such as cell-phone cameras. However, even with all these techniques at hand, optical designs are still based on ray tracing optimizations over tens or hundreds of dimensions that typically result in tradeoffs in terms of performance, size, weight, and form factor.

In Chapter 5, we propose a new paradigm for optical design based on artificial materials determined by design. The proposed infinitely refraction-linear artificial materials (IRAM) enable three-dimensional or high NA optical elements to maintain a linear relationship between input and output angles of refraction over a large field of view. By using first-order approximation, it can be shown that IRAMs are inherently anisotropic and thus polarization characteristics of light, accounted for by electromagnetic optics, need to be considered.

A summary of the thesis and future work is presented in Chapter 6.

Chapter 2 5D imaging: 3D localization and orientation estimation of single-molecules

2.1 Introduction

Single molecules that freely move exploring all possible orientations can be modeled as point emitters as a result of the rapid and random orientation changes on a time scale much shorter than the integration time of the detection device. Standard optical microscopes have been used to localize isotropically emitting molecules and extended to all three dimensions with the use of point spread functions (PSF) engineered specifically for 3D localization of isotropic emitters. Techniques that use multiple defocused image planes [12, 13], astigmatic optics[27], and Double-Helix PSFs [4, 14, 15] have been particularly successful in demonstrating that the optical system response can be tailored to enhance 3D localization performance [68]. Efficient estimators have demonstrated experimentally the possibility of reaching the fundamental limit of 3D localization precision provided by the Cramer-Rao Lower Bound (*CRLB*) [17, 18]. The use of an accurate system model, proper estimators, and calibration are critical to achieve the localization precision limit and avoid bias [15, 17–19].

However, the application of these techniques to dipole emitters such as fixed single molecules, where the isotropic assumption is not valid, is not straightforward and if the proper model and estimator are not used they can lead to orientation-dependent systematic errors[33], [34], [72], [73]. Enderlein *et al.*[33] have shown that fitting such a single-molecule image to a 2D Gaussian can result in position errors of tens of nm for molecules located in the microscope's focal plane. Even more strikingly, Engelhardt *et al.*[34] noted that with modest defocusing ($z = \pm 300$ nm), the position error associated with fitting to a centroid can exceed 100 nm for certain

single-molecule dipole orientations. If labels are sufficiently rotationally mobile such that they explore much of the orientation space within a single acquisition, this effect is averaged away and accuracy can be recovered. However, in some cases labels of biological structures can exhibit well-defined orientations[74]. Furthermore, fluorophores can be purposely anchored to convey orientation information about biological macromolecules, such as in various SM studies on motor protein translocation[75]–[77].

There are many established methods for determining dipole orientation of single fluorophores. Approaches have been developed which rely on excitation and/or emission with multiple polarizations[20], [78], introducing defocus and pattern matching[71], direct imaging of pupil functions[40], and using annular illumination to create characteristic field distributions[79], to name a few. The alternating measurement of 2D position and orientation has also been addressed[80]. Two groups considered simultaneous 2D localization and orientation fitting for molecules located in the focal plane[39] or for molecules at a known defocus[69]. However, most of these methods rely on imaging the total intensity of the dipole emission pattern, thus ignoring any polarization sensitive information that is inherently encoded in the Green's tensor response of a rotationally immobile molecular dipole.

This chapter addresses the design of optical microscope systems for the specific task of estimating the location and/or 3D orientation of multiple fixed dipoles in a wide field system. The goal is to create a system (or systems) that can precisely distinguish among different dipole positions and orientations in 3D space. The response of a system to a dipole input for different positions and orientations is the dipole spread function or more precisely the Green's tensor. Thus Green's tensor engineering for the estimation of dipole localization and orientation is the generalization of PSF engineering for the case of isotropic emitters (see Fig. 2.1(a)). The key

difference is the a priori assumption about the nature of the emitting particles and its implications for the optical system design. PSF engineering assumes the imaging of point emitters and has demonstrated the possibility of generating information efficient responses that encode the desired parameters. Similarly, Green's tensor engineering addresses the possibility of shaping the optical response to fixed dipoles at varying orientations. With the additional degrees of freedom in dipole orientation, the prior PSF designs may no longer provide optimum information efficient solutions, hence opening opportunities for novel task-specific designs. We present solutions based on polarization encoded imaging that overcome the limitations of polarization insensitive systems currently in use [8–10, 19, 20, 24]. In section 2.2, we describe the analytic expressions used to model microscope systems that image the field distributions of fixed dipoles. We present the field distributions for representative dipole orientations and for specific microscope systems. In section 2.3, we use the *CRLB* to compare these systems based on their ultimate capacity to estimate the location and 3D orientation of fixed dipoles. It is established that the precision lower bounds using a double-helix microscope are much lower than the standard systems and experimental validation is provided in section 2.4. In section 2.5, we analyze the *CRLB* of the spiral (vortex) phase mask that contains a single phase discontinuity.

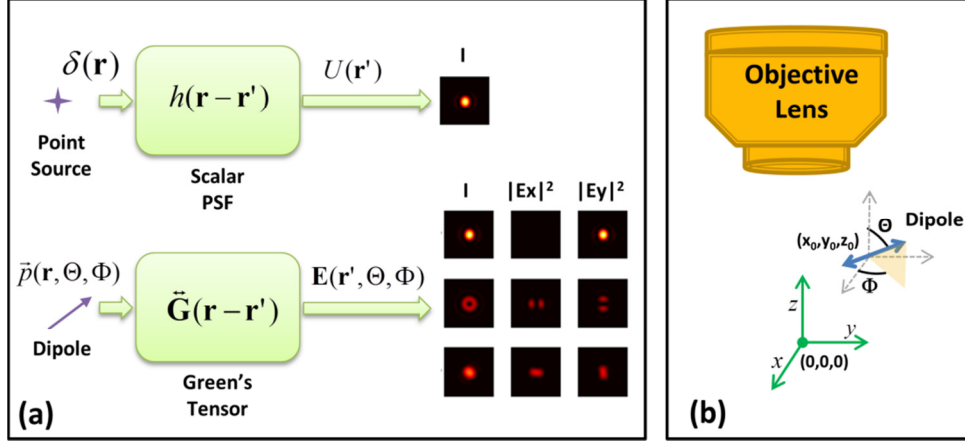


Fig. 2.1 Point Spread Function Engineering versus Green's tensor engineering: (a) The PSF is the response of the system to a point source whereas the Green's tensor is the response of the system to a dipole input. The output of the Green's tensor system is a vector function of the dipole orientation. Each of the rows, shown at the output, corresponds to a unique dipole orientation, showing the total intensity and the intensity of two transverse orthogonal components of the electric field. (b) The position and orientation of a dipole with respect to an objective lens defines the input space. The origin (0,0,0) is at the focal point of the objective lens with the z-axis parallel to the optical axis. Here (x_0, y_0, z_0) represent the position of the dipole and (Θ, Φ) represent the polar and azimuthal orientation angles respectively.

2.2 Optical system model and analysis

The electric field distribution resulting from dipole radiation has known analytic solutions[9]. Given the position (x_0, y_0, z_0) and orientation (Θ, Φ) (see Fig. 2.1 (b)) of a dipole immersed in a medium of refractive index n_1 , the far-field radiation pattern in the spherical coordinate system is given by,

$$E_\theta^o = \Pi(\theta)[\cos \Theta \sin \theta + \sin \Theta \cos \theta \cos(\varphi - \Phi)] \quad (2.1)$$

$$E_\varphi^o = -\Pi(\theta) \sin \Theta \sin(\varphi - \Phi) \quad (2.2)$$

where E_θ^o and E_φ^o denote the polar and azimuthal fields, respectively, and angles θ and φ denote the polar and azimuthal angle spherical coordinates. The superscript o represents the fields on the object side. Similarly, fields at the back aperture are represented by the subscript b. $\Pi(\theta)$ is the phase factor introduced due to the position of the dipole and is given by,

$$\Pi(\theta) = \exp[ikn_1(x_0 \sin \theta \cos \varphi + y_0 \sin \theta \sin \varphi - z_0 \cos \theta)] \quad (2.3)$$

The lens acts as a coordinate transformation element that maps the fields from spherical coordinates (object space) to cylindrical coordinates (pupil plane). Accordingly, the fields at the pupil plane of the microscope objective are[9]

$$\begin{bmatrix} E_\varphi^b \\ E_\rho^b \end{bmatrix} = \begin{bmatrix} E_\varphi^o \\ E_\theta^o \end{bmatrix} \frac{\sqrt{n_2}}{\sqrt{n_1} \cos \theta} \quad (2.4)$$

where n_2 is the refractive index after the microscope objective and the ratio $\sqrt{n_2}/\sqrt{n_1} \cos \theta$ is required for energy conservation. The E_ρ^b and E_φ^b fields obtained are in cylindrical coordinates but for convenience we decompose the fields in orthogonal linear polarizations.

$$\begin{bmatrix} E_y^b \\ E_x^b \end{bmatrix} = \begin{bmatrix} \sin \varphi & \cos \varphi \\ \cos \varphi & -\sin \varphi \end{bmatrix} \begin{bmatrix} E_\rho^b \\ E_\varphi^b \end{bmatrix} \quad (2.5)$$

The Green's tensor can now be modified by placing a polarization element described by Jones matrix \mathbf{J}_{OE} as follows

$$\begin{bmatrix} E_x^{b'} \\ E_y^{b'} \end{bmatrix} = \mathbf{J}_{OE} \begin{bmatrix} E_x^b \\ E_y^b \end{bmatrix} \quad (2.6)$$

Furthermore, a phase/amplitude mask of transmittance function $P_{Mask}(x,y)$ in the Fourier plane can also modify the transfer function as follows: $E_x^{b'} = E_x^b \cdot P_{Mask}(x,y)$ and $E_y^{b'} = E_y^b \cdot P_{Mask}(x,y)$. In either case, the field at the pupil plane is then focused on the detector using a tube lens which performs to a good accuracy a scaled Fourier transform (FT) of the field at the pupil plane, i.e. $E_x = FT\{E_x^{b'}\}|_{\lambda_f}$ and $E_y = FT\{E_y^{b'}\}|_{\lambda_f}$. The total intensity at the detector is given by

$$I(r, \varphi, \Theta, \Phi) \propto (E_x E_x^* + E_y E_y^*) \quad (2.7)$$

From the above equations, it is clear that the emission pattern of the dipole, the intensity I , and intensity of the two linear polarizations $|E_x|^2$ and $|E_y|^2$ depend on the dipole orientation. Fig. 2.2 shows the associated intensity distributions for a dipole located at the focal plane (Fig. 2.2(a)) and at $0.2\mu\text{m}$ from the focal plane (Fig. 2.2(b)). Each row provides the resulting intensity distributions for each unique dipole orientation, namely, O1: dipole along \hat{y} ($\Theta=90^\circ$ $\Phi=90^\circ$); O2: dipole along \hat{z} ($\Theta=0^\circ$ $\Phi=0^\circ$); O3: dipole along $\Theta=45^\circ$ $\Phi=45^\circ$). Fig. 2.2 also shows different intensity distributions demonstrating the variability when using either total intensity or two different polarization state decompositions. Here, all systems in consideration have been standardized to use an objective lens with numerical aperture (NA) of 1.4 and assume the emission wavelength of the emitter at $\lambda=532$ nm. The dipole is assumed to be immersed in a medium of refractive index $n_1=1.52$.

For a dipole oriented along \hat{y} the intensity $|E_x|^2$ is zero and all the energy lies in $|E_y|^2$. This owes to the fact that the electric field of a dipole is linearly polarized along the dipole axis; which is true even when the dipole is defocused, implying that there is no information about the z -position of the dipole in $|E_x|^2$ for a dipole along \hat{y} . In order to make sure that irrespective of the orientation of the dipole, neither of the two orthogonal polarizations states have zero intensity; we propose a set of elliptical polarization images. The elliptical polarizations are obtained by superposing the orthogonal linear polarizations and can be realized by using a quarter wave plate with principal axis at 45° with the x -axis followed by polarizers along the x and y axes,

$$\begin{bmatrix} E_1^b \\ E_2^b \end{bmatrix} = \frac{1}{\sqrt{2}} \begin{bmatrix} 1 & i \\ 1 & -i \end{bmatrix} \begin{bmatrix} E_x^b \\ E_y^b \end{bmatrix} \quad (2.8)$$

From the above equations it can be seen that E_1^b and E_2^b form an orthogonal basis set.

The intensity distributions of these two elliptical polarizations are shown as the fourth and fifth

columns in Fig. 2.2(a) and Fig. 2.2(b). It can be seen that for the dipole orientations considered here, the elliptical polarization method results in a more uniform energy distribution between the two images.

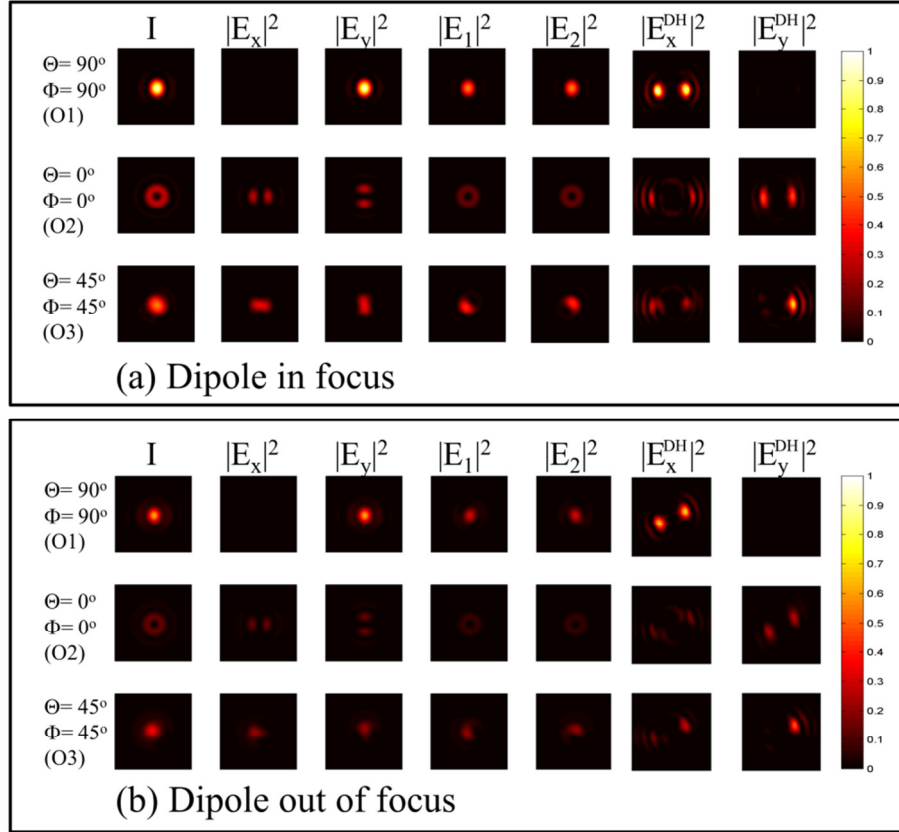


Fig. 2.2 Simulation of the dipole spread function along three representative orientations: I is the detected total Intensity (single channel system), $|E_x|^2$, $|E_y|^2$, $|E_1|^2$, and $|E_2|^2$ (left to right) correspond to images obtained in two-channel systems when using either orthogonal polarizers ($|E_x|^2$, $|E_y|^2$) or a quarter waveplate with orthogonal polarizer (see text for details), whereas $|E_x^{DH}|^2$ and $|E_y^{DH}|^2$ represent the intensity distributions of the two orthogonal linear polarizations using the double-helix phase mask (DH). In (a), the dipole is at the focal plane, while in (b) it is located $0.2 \mu\text{m}$ from the focal plane. The dipole is oriented along (from top to bottom) \hat{y} ($\Theta=90^\circ, \Phi=90^\circ$), \hat{z} ($\Theta=0^\circ, \Phi=0^\circ$) and $\Theta=45^\circ, \Phi=45^\circ$

The Green's tensor response can also be tailored by using phase masks. For instance, the last two columns of Fig. 2.2 show a polarization sensitive (PS) system that uses a double helix (DH) phase mask[66] in the Fourier plane. The DH phase mask has been extensively used for 3D

localization of isotropic emitters over an extended depth range. Here we analyze its use for Green's function engineering applied to fixed dipoles. Owing to the design of the DH mask, it generates two lobes that rotate as the dipoles are defocused, but for fixed dipoles the relative strength and lobe shape are significantly affected by the dipole orientation.

The simulated images in Fig. 2.2 reveal that dipole localization/orientation information is carried in the images at the orientations investigated and that the total intensity microscope, the linear polarization microscope (with or without the phase mask), and the elliptical polarization microscope are worth investigating as potential candidate solutions.

In what follows we compare different optical systems which are designed to employ either total intensity images, linear polarization images, or elliptical polarization images (Fig. 2.3) as a means to retrieve information from the system towards localization/orientation estimation. In addition to investigating the utility of polarization modulation, we propose including the bi-focal microscope configuration, i.e. simultaneously capturing the images at two different focal planes. This configuration has already been demonstrated to be useful for axial localization of isotropic emitters [12, 13]. It is noteworthy that a myriad of different systems could be realized. The systems considered here represent an interesting subset and act as a proof of principle of the possibilities available for Green's tensor engineering. Also, because of the inherent low signal collection in single-molecule imaging, each system is selected so that no photons exiting the objective pupil are lost beyond the neglected minor losses at the passive devices (polarizers, waveplates, lenses, and beam splitters).

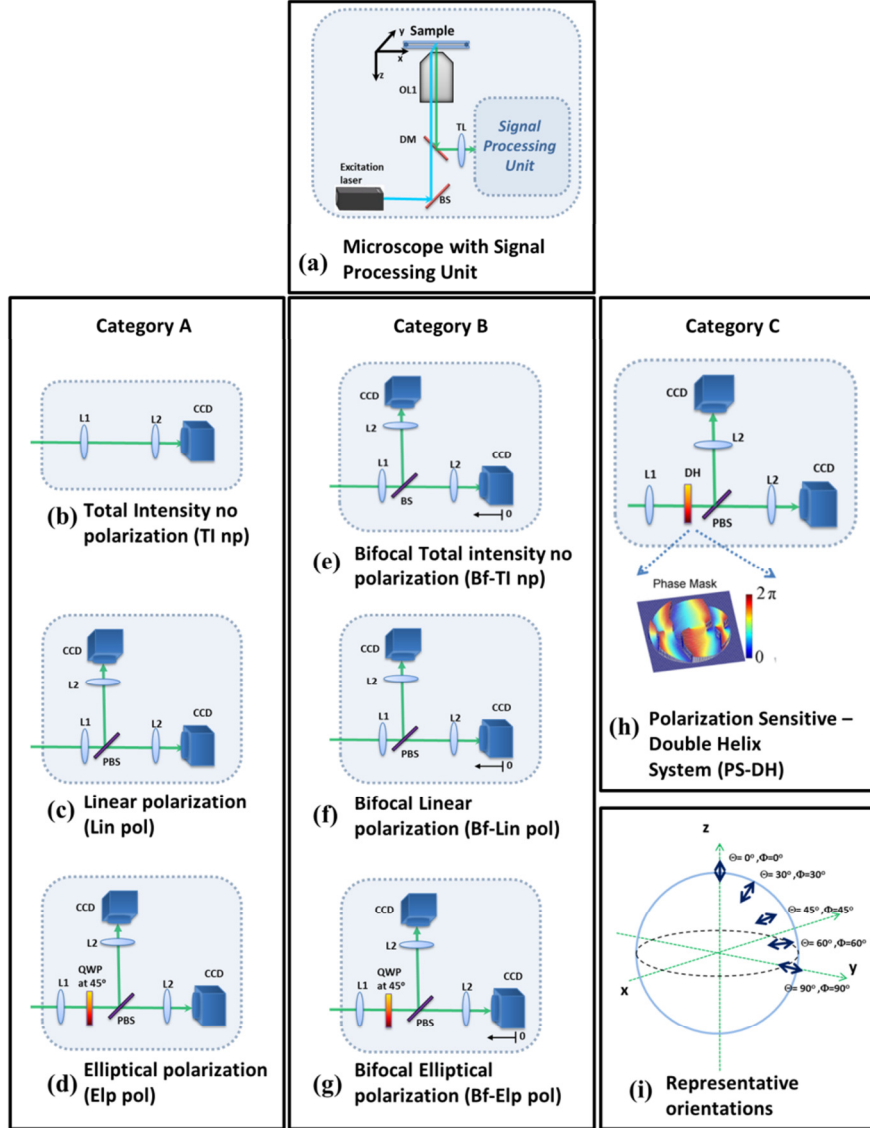


Fig. 2.3 Schematic of the systems considered for dipole location and orientation estimation: (a) A traditional microscope system with a signal processing unit for Green's function engineering. Category A shows three signal processing units that focus at the same plane whereas Category B shows the three signal processing units that focus at two different planes leading to a bifocal system. Parts (b) and (e), represent systems that measures the total intensity, parts (c) and (f) represent systems with two orthogonal polarization channels, imaging the intensities $|E_x|^2$ and $|E_y|^2$ separately, and parts (d) and (g) represent the systems with two polarization channels imaging the intensities of the elliptical polarizations components, $(|E_x + iE_y|^2)/2$ and $(|iE_x + E_y|^2)/2$ separately. (h) Shows the linear polarization system with a double-helix phase mask in the Fourier plane. (i) Shows the five dipole orientations used to compare these six systems on a unit sphere. TL - tube lens, L1, L2 -relay lenses, OL1 - objective lens, DM – dichroic mirror, PBS – polarizing beam splitter, QWP – Quarter wave plates with fast axis along 45° from x-axis.

The schematic in Fig. 2.3(a) shows the excitation laser and the microscope objective and represents the signal processing unit as a black box. Seven optical signal processing systems are split into three categories for analysis purpose. Category A (Fig. 2.3(b), Fig. 2.3(c), and Fig. 2.3(d)) requires that the system collects information from a single focal plane. Category B ((Fig. 2.3(e), Fig. 2.3(f), and Fig. 2.3(g)) uses two images located at two different focal depths. Also, as shown, the systems in Fig. 2.3(b) and Fig. 2.3(e) image the total intensity without polarization sensitivity. The systems in Fig. 2.3(c) and Fig. 2.3(f) consider the use of two imaging channels with orthogonal linear polarization states where the dipole emission is collected by a microscope objective and split by a polarizing beam splitter in the pupil plane. The systems in Fig. 2.3(d) and Fig. 2.3(g) show the use of two imaging channels that employ orthogonal elliptical polarizations as described in eq. (2.8). The emission light goes through a quarter wave plate with fast-axis aligned at 45° and is then split using a polarizing beam splitter; each channel is imaged separately using a pair of tube lenses. Category C considers the use of linear polarization system with the addition of phase masks. In particular, Fig. 2.3(h) shows the PS-DH system[37], [66] with a DH phase mask place in the Fourier plane.

The intensity distributions in Fig. 2.2 show that for dipoles oriented along O1:($\Theta=90^\circ$, $\Phi=90^\circ$) and O2:($\Theta=0^\circ$, $\Phi=0^\circ$) some of the systems in Fig. 2.3 might be lacking in information about the dipole's position and/or orientation whereas there is always finite information for dipoles oriented along O3:($\Theta=45^\circ$, $\Phi=45^\circ$). We further consider the results for two intermediate orientations at O4:($\Theta=30^\circ$, $\Phi=30^\circ$) and O5:($\Theta=60^\circ$, $\Phi=60^\circ$). Fig. 2.3(i) shows these five dipole orientations. These orientations were chosen as a representative set of the full 4π steradian solid angle.

2.3 Cramer-Rao Lower Bound

2.3.1 CRLB theory

Cramer-Rao lower bound (*CRLB*) is an information theoretical measurement that will be used to compare various optical systems. By definition, *CRLB* is a lower bound on the variance of all unbiased estimators. Thus *CRLB* is independent of the estimator and can be used as a measure of performance of an optical system.

Let's consider the single parameter estimation case first. Given a random sample X_1, X_2, \dots, X_n from a distribution with pdf $p_{i,j}(x|\psi)$. If we estimate the parameter ψ with any unbiased estimator $\hat{\psi}$, the theorem states that,

$$\text{Var}(\hat{\psi}) \geq \frac{1}{E \left[\left(\frac{\partial}{\partial \psi} \ln p(\bar{X} | \psi) \right)^2 \right]} \quad (2.9)$$

The term on the left hand side of eq. (2.9) represents the variance of any unbiased estimator; whereas the term on the right is the *CRLB*. Here, E refers to the expectation and \ln the natural logarithm. Since, the random sample appears only in the denominator, it is said to contain all the information about the sample and is termed as the Fisher Information (*FI*). Thus *CRLB* is the inverse of the Fisher information (*FI*). For an optical system, we generally deal with multiple parameters. For example, a point optical source is completely characterized by its position (x_0, y_0, z_0) whereas; a point dipole is characterized by its position and orientation $(x_0, y_0, z_0, \Theta, \Phi)$. Moreover, for a typical optical system the final image is formed on an electronic detector and the space over which the fisher information is calculated can be described in terms of the detector pixels. Thus, in a multivariable case the *FI* can be written in a matrix form as [28]

$$FI_{\psi} [m, n] = \sum_{i,j} E \left[\frac{\partial \ln p_{i,j}(k | \psi)}{\partial \psi [m]} \frac{\partial \ln p_{i,j}(k | \psi)}{\partial \psi [n]} \right] \quad (2.10)$$

where ψ is the unknown parameter to be estimated. Thus, for an N -parameter estimation problem, the FI is a $N \times N$ matrix. Here $p_{i,j}(k|\psi)$ is the probability density function (PDF) for the pixel in i^{th} row and j^{th} column. An important property of FI is that it is additive and thus the summation denotes the addition of the FI over all the pixels of the detector. If the optical system is split in more than one channel (ex: using a beam splitter), the FI of the system is calculated by adding the FI of each channel. Different noise sources can be added by appropriately choosing the pdf. The $CRLB$ for the multivariable case is then given by,

$$CRLB_{\psi} [m] = FI_{\psi}^{-1} [m, m] \quad (2.11)$$

Another important measure of performance is the standard deviation which is just the square root of the variance. Thus the lower bound on the standard variation is given by the square root of the $CRLB$,

$$\sigma_{\psi} [m] = \sqrt{CRLB_{\psi} [m]} \quad (2.12)$$

The standard deviation directly yields the error lower bound in the same units as the measured data. We assume the imaging systems to be shift-invariant in the transverse direction, which is a good approximation in the central region of the field of view. Hence, the $CRLB$ remains constant with transverse shifts. For 3D imaging and localization, we are interested in the minimum localization volume. One measure of this uncertainty volume is

$$\sigma_{3D} = \frac{4\pi}{3} \sigma_x \cdot \sigma_y \cdot \sigma_z \quad (2.13)$$

Here, σ_x , σ_y , and σ_z represent the lower bound standard deviation along the three Cartesian co-ordinates and σ_{3D} is the volume ellipsoid generated by using the these standard-deviations as the three semi-principal axis. Similarly, for estimating the orientation of a dipole, we can define the solid angle error as,

$$\sigma_{\Omega} = \sin \Theta \cdot \sigma_{\Theta} \cdot \sigma_{\Phi} \quad (2.14)$$

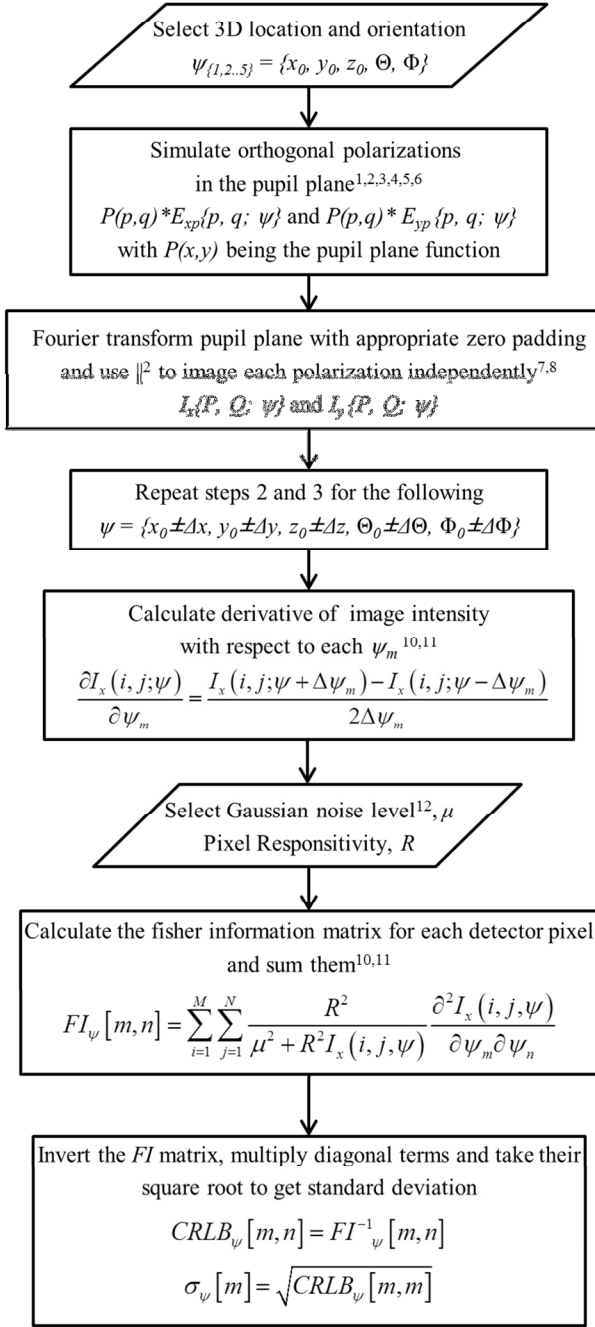
Here, σ_{θ} and σ_{ϕ} are the lower bound standard deviation for the polar and azimuthal angles and σ_{Ω} represents the solid angle of the cone generated using these values as the polar and azimuthal angles. Fixed dipoles lead to a 5-parameter estimation problem and defining the quantities in the above equations facilitates the analysis, comparison, and visualization.

2.3.2 Numerical calculation of CRLB

References [42] and [81] introduced information theoretic analyses for the study of the limits of precision in dipole orientation. In Ref. [42] we analyzed the 5D dipole estimation problem for the polarization system of Fig. 2.3(c). Meanwhile, Ref. [81] performed Fisher information calculations for orientation estimation using configurations that allow estimation of only one molecule at a time. Therefore the analysis did not include localization estimation or the effects of defocus. In contrast, here we analyze both the orientation and localization precision limits as functions of defocus and orientation for multiple configurations. All the systems analyzed allow for widefield imaging and hence the estimation of location and orientation of multiple dipoles in parallel.

As described in section 2.3.1, *CRLB* is a function of the fisher information (*FI*). In this section, we describe in greater detail the numerical computation of *FI*, followed by *CRLB* and standard deviation. A flowchart for calculating the *FI* matrix for a point dipole input is presented in Fig. 2.4.

Flowchart for calculating Fisher Information and error bounds



Assumptions

1. Image is continuous valued
2. Use Eq.2.1 and 2.2
3. Each pixel is a random independent variable
4. $P(x,y)$ is polarization insensitive.
5. $P(x,y) = 1$ for clear aperture
6. Pupil plane is $p \times q$ pixels
7. Zero padding determines the sampling rate
8. Detector has $P \times Q$ pixels
9. Each derivative step $\Delta\psi$ is chosen so that the derivative is independent of step size
10. For single channel the intensities are added before taking the derivative
11. For multiple channel systems, the FI is added for each channel before matrix inversion
12. Pure Poisson noise is simulated with $\mu=0$

Fig. 2.4 Flowchart for calculating the Fisher Information matrix, Cramer-Rao lower bounds and standard deviation for a general imaging system consisting of a single channel or polarization-sensitive system with multiple channels.

In order to calculate the *CRLB*, an accurate system model is required to generate the image $I(i, j; \psi)$ at the detector, where ψ represents the dipole input parameters. It should be noted that, depending on the system configuration, the image I could either represent the total intensity or the intensity of each channel of the imaging system separately. The image at the detector is calculated by accurately modeling the electric field in the pupil plane $P(p,q)*E_p(p,q;\psi)$ generated due a point dipole in the object space. Here, $p \times q$ represent the total no of pixels in the pupil plane, $P(p,q)$ represents the pupil plane function which allows for the inclusion of a phase/amplitude mask. The intensity at the detector due to each channel can be found by a two-dimensional Fourier transform of the field in the pupil plane. Given the image at the detector, the partial derivatives can be found using central difference methods,

$$\frac{\partial I}{\partial \psi_k} = \frac{I(\psi_k + \Delta\psi_k) - I(\psi_k - \Delta\psi_k)}{2\Delta\psi_k} \quad (2.15)$$

where $\Delta\psi_k$ is the numerical step size chosen for parameter ψ_k . To make sure that the derivative is independent of the chosen step size, it was calculated for decreasing step sizes and the step size where the derivative reaches the asymptotic limit was chosen. It was found that an appropriate step size for position variables (x_0, y_0, z_0) is 1 nm and 1 mrad for orientation variables (Θ, Φ). Once the partial derivatives are calculated w.r.t. to each of the five variables, the generalized *FI* matrix in eq. (2.10) can be reduced to an approximate form for joint Gaussian and Poisson processes in an imaging system as [82]

$$FI_\psi [m, n] \approx \sum_{i=1}^M \sum_{j=1}^N \frac{R^2}{\mu^2 + R^2 I(i, j; \psi)} \frac{\partial^2 I(i, j; \psi)}{\partial \psi_m \partial \psi_n} \quad (2.16)$$

where μ is the standard deviation of the Gaussian noise and R [Volts/photons] is the responsivity of the pixel. A pure Poisson noise model can be considered when $\mu=0$. The assumptions for the derivation of eq. (2.16) are that each detector pixel is considered to be an independent random event with uniform standard deviation across the detector array, which

allows for the addition of the FI across the pixels. This procedure is used for each channel of the system and the total FI of the system is obtained by adding them. The $CRLB$ is then obtained by inverting the FI matrix. The $CRLB$ values along the diagonal provide the estimator variances of each independent parameter and are frequently quoted when analyzing system performance. The standard deviation σ is then calculated taking the square root of the diagonal elements of the $CRLB$.

The number of photons captured by the objective lens depends on the numerical aperture and the orientation of the dipole with respect to the lens because the intensity of dipole radiation varies as $\sin^2\theta$, where θ is the angle from the axis of the dipole. Thus, a dipole that is perpendicular to the optical axis will have more photons detected than all other dipole orientations as long as the half-angle of the captured cone is less than 90° . Thus, among the representative orientations considered, the dipole along \hat{y} ($\Theta=90^\circ$ $\Phi=90^\circ$) will have the most photons captured and the pdf is normalized with respect to the dipole along \hat{y} for $CRLB$ calculations. We use a total of 5000 photons for the dipole perpendicular to the optical axis. It should be noted that the normalization of the captured photons based on dipole orientation does not affect the relative comparison of error bounds between different optical systems.

The $CRLB$ for the isotropic point emitter is calculated in a similar way using the Poisson noise model. But, since localization of an isotropic point source is a 3-parameter problem, the unknown parameter in this case is given by $\psi = [x_0, y_0, z_0]$ leading to a FI matrix of size 3×3 . The $CRLB$ comparison between a point source and a dipole emitter is presented in Appendix 2A to the chapter.

2.3.3 Estimation error bounds as a function of defocus

We compare the *CRLB* for dipole position and orientation in the shot noise limit using 5000 photons per image for the systems previously discussed. Fig. 2.5(a) and Fig. 2.5(b) show the average of the standard deviation for 3D position estimation (σ_{3D}) and solid angle estimation (σ_{Ω}) respectively, over the five¹ dipole orientations shown in Fig. 2.3(h). These are respectively denoted as $\text{avg}(\sigma_{3D})$ and $\text{avg}(\sigma_{\Omega})$. It can be seen from Fig. 2.5 that, for an in-focus molecule, the $\text{avg}(\sigma_{3D})$ and $\text{avg}(\sigma_{\Omega})$ for the single channel system [TI np: Fig. 2.3(b)] and the linear polarization system [Lin pol: Fig. 2.3(c)] increases rapidly, whereas for the elliptical system [Elp pol: Fig. 2.3(d)] they have a relatively smaller value. These high averages are due to the fact that near focus, these three systems carry either none or very little information about z -position variations of the dipoles that lie in the x - y plane ($\Theta=90^\circ$) and dipoles that are oriented along the optical axis ($\Theta=0^\circ$). Also, far from focus, the linear and elliptical polarization systems exhibit more precise localization than the total intensity system. On the other hand; the PS-DH system shows a finite $\text{avg}(\sigma_{3D})$ and $\text{avg}(\sigma_{\Omega})$ over the complete defocus range. In a smaller defocus range and away from focus, the $\text{avg}(\sigma_{3D})$ is less precise than the clear aperture polarization sensitive systems. As for the solid angle error, the PS-DH system has the lowest and most uniform $\text{avg}(\sigma_{\Omega})$. Thus, if we need uniform performance over a defocus range of $-z$ to $+z$, the widely used single channel system [8–10, 19, 20, 24] will not be the best candidates.

¹ For solid angle estimation, we average over four dipole orientations because for a dipole along the optical axis ($\Theta=0^\circ$), $\sin\Theta=0$, and the solid angle error is indeterminate

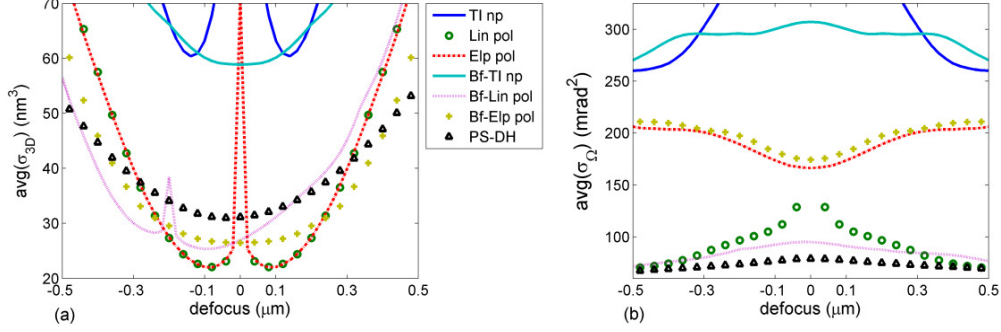


Fig. 2.5 Estimation error bounds as a function of defocus: (a) Average of volume localization - $\sigma_{3D}(4\pi/3 \cdot \sigma_x \cdot \sigma_y \cdot \sigma_z)$ (b) Average of Solid angle error - $\sigma_{\Omega}(\sin \Theta \cdot \sigma_{\theta} \cdot \sigma_{\phi})$ for the five representative dipole orientations with respect to the axial position of the dipole. For the bifocal systems, the two focal planes were offset by $0.4 \mu\text{m}$ and the x -axis represents the center of the two planes. The legends represent the systems compared here, namely single measurement-total intensity (TI np: solid blue), linear polarization (Lin pol: green o), elliptical polarization (Elp pol: red dash-dot), bi-focal total intensity (Bf-TI np: solid cyan), bi-focal with linear polarization (Bf-Lin pol: magenta dash), bi-focal with elliptical polarization (Bf-Elp pol: yellow +), and linear polarization system that used a double helix phase mask in the Fourier plane (PS-DH-Lin pol: black Δ).

In order to analyze the bi-focal systems, a defocus of $0.4 \mu\text{m}$ was chosen by optimizing the average *CRLB* for the dipole oriented along O3: ($\Theta=45^\circ$, $\Phi=45^\circ$). This orientation was chosen since it gives a finite *CRLB* for all the different systems and for all defocus values. Among the three bi-focal systems, the system that measures the total intensity has a substantially higher $\text{avg}(\sigma_{3D})$ and $\text{avg}(\sigma_{\Omega})$ throughout the defocus region compared to the bi-focal systems that employ polarization. The bi-focal systems with linear and elliptical polarization present a more uniform curve in the region of interest with the linear polarization system showing a lower *CRLB* than the elliptical one for solid angle estimation. It is noteworthy that the bi-focal linear curve is asymmetric about $z_0=0$ and has a spike at defocus $-0.2 \mu\text{m}$. Since the radiation of a dipole is linearly polarized, the E_x channel of the bi-focal linear system, for a dipole along \hat{y} ($\Theta=90^\circ$, $\Phi=90^\circ$), has no information at focus and this coupled with the E_y channel at $z_0=-0.4 \mu\text{m}$ results in a spike in the *CRLB* curve at $z_0=-0.2 \mu\text{m}$. Thus, for 3D localization, depending on the region of

interest, either the bi-focal elliptical system or one of the single-plane linear or elliptical systems would be suitable candidates. However, for orientation estimation, the PS-DH system shows the lowest *CRLB* among the systems considered followed closely by the bi-focal linear polarization system.

2.3.4 Estimation error bounds as a function of azimuthal and polar angles

Localization and orientation estimation of a dipole are functions of both, the dipoles position and orientation. In Fig. 2.6, we show the lower bound of the standard deviation for volume localization (σ_{3D}) and the orientation solid angle (σ_{Ω}) for a dipole with respect to the azimuthal and polar angles. Fig. 2.6(a) and (b) show σ_{3D} and σ_{Ω} respectively, with the top row displaying them as a function of angle Φ for $\Theta=90^\circ$, and the bottom row displaying them as a function of angle Θ for $\Phi=0^\circ$. Note that at $\Theta=90^\circ$ an in-focus dipole has rapidly increasing *CRLB*, thus these plots were made for a defocus of $z_0=0.1 \mu\text{m}$ to gain a qualitative insight. Both σ_{3D} and σ_{Ω} have a nearly constant *CRLB* for all seven systems as a function of azimuthal angle Φ . For estimation of the solid angle, the Lin pol, the Bf-Lin pol system and the PS-DH system show the lowest *CRLB* followed by the Elp pol and TI np systems. Indeed, as the dipole rotates in Φ , the intensity distributions of the (Bf-)TI np and the (Bf-) Elp pol system rotate, thus rotating the major-axis of the elliptical pattern of the dipole emission, whereas for the (Bf -) Lin pol and PS-DH systems, there is energy exchange between the two channels. As for volume localization, the Elp pol and Lin pol systems that focus at the same plane have a better precision but only over a short range in the axial dimension (see Fig. 2.5(a)).

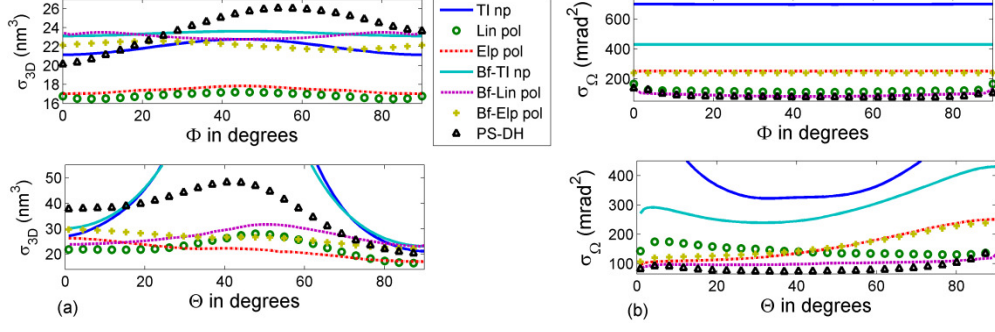


Fig. 2.6 Estimation error bounds as a function of dipole orientation angle: (a) Volume localization - $\sigma_{3D}(4\pi/3 \cdot \sigma_x \cdot \sigma_y \cdot \sigma_z)$ and (b) Solid angle error - $\sigma_{\Omega}(\sin \Theta \cdot \sigma_{\Theta} \cdot \sigma_{\Phi})$ as a function of the azimuthal angle Φ (top row) and polar angle Θ (bottom plot). For the plots of category A, where system collects information from a single focal plane chosen at a defocus $z_0 = 0.1\mu\text{m}$. For plot against Φ the angle $\Theta = 90^\circ$ and for the plots against Θ the angle Φ was chosen to be 0° . For the bifocal systems, the two focal planes were offset by $0.4\mu\text{m}$ and the x -axis represents the center of the two planes. The legends represent the systems compared here, namely single measurement- total intensity (TI np: solid blue), linear polarization (Lin pol: green o), elliptical polarization (Elp pol: red dash-dot), bi-focal total intensity (Bf-TI np: solid cyan), bi-focal with linear polarization (Bf-Lin pol: magenta dash), bi-focal with elliptical polarization (Bf-Elp pol: yellow +), and linear polarization system that used a double helix phase mask in the Fourier plane (PS-DH-Lin pol: black Δ).

The bottom row in Fig. 2.6 shows the volume and solid angle estimation precision w.r.t to the polar angle Θ . As shown in Fig. 2.6(a), for volume localization w.r.t. Θ , all systems except the non-polarization sensitive systems provide a pretty uniform and low $CRLB$, implying a better lower bound for estimation error. On the other hand, from Fig. 2.6(b) it can be seen that, as a function of Θ , the estimation of the solid angle becomes difficult using the non-polarization sensitive systems, whereas the PS-DH system has the smallest lower bound in estimating the solid angle. Thus, overall the PS-DH system has the lowest and most uniform σ_{Ω} for solid angle estimation but not far from the Bf-Lin pol system.

2.3.5 Estimation error bounds as a function of defocus and polar angle

For shift invariant systems, σ_{3D} and σ_{Ω} are in general functions of Θ , Φ , and z . Therefore, they could be represented in a 3D space for joint optimization. The cross sections

presented in Fig. 2.5 and Fig. 2.6 are representative of the behavior of the systems and help identify the best systems. However, the 2D plots were either averaged for a representative set of dipole orientations or computed only for fixed orientation or defocus parameters. A more complete representation would be to study the volume and solid angle errors as functions of all three variables. However, such a plot would be visually challenging to represent. It was seen in Fig 2.5 that the estimation error bounds were a relatively slowly varying function of the azimuthal angle Φ . Therefore, we calculate the error bounds as a function of the three variables and for each z and Θ , we find the maximum and minimum error bounds for all Φ , thus making it possible to visualize the error bounds as surface plots. As shown in Fig. 2.7(a) and Fig. 2.7(b), the lower bounds for the commonly used single channel imaging system [8–10, 19, 20, 24] and the best two-channel systems identified above are represented as surface plots as functions of z and Θ . These plots show the striking improvement in precision achievable by design via the *CRLB* metric. Typical improvements are threefold in 3D position estimation and fourfold in orientation estimation. It is also noteworthy that even when the azimuthal angle is spanned through a rotation of 2π , the improvements in the estimation remain nearly unchanged. Also from Fig. 2.5(a) it can be seen that the Bf-Elp pol system has a more uniform *CRLB* than the Lin pol system, although it performs worse near focus. We compare the volume localization of these two systems as a function of polar angle and defocus in Fig. 2.7(c). Similarly, for solid angle error (Fig. 2.6), the PS-DH system and the Bf-Lin pol system are the strongest contenders. In Fig. 2.7(d) we compare these two systems as functions of defocus and polar angle Θ . This analysis can be extended to include parametric surfaces as a function of specific system parameters, such as number of photons, background noise, etc., which could be used for further system optimization.

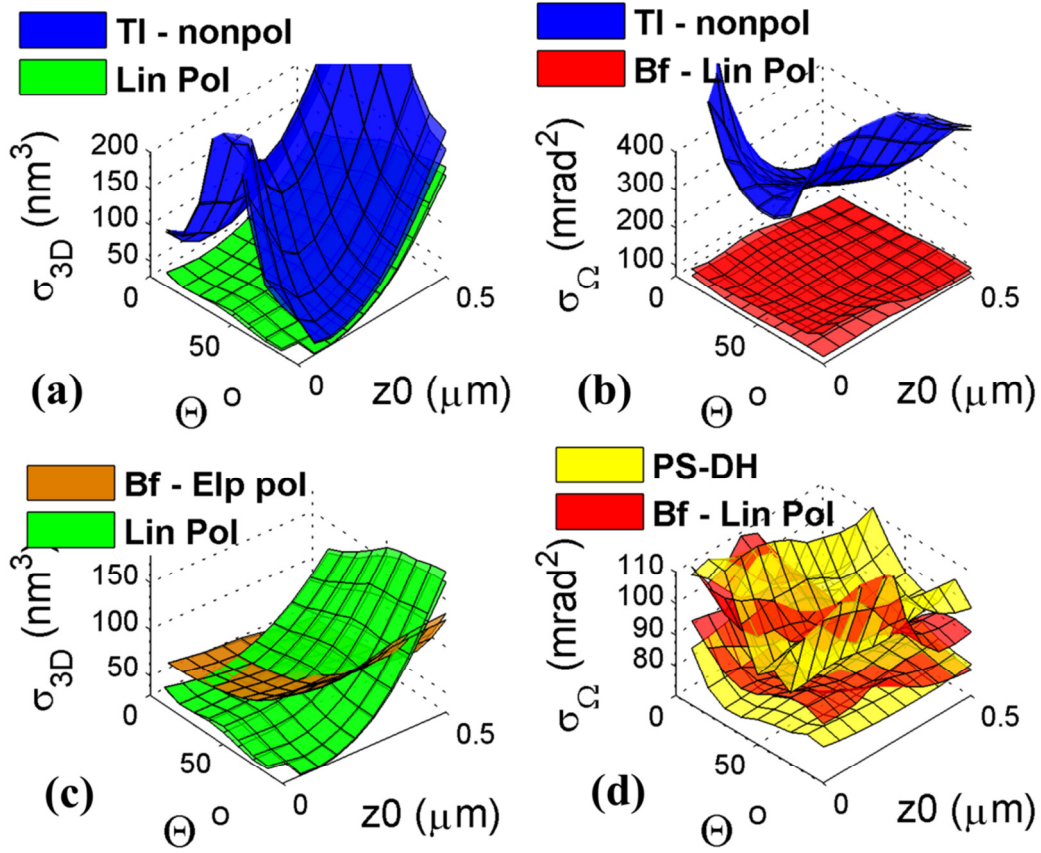


Fig. 2.7 3D localization and orientation estimation design via the *CRLB*: Parts (a) and (c) show the volume localization lower bound- $\sigma_{3D}(4\pi/3 \cdot \sigma_x \cdot \sigma_y \cdot \sigma_z)$. Parts (b) and (d) show the solid angle lower bound error - $\sigma_{\Omega}(\sin \Theta \cdot \sigma_{\Theta} \cdot \sigma_{\Phi})$ as a function of the polar angle Θ and defocus (z_0). Each system considered here is represented by a unique color and for each system (color), the two surface plots represent the maximum and the minimum error calculated over all azimuthal angles Φ . The systems compared in the above plots are the single channel total intensity system (TI np: blue surface), Linear polarization system (Lin Pol: green surface), bifocal linear polarization system (Bf-Lin Pol: red surface), bifocal elliptical polarization system (Bf-Elp Pol: brown surface), linear polarization with the DH mask (PS-DH: yellow surface), and the DH system for the isotropic emitter (Iso-DH: cyan surface). For the bifocal system, the two focal planes are separated by the distance $d_z=0.4 \mu\text{m}$ and z_0 represents the center of the two planes.

2.4 Experimental validation using a double-helix mask

In the previous sections we show that the Green's function for a dipole input can be efficiently engineered by either using simple polarization optics or by using phase masks that can

encode the information in a non-standard form or a combination of both. Particularly, the double-helix point spread function (DH-PSF) stood out as a strong candidate for simultaneously estimating a dipole's position and orientation. Both the volume and solid angle *CRLBs* of the DHPSF showed superior performance over the defocus range of 2 microns. Moreover, since the DH-PSF mask itself works by imparting a sizeable distortion on the wavefront, the associated images are more robust to minor disturbances of the wavefront caused by aberrations[31].

The results described in this section were performed in collaboration with Ginni Grover, Sean Quirin, and W. E. Moerner's group at Stanford, including Matthew Lew, Michael Backlund, Adam Backer and Steffen Sahl. Experiments were performed both at CU-Boulder and Stanford University. My participation was in simulating the response and the *CRLB* of the DHPSF, in general discussions, and in the experiments performed at CU-Boulder.

2.4.1 Experimental setup

The experimental setup consisted of a standard microscope that creates an image at the intermediate plane (IIP) followed by a 4f system. The DHPSF was placed in the Fourier plane of the 4f system owing to the fact that the phase mask has been optimized to perform at its best at the Fourier plane. A phase-only reflective liquid crystal spatial light modulator (SLM)[83]–[85] is used to realize the DHPSF. This type of SLM can only modulate vertically polarized, hence the emission was split by a polarizing beamsplitter and the horizontally polarized channel was rotated with a half wave plate. Each polarization channel was then reflected separately off the SLM[86]. To ensure maximal channel symmetry between the two polarization channels, a novel setup was used as shown in Fig. 2.8B. The square pyramidal mirror is used to deflect the beams out of the plane into the w direction (as marked in Fig. 2.8B-D) and onto the SLM mounted from above with its face toward the mirror (Fig. 2.8C-D). This forces the two polarization channels to

have the same angle of incidence on the SLM. For each measurement, the phase mask was used in two orthogonal orientations (Fig. 2.8B inset) for reasons described below.

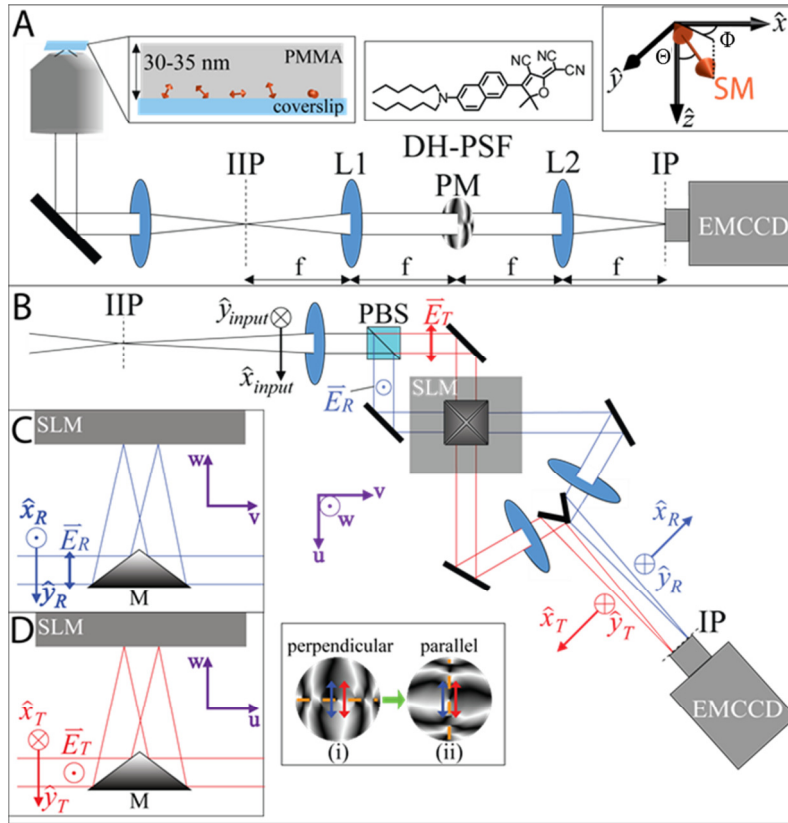


Fig. 2.8 DH-PSF imaging system. (A) $4f$ optical system schematic, where IIP is the intermediate image plane formed by a standard inverted microscope, L1 and L2 are focal-length-matched achromatic lenses, DH-PSF PM is the DH-PSF phase mask, and IP is the resulting image plane that is recorded on an EMCCD camera. The sample for the experiments described consisted of DCDHF-N-6 molecules (middle inset) embedded in a thin layer of PMMA (left inset). Orientation angles (Θ , Φ) are defined in the right inset and have ranges $[0, 90^\circ]$ and $[-180, 180^\circ]$, respectively. (B) The high efficiency dual-polarization detection DH-PSF setup used for these experiments (inverted microscope omitted for simplicity). The collected fluorescence is split by a polarizing beamsplitter (PBS) into reflected (R, blue) and transmitted (T, red) channels. Input Cartesian unit vectors $(\hat{x}_{input}, \hat{y}_{input})$ define molecular orientation (Θ , Φ) and are propagated differently through the various reflections in the two polarization channels $((\hat{x}_R, \hat{y}_R)$ and (\hat{x}_T, \hat{y}_T)). The two electric field polarization axes \vec{E}_R and \vec{E}_T are projected identically onto the phase mask (inset). The inset shows how each polarization axis (blue and red arrows) is oriented relative to the mask's axis of phase discontinuities (dashed orange) when the mask is upright (i; polarization perpendicular to discontinuities) and rotated (ii; polarization parallel to discontinuities). (C-D) Two side-on views of the SLM portion of the setup, showing the square pyramidal mirror (figure extracted from [45]).

The simulations of DH-PSF dipole response show dependence on \bar{E} -field polarization (Fig. 2.2) due to the asymmetry of the phase mask. However, the polarization axis of each polarization channel is identical in the SLM plane due to the geometry of the setup. Therefore depending on the orientation of the mask both the channels are rendered with either parallel or perpendicular type behavior (Fig. 2.8B inset). Thus to capture the full behavior of the DH-PSF response to dipole emission patterns, each single molecule was measured with the mask oriented upright (perpendicular) and also with the mask rotated by 90° (parallel). Since the molecular coordinates are projected differently onto the mask in the two channels, none of these four images are identical and they do not convey degenerate information. Hence, non-degenerate information is provided from four different images (two acquisitions of two polarization channels) of each single molecule to produce a single estimate of the molecule's position and orientation.

2.4.2 Cramer-Rao lower bound for four channel Double Helix system.

As described in the previous section, the setup shown in Fig. 2.8 is effectively a four channel system where two of the channels are imaged using one orientation of the DHPSF phase mask and the other using an orthogonal variation of it. Here we quantitatively compare it to established methods that use a clear aperture, standard PSF system[39], [71]. We calculate the photon-limited precision that can be achieved in estimating the position and orientation of a dipole using the Cramer Rao Lower Bound (*CRLB*)[87].

For the *CRLB* simulation, the dipole is assumed to be immersed in a medium of index 1.52 (no interface) and the emission wavelength is at $\lambda = 610$ nm. The objective lens has a NA of 1.4. The pixel size is 160 nm in the object plane. In all calculations, the number of photons detected in the standard system is the same as that in the DH-system, properly divided among the four channels.

Fig. 2.9 shows the orientation (σ_Θ and σ_Φ) and 3D localization (σ_{3D}) error lower bounds as a function of the polar angle (Θ), with and without background. The amount of defocus for either system is chosen to optimize the precision based on the lowest *CRLB*. Thus, the axial defocus for the standard (clear aperture) system is $z_0 = 100$ nm, whereas the DH-system performs best at focus ($z_0 = 0$). Our calculations also show that the localization and orientation errors are relatively constant as a function of the polar angle Φ . In order to make a fair comparison we choose $\Phi = 45^\circ$ in Fig. 2.9 to evenly distribute the light between the two linear polarization channels.

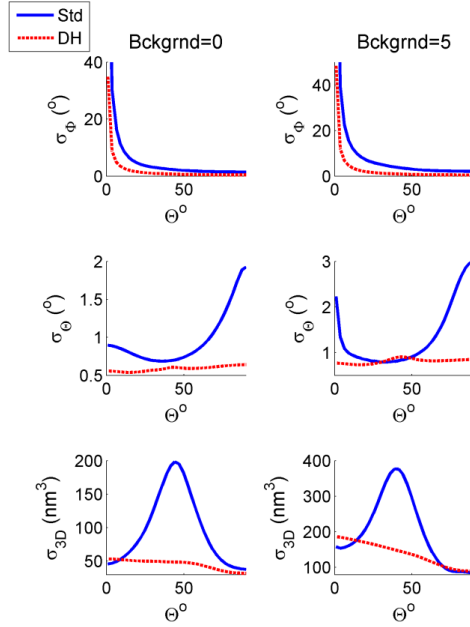


Fig. 2.9 Lower bound of the precision (standard deviation) for estimating the azimuthal angle (σ_Φ), polar angle (σ_Θ), and the 3D position (σ_{3D}) w.r.t to the polar angle theta (Θ). Blue solid curves represent the standard PSF case and dashed red curves represent the DH case. The plots on the left are shown for zero background whereas the ones on the right have background of 5 photons per pixel. The standard PSF case is defocused by 100nm, and the DH case is in focus. The polar angle in both cases is $\Phi=45^\circ$.

It can be clearly seen that the DHPSF outperforms the standard system for both localization and orientation precision over the complete range of orientation angles considered

here. For polar angles approaching 0° , the standard system seems to have slightly better precision but the difference is negligible in comparison to the performance over the considered range. In presence of background the precision worsens but DHPSF still stands out as a better candidate for estimating both the location and orientation. The standard system performance is calculated for the optimal defocus so it will substantially deteriorate with variations in z . On the contrary, the DH system has a slower variation with defocus and hence provides a relatively uniform performance with defocus.

The precision lower bounds w.r.t to defocus for the two systems, with and without background, is shown in Fig. 2.10. Since the polar angles have a substantial effect on the precision lower bounds, we show the lower bounds for dipole oriented (A) Perpendicular to the optical axis ($\Theta, \Phi = 90^\circ, 90^\circ$) and (B) dipole oriented at $(\Theta, \Phi) = (45^\circ, 45^\circ)$. The lower bound of the error for angle estimation and 3D position using the four-channel polarization-sensitive DH system is substantially lower than that of the standard PSF case. It can be seen that the DH-system performs better than the standard system over most of the defocus range with and without background. Moreover, for dipoles oriented perpendicular ($\Theta = 90^\circ$) to the optical axis, the standard system fails to precisely locate dipoles in focus and the best estimate of the dipoles position is the depth of focus. But owing to the rotating nature of the DHPSF, the DH-system does not suffer from the precision loss.

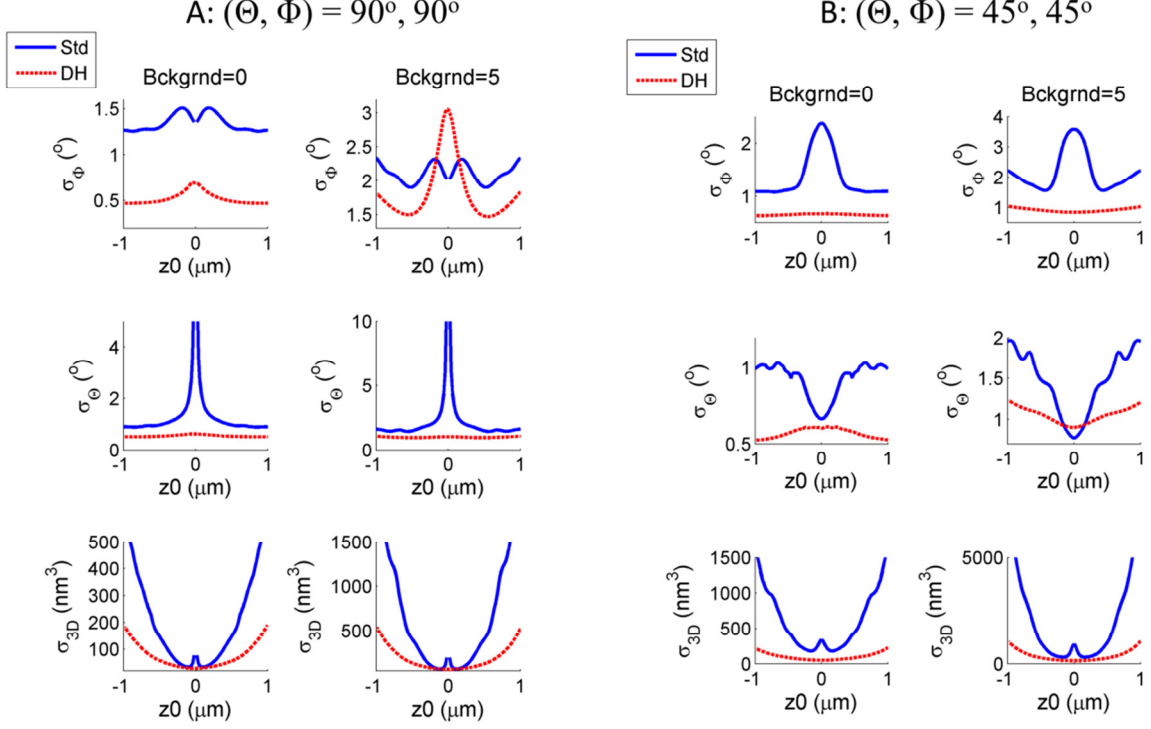


Fig. 2.10 Lower bound of the precision (standard deviation) for estimating the azimuthal angle (σ_ϕ) polar angle (σ_θ), and the 3D position (σ_{3D}) w.r.t to defocus (z_0) for a dipole oriented along (A) $\Theta=90^\circ, \Phi=90^\circ$ and (B) $\Theta=45^\circ, \Phi=45^\circ$. Blue solid curves represent the standard PSF case and dashed red curves represent the DH case. The plots on the left are shown for zero background whereas the ones on the right have background of 5 photons per pixel.

As described earlier, the error bounds are a relatively constant function w.r.t to the azimuthal angle. Moreover, we assume that the optical systems are shift invariant. Thus, the variation of precision error is small w.r.t to the transverse co-ordinates (x, y). Therefore, we plot both the solid and volume angle error as functions of the defocus and polar angle with and without background using surface plots as shown in Fig. 2.11. These plots help visualize the improvements the DH system provides over that of the standard ones. With increase in background, the standard system has a slightly better precision for dipoles aligned along the optical axis but rapidly decreases as the orientation angle changes. The volume precision shows about 2-3x improvement whereas a 3-4x improvement is seen in estimating the solid angle. Thus it can be concluded that the polarization sensitive 4-channel DHPSF system can significantly

improve the precision in estimating the dipole's parameters as compared to the commonly used standard system.

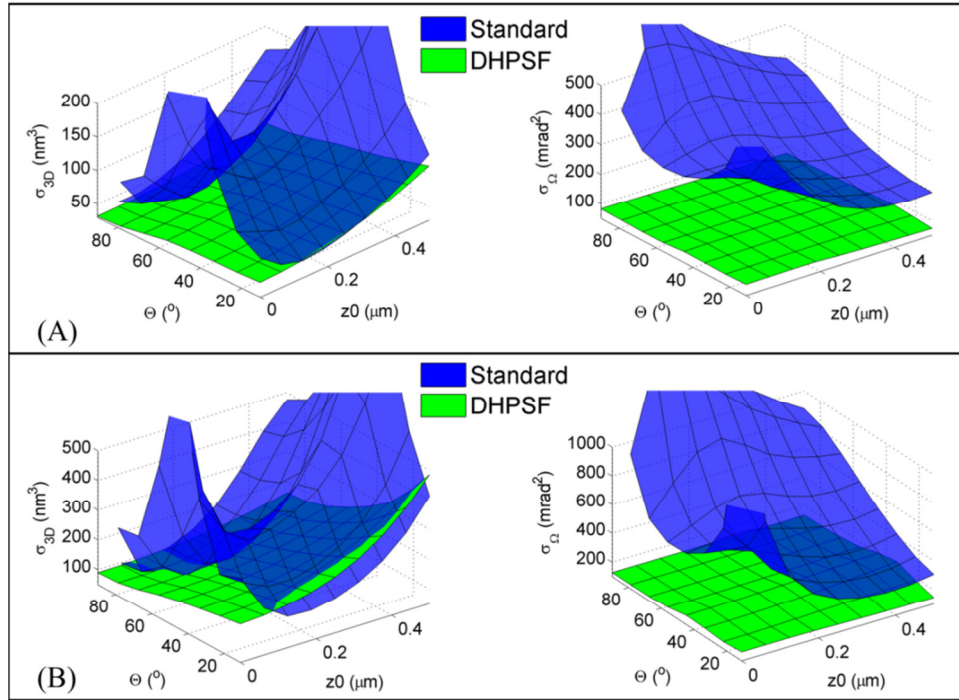


Fig. 2.11 Surface plots showing the lower bound of the precision (standard deviation) for estimating the 3D position (σ_{3D}) and solid angle (σ_{Ω}) w.r.t to defocus (z_0) and is polar angle (Θ).

(A) Zero background noise. (B) Background of 5 photons/pixel. Blue surfaces represent the standard clear aperture system whereas the green surfaces represent the 4-channel double helix system used for this experiment.

2.4.3 Estimation parameters

It was shown earlier that as the emitter is moved in z , the two lobed PSF of double helix phase mask [37], tracing out a double helix along the optical axis. The z -position is encoded in the rotation angle and the transverse position is encoded in the location of the two lobes. As described earlier, the emission of fixed dipole is polarized along its dipole momentum. Therefore, splitting the emission into orthogonal polarization channels yields some information about the azimuthal (Φ ; Fig. 2.8A inset) orientation based on the computed linear dichroism,

$$LD = \frac{N_T - N_R}{N_T + N_R} = \cos(2\Phi) \quad (2.17)$$

Where N_T and N_R are respectively the numbers of photons detected above background in the transmitted and reflected polarization channels defined relative to the PBS (Fig. 2.8B). To measure polar orientation (Θ ; Fig. 2.8A inset), another parameter must be measured which is offered by the DH-PSF, namely, the relative intensity of the two lobes of the DH-PSF which is a function of (z, Θ, Φ) of a single molecule emitter. Unlike an isotropic emitter that yields lobes of equal intensities for all z , the dipole emitter exhibits large lobe asymmetries that depend on (z, Θ, Φ) as show in Fig. 2.2. We quantify the lobe asymmetry as

$$LA = \frac{A_{L1} - A_{L2}}{A_{L1} + A_{L2}} \quad (2.18)$$

in which A_{L1} and A_{L2} are the amplitudes of lobes 1 and 2 of the DH-PSF, respectively. By measuring (z, LD, LA) from DH-PSF images of an emitter, we are thus able to determine the molecule's orientation.

2.4.4 Methods

The sample consisted of DCDHF-N-6[88] spun in thin (30-35 nm by ellipsometry) layer of PMMA which restricted the motion of molecules effectively making them dipole sources. The objective was scanned over a 2 μm depth range centered about the focal plane in steps of 50 nm. Images were recorded at every z -step such that for each SM, many different sets of observables $(x_{\text{apparent}}, y_{\text{apparent}}, z, LA, LD)$ were recorded. From each single measurement of this set, the orientation and 3D position were estimated using the prescription provided by the simulated images of $(x_{\text{apparent}}, y_{\text{apparent}}, z, LA, LD)$ for each orientation and defocus, ultimately subtracting lateral shifts $(\Delta x, \Delta y)$ from the apparent positions. Since we do not expect the orientation or lateral position of a SM to change on our imaging timescale for PMMA at room temperature, each independent measurement should produce the same $(x_{\text{true}}, y_{\text{true}}, \Theta, \Phi)$ within some precision.

In other words, our method is validated if the determined $(x_{true}, y_{true}, \Theta, \Phi)$ of a SM are each constant functions of z .

Using the DH-PSF-based method, the orientation of six molecules (two are shown in Fig. 2.12, the other four are described in the SI of Ref. [89]) was estimated. To distinguish the four images colors were assigned to each mask orientation/polarization channel combination: mask parallel/transmitted polarization is the “red channel”, mask perpendicular/transmitted polarization is “gold”, mask parallel/reflected polarization is “green”, and mask perpendicular/reflected polarization is “blue”. Fig. 2.12A and C show representative images of the DH-PSF for each example molecule in the four channels at a single z position, while Fig. 2.12B and D show the corresponding clear-aperture defocused images. For both example molecules, each measurement of LD (Fig. 2.12E-F) and LA (Fig. 2.12G-H) as a scatter point plotted vs. z are shown. For each quartet of LA measurements and associated LD measurements, there is a corresponding estimation of (Θ, Φ) . The mean orientation of the Gaussian fit of these distributions of (Θ, Φ) yields the solid overlays in Fig. 2.12E-H. The full distributions of DH-PSF-extracted (Θ, Φ) are shown in Fig. 2.12I-J. Also displayed for each molecule in Fig. 2.12 is the orientation estimated from the independent defocused measurement (purple arrows). We see excellent agreement between the defocus-determined orientation and the DH-PSF-based measurements: $(\Theta_{DH-PSF} = 42^\circ \pm 12^\circ, \Phi_{DH-PSF} = -76^\circ \pm 7^\circ)$ and $(\Theta_{defocus} = 40^\circ \pm 2^\circ, \Phi_{defocus} = -81^\circ \pm 4^\circ)$ for molecule 1; $(\Theta_{DH-PSF} = 61^\circ \pm 2^\circ, \Phi_{DH-PSF} = 141^\circ \pm 4^\circ)$ and $(\Theta_{defocus} = 63^\circ \pm 3^\circ, \Phi_{defocus} = 143^\circ \pm 5^\circ)$ for molecule 2.

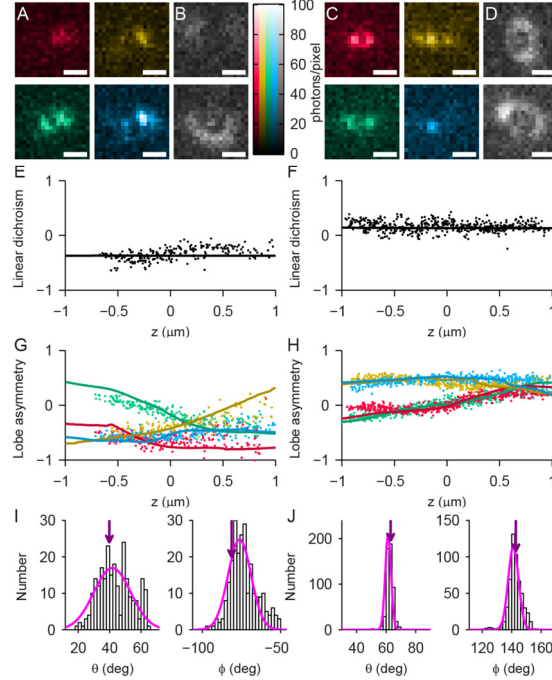


Fig. 2.12 Orientation fitting results for example molecule 1 (left column) and example molecule 2 (right column). All scale bars 1 μm . (A) Four example DH-PSF images (which constitute one measurement of orientation) of molecule 1 at $z \approx -250$ nm as it appears in each of four mask orientation/polarization channel combinations: parallel/transmitted (red), perpendicular/transmitted (gold), parallel/reflected (green), and perpendicular/reflected (blue). Note that only one lobe is easily visible in the red and gold channels. (B) The transmitted (top) and reflected (bottom) polarization defocused standard PSF images used for independent orientation measurement. (C) The equivalent of (A) for example molecule 2 at $z \approx 0$ nm. (D) The equivalent of (B) for example molecule 2. (E-F) Each measurement of LD (scatter) and the predicted LD based on the mean fit orientation (solid) for each molecule. (G-H) Each measurement of LA in each channel (color code same as in A) and the overlaid predicted LA for the mean fit orientation. (I-J) Histograms of Θ and Φ extracted from DH-PSF based measurements. Magenta line is Gaussian fit, which gives mean values ($\Theta_{DH-PSF} = 42^\circ \pm 12^\circ$, $\Phi_{DH-PSF} = -76^\circ \pm 7^\circ$) (error is S.D.) for molecule 1 and ($\Theta_{DH-PSF} = 61^\circ \pm 2^\circ$, $\Phi_{DH-PSF} = 141^\circ \pm 4^\circ$) for molecule 2. Purple arrow denotes orientation extracted from defocused imaging: ($\Theta_{defocus} = 40^\circ \pm 2^\circ$, $\Phi_{defocus} = -81^\circ \pm 4^\circ$) for molecule 1 and ($\Theta_{defocus} = 63^\circ \pm 3^\circ$, $\Phi_{defocus} = 143^\circ \pm 5^\circ$) for molecule 2 (figure extracted from [45]).

Thus using the DHPSF, the dipole orientation and location were estimated within the limits of acceptable standard deviations and the measurements were further validated using clear aperture defocused images of the same. This was the first demonstration of simultaneous measurement of the 5D parameters associated with dipole imaging.

In the next section we show the vortex phase mask as another example of engineering the Green's tensor, and also present alternatives to the SLM implementation of phase mask to simplify optical design and capture light efficiently from single molecule emitters.

2.5 Engineering the Green's tensor using a spiral (vortex) phase mask

In the previous sections it was seen that the Green's tensor of a dipole input can be efficiently engineered to extract information about the dipole position and orientation using the double-helix point spread function (DHPSF). The phase singularities induced by the DHPSF phase mask causes redistribution of energy from an airy-disc like PSF to a double lobed pattern that has a null in the center. The DHPSF was designed by superimposing the propagating modes in the Laguerre-Gaussian modal plane and optimizing the PSF over a range of defocus values[90]. However, it was later shown that similar double-lobed patterns can be realized by generating phase masks using strategically placed phase discontinuities[91]. The simplest form of a phase discontinuity is the well-known spiral (vortex) phase which is also the (1, 0) mode of the Laguerre polynomials. There has been a growing interest in the generation and applications of the vortex beams in optical microscopy[92], optical cooling and trapping[93], [94], optical tweezers[95]–[97]. In this section we study the vortex phase mask vis-à-vis dipole localization and orientation estimation

As the name suggests, the spiral phase has an azimuthal phase variation given by $\exp(-im\varphi)$, where φ is the azimuthal angle and m is an integer known as the charge of the spiral phase. When $m=1$, we get the single charge spiral phase shown in Fig. 2.13(a). The point source response of the spiral phase is the doughnut shaped intensity distribution profile shown in Fig. 2.13(b). As the point source is defocused axially, the central null of the vortex distribution

remains unchanged and a relatively tighter intensity distribution is observed as compared to the airy-disc. From here on, we will refer to the spiral phase profile as vortex mask.

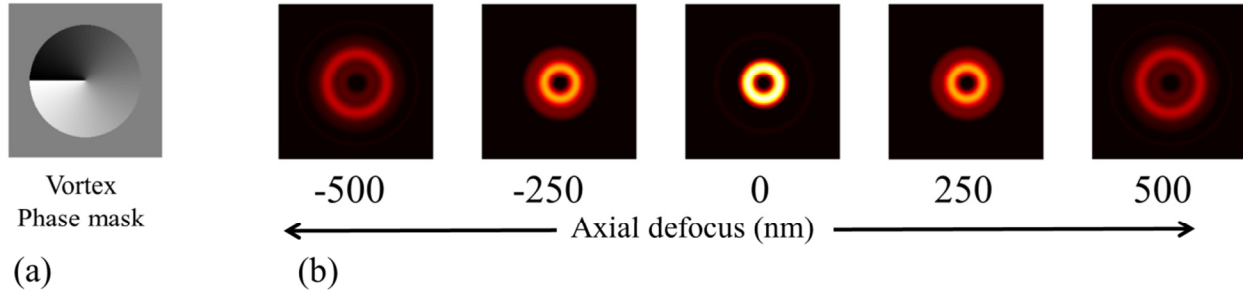


Fig. 2.13 Simulation of PSF of a spiral (vortex) phase mask: (a) Phase of the spiral phase mask. (b) PSF of the spiral phase as a function of defocus.

The simulation of the intensity distribution for a single channel total intensity system and the polarization sensitive two channel systems using the vortex phase mask along the three representative dipole orientations is shown in Fig. 2.14. Here, (a) shows the distribution for a dipole in focus and (b) for a dipole $0.2 \mu\text{m}$ from focus. For a dipole oriented along the optical axis ($\Theta=0^\circ \Phi=0^\circ$), the response looks similar to the response of a point source but has a smaller spread as it is defocused. For dipoles perpendicular to the optical axis ($\Theta=90^\circ \Phi=90^\circ$) it exhibits the characteristic donut profile that gets skewed with defocus, whereas for intermediate orientations $\Theta=45^\circ \Phi=45^\circ$ a crescent shaped image of the dipole is seen. The images suggest that unlike the standard optical system, the response of the vortex phase mask varies continuously as the dipole traced through focus. The *CRLB* curves shown in the next section further clarify this effect.

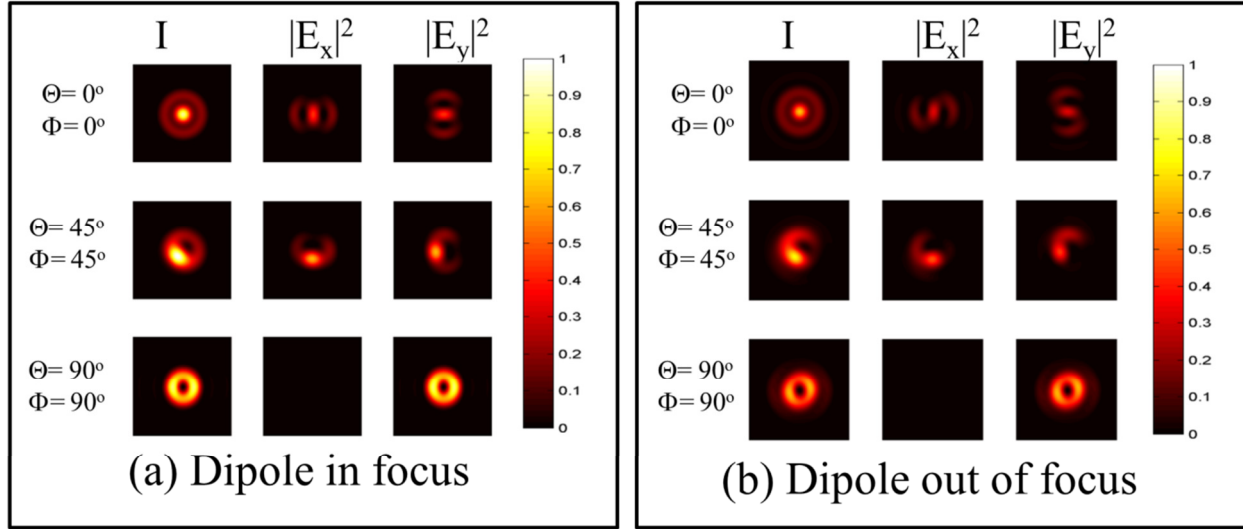


Fig. 2.14 Simulation of the dipole spread function along three representative orientations using Vortex phase mask: (I) is the detected total Intensity (single channel system), $|E_x|^2$, $|E_y|^2$, (left to right) correspond to images obtained in two-channel systems when using orthogonal polarizers. In (a), the dipole is at the focal plane, while in (b) it is located $0.2 \mu\text{m}$ from the focal plane. The dipole is oriented along (from top to bottom) \hat{z} ($\Theta=0^\circ \Phi=0^\circ$), $\Theta=45^\circ \Phi=45^\circ$, and \hat{y} ($\Theta=90^\circ \Phi=90^\circ$)

2.5.1 CRLB for the vortex phase mask

In this section, we compare the estimation lower bounds of the Vortex phase mask with that of the DHPSF and the clear aperture system. Since it has already been established that polarization sensitive systems are superior to total intensity systems, we compare them using the two channel orthogonal polarization systems. The *CRLB* is calculated in the shot noise limit with a total of 5000 photons and a background of five photons/pixel. As shown in Fig. 2.15, (a) represents the average of the volume standard deviation along the five representative orientations whereas (b) represents the solid angle standard deviation; both as a function of defocus (z_0). Plots (c) and (d) show these as a function of polar angle Θ . The error bounds are relatively constant as a function of azimuthal angle Φ and do not convey any new information. The three curves shown represent the linear-polarization system (solid blue), polarization sensitive DHPSF (dot-dashed green), and vortex phase mask (dashed red).

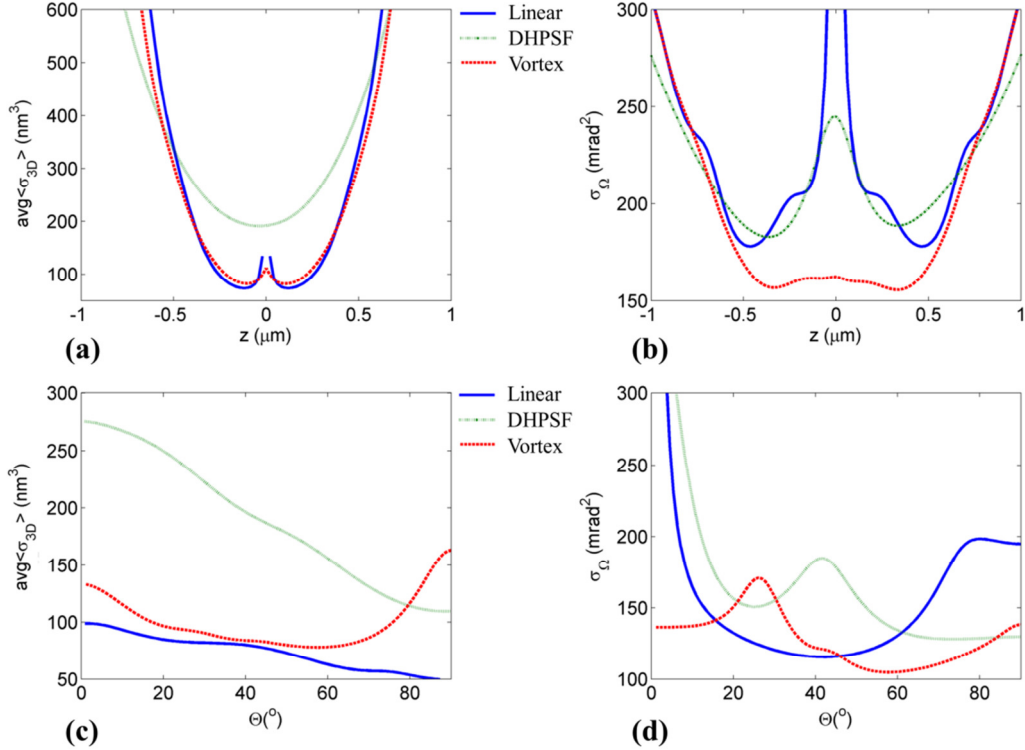


Fig. 2.15 Estimation error bounds for the vortex phase mask: The figure shows the lower bound of the standard deviation for the vortex phase mask (dashed red), DHPSF (dot-dashed green) and the two channel linear polarization system (solid blue). The top row represents the error bounds as a function of defocus and the bottom row shows them as a function of polar angle Θ . The left column is the average of the volume standard deviation along the five representative orientations shown in Fig. 2.3(i). The right column is the solid angle standard deviation.

The linear polarization system exhibits the smallest error lower bound but since the standard PSF does not change near focus, the best estimate, for dipoles perpendicular to the optical axis, is the depth of focus. This translates to an infinity at the focus in the volume standard deviation curve. The vortex phase mask on the other hand shows a pretty low and uniform performance over the range of defocus and polar angle. Moreover, the vortex phase mask does not suffer from depth of defocus problem. A surface plot showing the comparison of the vortex and DHPSF is shown in Fig. 2.16. It is clear from these plots that the vortex phase mask uniformly performs better than the DHPSF within the defocus range of 0-0.5 μm and for polar angles between 0° to 90°

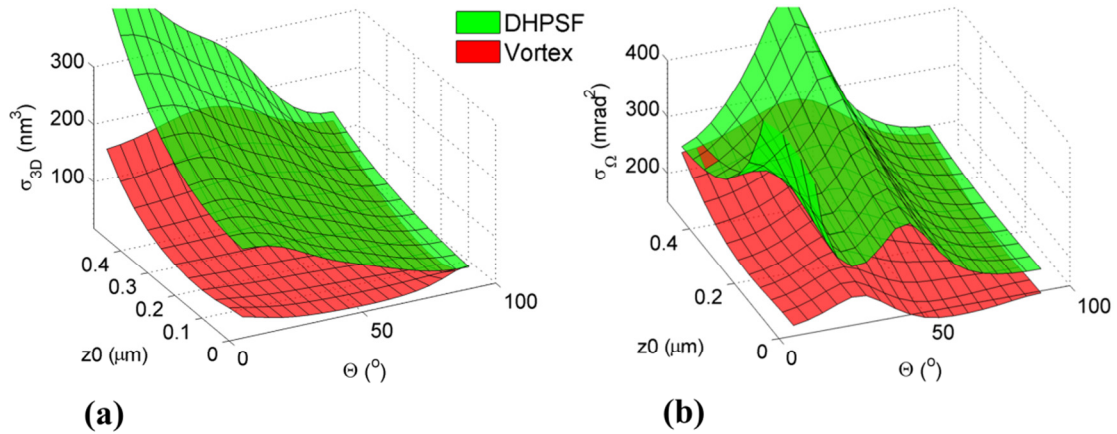


Fig. 2.16 Surface plots of the error bounds for vortex phase mask and DHPSF: The plot shows the volume (left) and solid angle standard deviation for vortex phase mask and DHPSF as a function of polar angle (Θ) and defocus (z_0).

2.5.2 Implementation in an imaging system

The vortex phase mask was implemented in a 4f relay system added to a standard microscope. The setup is similar to that shown in Fig. 2.8(A) except that instead of implementing the phase mask using the SLM, a 16-level vortex phase mask is fabricated using the binary multi-level exposure method. The fabrication details are given in Chapter 3. A 1.4 NA objective is used with a 100x magnification to image both point sources and fixed dipole emitters. The resulting images are shown in Fig. 2.17. Before imaging the molecules with the vortex phase mask, they are imaged with clear aperture at a defocus value of ~ 1.2 micron from the focal position. As expected, we see the blurred air-disc function. The vortex mask is then inserted in the Fourier plane of the 4f system. The PSF is now the donut shaped intensity distribution that has a null in the center. The vortex mask was then used to image DCDHF-N-6 molecules embedded in PMMA that act as fixed dipole emitters whose emission pattern depend on their orientation as well. As shown in Fig. 2.17, we observe the crescent shaped images of fixed dipoles similar to simulated images shown Fig. 2.14.

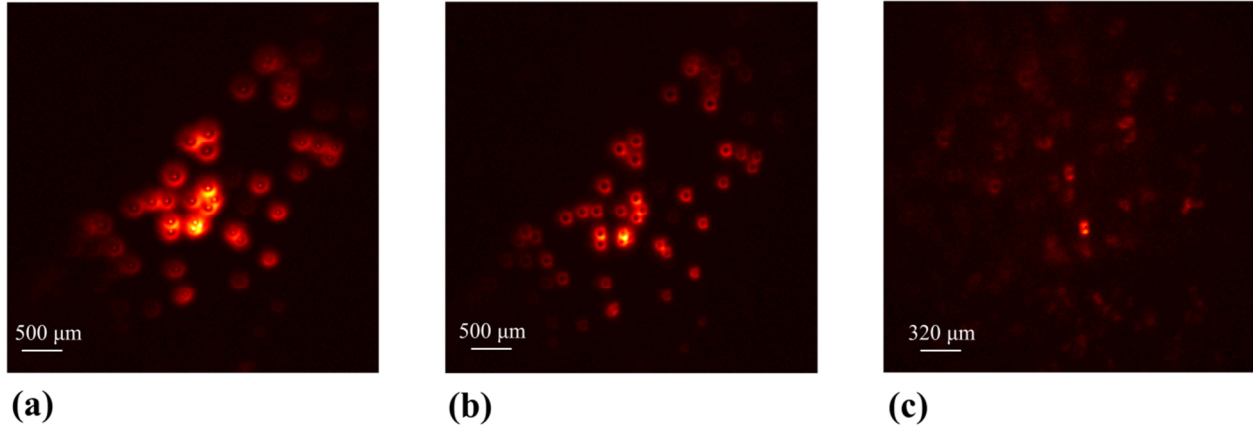


Fig. 2.17 Experimental images using the vortex phase mask: The experimental setup is similar to the one shown in Fig. 2.8(A). The fabricated vortex phase mask DOE was used instead of the SLM. (a) and (b) shows the image of fiduciary beads with a standard clear aperture and a vortex phase mask respectively at a defocus of 1.2 microns. (c) Shows the image of DCDHF-N-6 molecules embedded in PMMA creating fixed dipole emitters.

As shown earlier, the vortex phase mask has a lower $CRLB$ than that of the DHPSF meaning that if we use the best unbiased estimator for the vortex and DHPSF, the estimates obtained using the vortex phase mask will be less prone to estimation errors. However, unlike the DHPSF the vortex does not present us with a straightforward metric like the lobe asymmetry. Hence, other estimation methods like maximum likelihood estimation (MLE), matching pursuit, convex optimization etc. are better candidates for use with the vortex phase mask[70], [98]–[103].

2.6 Conclusion and Outlook

In conclusion, we have investigated the 5D (3D localization + 2D orientation) super-resolution of fixed dipole emitters. In comparison to the 3D localization of point sources, with appropriate optical systems, the 5D estimation shows better estimation precision as long as the systematic errors due to orientation are taken into account.

The *CRLB* analysis provides a powerful tool for the design of fixed dipole localization/orientation imaging systems. The main conclusion from this analysis is that when imaging fixed dipoles under shot noise limited conditions, systems that are sensitive to polarization are stronger candidates for estimating the 3D position and orientation of the dipole. In particular we have shown that the commonly used systems that acquire the total intensity of a defocused single image provide the poorest localization and orientation performance among the systems considered here. Clearly, this is primarily due to the fact that the light emitted from a fixed dipole is polarized. Hence, splitting the emitted radiation in orthogonal polarization states helps estimate these parameters more efficiently by making the system more sensitive to changes in position or orientation.

Furthermore, we quantified the performance limits from a set of candidate imaging systems by comparing their *CRLB*. We also demonstrated the importance of multifocal imaging in terms of the *CRLB* for localization and orientation estimation. The *CRLB* analysis establishes that position estimations can be uniformly improved by using a two channel bi-focal polarization sensitive system, while a single focus plane polarization system might provide a lower *CRLB* for a short range defocus region. On the other hand, the orientation of a dipole is best estimated using a two channel bi-focal linear polarization sensitive system or a polarization-sensitive double-helix or vortex phase mask system. Since the double-lobed shape of the DH-PSF is conserved over various dipole orientations and axial positions, the orientation precision of the DH-PSF is uniform over a large range of defocus. Although, the estimation of 3D location of a point source is dissimilar to the 5D parameter estimation of a dipole source, a *CRLB* comparison of them (Appendix 2A to the chapter) provides insight into the fundamental precision limits of isotropic and anisotropic sources.

With the help of direct experimental demonstration, we also show that the DH-PSF can be used to simultaneously extract precise 3D localization, estimate dipole orientation, and dramatically reduce (x, y) systematic errors due to the orientation effect over an extended z range. With the correction of localization errors from the SM dipole orientation effect, far-field super-resolution microscopy is one step closer toward attaining molecular spatial resolution[104] to reveal the nanoscale machinery at work within living cells.

APPENDIX 2A LOCALIZATION OF ISOTROPIC POINT EMITTER VS. DIPOLE EMITTER

A freely and randomly rotating dipole can be modeled as an isotropic point source emitter. The localization of isotropic emitters constitutes a different problem than that of the localization of fixed dipoles because isotropic emitters lead to a three-parameter estimation problem, while fixed dipoles require the estimation of five parameters. Therefore, because the prior knowledge about the object to be localized is different, special care has to be taken in understanding the limitations of a performance comparison.

Here we compare the *CRLB* of the dipole localization with that of a point source emitter. A point source emits a spherical wave making the intensity equal in all directions, unlike that of a dipole where the intensity varies as $\sin^2\theta$, where θ is the angle measured from the axis of the dipole. We assume that the total number of photons emitted by the point source and the dipole is equal. Thus, for a dipole oriented perpendicular to the optical axis we derive the ratio of the number of photons captured by the lens as

$$\frac{\text{Dipole Photon Count}}{\text{Point source Photon Count}} = 1 + \cos^2 t_m + \cos^2 t_m \quad (2.19)$$

where, t_m is the half-angle of the cone captured by the objective lens. For a system with $NA=1.4$ and index of immersion medium $n=1.52$, $t_m \approx 67^\circ$ and the above ratio ≈ 1.5 . Thus, if the number of detected photons for the fixed dipole oriented perpendicular to the optical axis is 5000, for the isotropic case it will be ≈ 3333 . The *CRLB* is calculated in a similar way using Poisson noise and the lower bound of the volume localization error calculated as in eq. (2.13)

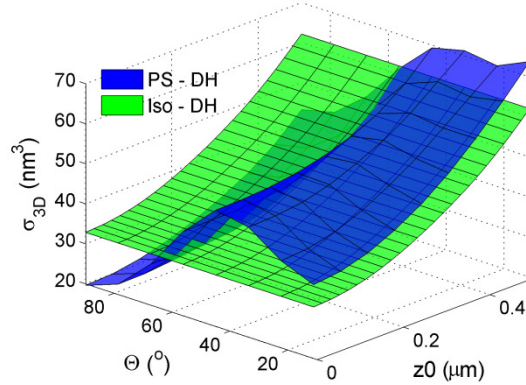


Fig. 2.18 Comparison of *CRLB* for 3D localization for a fixed dipole and an isotropic emitter: The 3D volume localization lower bound- $\sigma_{3D}(4\pi/3 \cdot \sigma_x \cdot \sigma_y \cdot \sigma_z)$ is plotted as a function of the polar angle Θ and defocus distance (z_0). The systems compared in the above plots are the linear polarization with the DH mask (PS-DH: blue surface), and the DH system for the isotropic emitter (Iso-DH: green surface). For this comparison it is assumed that both emitters emit the same number of photons leading to varying number of detected photons.

Fig. 2.18 shows the volume localization error for a fixed dipole compared with that of the isotropic emitter. The localization of the isotropic emitter is clearly independent of the dipole orientation (Θ, Φ). Because we assume the fixed dipole and the isotropic emitter emit the same number of photons, the fixed dipole can be localized more precisely at orientations around the normal to the optical axis, which are the directions of maximum radiation. Similarly, fixed dipoles oriented between 0° and 50° from the optical axis have poorer localization accuracy. The relative difference is explained by the fact that the number of photons detected for the dipole is

larger as long as the dipoles are oriented closer to the transverse plane ($\Theta=90^\circ$), while the difference in image shape has only a second order effect.

Chapter 3 Phase masks as a diffractive optical element (DOE)

3.1 Introduction

In Chapter 2 we established that engineering the Green's tensor by the introduction of phase masks can aid in precisely estimating the dipole orientation and location. In this section we present a method for fabricating these wavefront modulating elements as diffractive optical elements (DOE). The fabrication was done as a part of the NNIN-REU summer program with the assistance of Aubrey Shapero at the Colorado Nanofabrication Laboratory (CNL) at CU-Boulder.

Previously, PSF engineering phase masks were either loaded on SLM[37], [86], [105], [106] (Fig. 2.8) or realized using amplitude holograms[29]. The major drawback of using SLM is that they are polarization sensitive, and hence in general reject about 50% of the incoming light[30], [37], [90] unless the incident light is carefully controlled to modulate and collect all polarization states[86], [89]. However, in single molecule imaging, the number of photons available for precisely estimating the imaging metrics is only on the order of a few thousand. It can be shown that, for photon-limited systems, the localization precision varies as the square of number of photons captured[107]. Hence, there is a need to realize optically efficient phase masks.

An alternative way of implementing phase masks is by using them as diffractive optical elements (DOE) realized as surface relief structures in an optically transparent material. In the paraxial and thin element limit, these phase masks are polarization independent. Another advantage of DOEs is that they can be fabricated using low absorption materials like glass, quartz or polymer. The phase change imparted by the DOE is related to its depth profile and is given by

$$h(x, y) = \frac{\lambda_0}{n(\lambda_0) - 1} \frac{\psi(x, y)}{2\pi} \quad (3.1)$$

Where, λ_0 is the wavelength of operation, $n(\lambda_0)$, is the refractive index of the substrate and $\psi(x, y)$ is the required phase variation. Since phase changes can always be expressed between 0 and 2π , the maximum height profile required to impart any given phase is on the order of $\sim 2\lambda_0$ making it possible to implement DOEs in extremely thin substrates.

Diffractive optical elements have previously been fabricated using a number of techniques that include gray-level lithography[67], [98], [108], multi-step binary exposures[63], Ion beam etching[109], direct diamond turning of a surface[110][111], etc. Direct-write methods such as Ion beam etching and diamond turning are both scanning type methods and require extremely long fabrication times. On the other hand, maskless gray-scale lithography is extremely promising and was previously used to fabricate DHPSFs[67], [98]. The benefit of gray-level lithography is that it allows fabrication of continuous height relief and therefore was thought to be better than conventional binary lithography. However a major limitation of the gray-level method was found to be the inconsistent performance of the lithographic instrumentation and also the lack of optimal photoresists developed for continuous surface reliefs. This resulted in point defects throughout the fabricated phase mask which lead to unwanted scattering of light in experiments. Hence we turn to the multiple binary exposure lithography method to fabricate high efficiency 16-level phase mask.

3.2 Diffraction efficiency of DOE

In the binary multiple exposure method, the lithography process is repeated multiple times to approximate a continuous relief structure by 2^M steps, M being the number of binary amplitude masks used. The multi-step procedure is shown in Fig. 3.1. The transverse resolution that can be achieved using this method is typically on the order of $\sim 1 \mu\text{m}$.

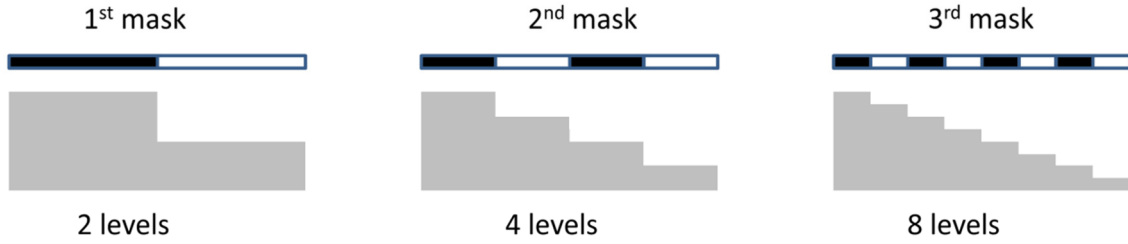


Fig. 3.1 Multiple steps in typical binary multi-exposure lithography. The number of discrete levels is 2^M , where M is the number of binary amplitude masks used.

The quality of the binary DOE depends on the number of discrete steps used to approximate a continuous profile[63]. In general the quality is determined by the percentage of energy transmitted in the first diffraction order and is also termed as its diffraction efficiency. For an N -level phase mask, the diffraction efficiency is given by[112]

$$\eta(N) = \left(\frac{\sin(\pi/N)}{\pi/N} \right)^2 \quad (3.2)$$

The diffraction efficiency for up to 16-levels is shown in Fig. 3.2. The diffraction efficiency for an 8-level phase mask is about 95% and for a 16-level phase mask is around 99%. Since single molecule experiments are extremely demanding in terms of the number of available photons, we fabricate a 16-level mask to maximize the efficiency.

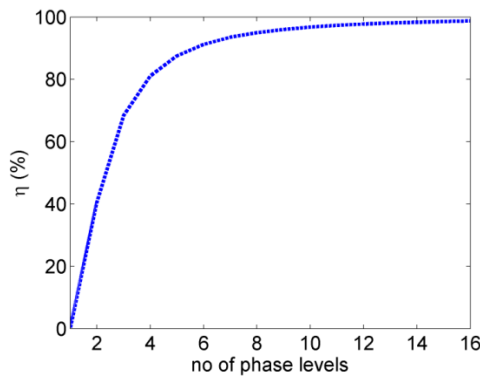


Fig. 3.2 Diffraction efficiency (η) as a function of number of discrete phase levels used to approximate a continuous profile.

3.3 Alignment of binary masks

The 16-level phase mask requires four binary amplitude masks. In each step, the amplitude mask is aligned on top of the intermediate phase mask. Misalignments manifest themselves as errors in the transmitted wavefront. Hence, aligning tolerance of the binary amplitude masks affect quality of the phase mask. The fabrication process involves first converting the gradient pattern into four binary amplitude patterns for lithography[98]. These are made into the binary mask using the Heidelberg DWL 66FS. An image of lithography mask with appropriate marks for alignment is shown in Fig. 3.3. The lithographic mask is designed to accommodate four phase masks on a single 1” x 1” substrate. The purple areas denote the areas that will be etched away after development, thus forming the binary amplitude pattern. It should be noted that the multi-level binary method works well with both positive and negative photo-resists. In a positive photo-resist the exposed area is washed away after development whereas for negative photo-resist, the exposed area remains on the substrate. If a negative photo-resist is desired, the polarity of the designed mask can be changed using the software in Heidelberg DWL 66FS. This will cause the purple areas to become opaque after development and etching.

The central pattern in Fig. 3.3(a) shows the circular binary amplitude that is used to create an aperture in the chrome deposited on the substrate. The circular aperture is used to block any stray light from entering the final phase mask when it is used in the optical setup. It also helps in aligning the center of the phase mask with the optical axis. Also shown in part (a) are the four binary amplitude masks used for the vortex phase mask. In order to minimize propagation errors induce due to misalignment, two sets of markers are used. The crosses shown in (b) are used for coarse alignment whereas the ones shown in (c) are used for finer alignment. The

decreasing size of the crosses can be used to align the binary amplitude masks with micron order precision.

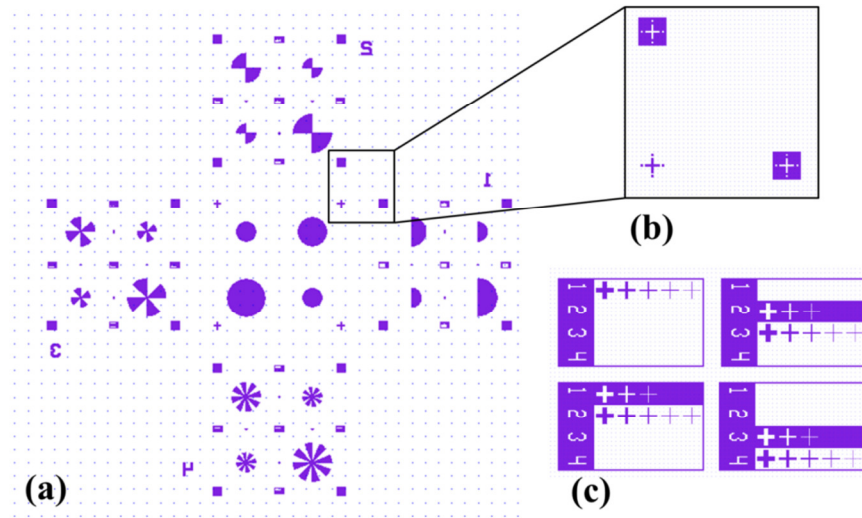


Fig. 3.3 Design of the binary amplitude mask. (a) Design showing the amplitude mask to create and aperture in chromium mask and the four binary amplitude masks required to generate the 16-level phase mask. (b) Coarse alignment markers used to align the phase mask in the center of the aperture. (c) Fine alignment markers used to align the binary amplitude masks on each other.

3.4 Fabrication of the phase mask

The fabrication of the 16-level phase mask requires using a 4 amplitude mask exposures. Moreover, to create a circular aperture, an additional initial exposure is required. Therefore, the first step in the fabrication of the phase mask is depositing chromium on the glass substrate. This is done using the thermal evaporation (deposition) method. In this method, the deposition material is heated in a vacuum chamber ($\sim 5 \times 10^{-6}$ Torr). The heating causes the material to evaporate and condense on the cooler substrate. Vacuum helps in making sure that the evaporated vapors do not collide with any background gas and directly travel to the substrate. Using this procedure a 40nm layer of chromium is deposited on one side of the glass substrate.

Once chromium is deposited, the substrate is subjected to the 5 exposure steps mentioned earlier. Each of the exposures is a 5-step process as illustrated in Fig. 3.4. The first exposure is

carried out on the chromium side of the substrate whereas for subsequent exposures the glass side is used.

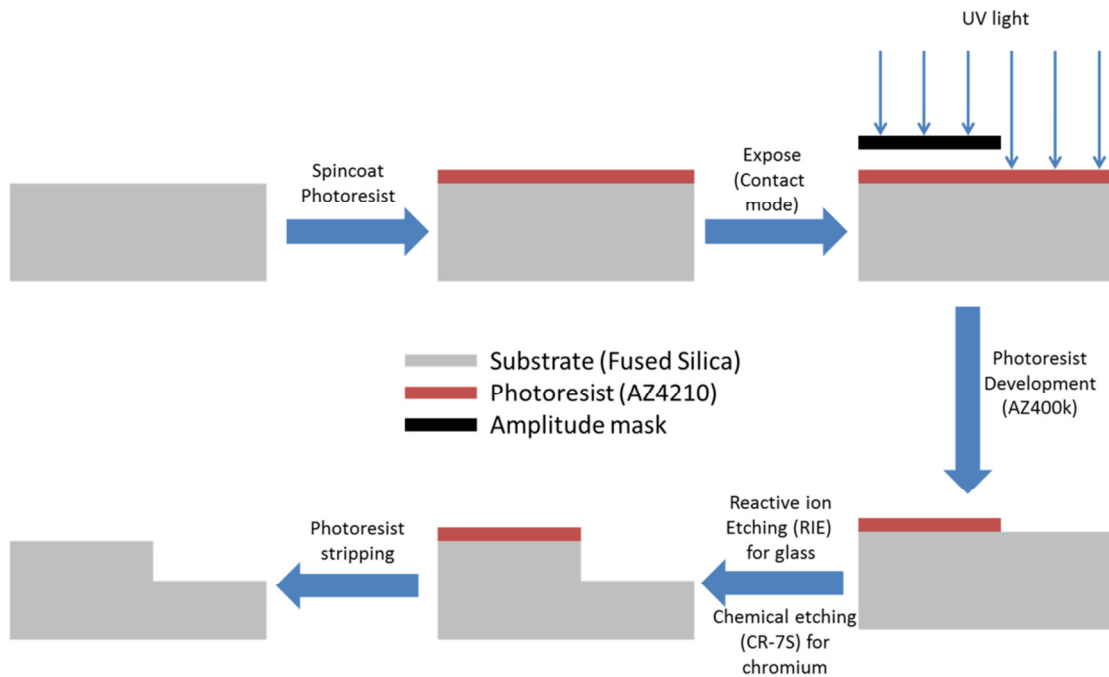


Fig. 3.4 Step-by-step procedure for exposing a single binary amplitude mask: The steps involved in each of the exposure steps is shown. The substrate used here is quartz; photo-resist is the positive Clariant AZ4210. The photo-resist is spin-coated for 30s at 6000 rpm to create a ~1.8 micron thick layer. UV light is exposed onto the photoresist for 12s using a 160W light source. The exposed mask is developed in a 1:4 solution of AZ400K and DI water for 2 minutes. Reactive ion etching used to etch in glass whereas chemical etching using CR-7S is used to etch away chromium to create a circular aperture. The photo-resist is stripped using acetone in the final step.

3.4.1 Spincoat photoresist

The first step to any lithographic process is deposition of an appropriate photo-resist. We choose the positive Clariant AZ4210 photoresist to ensure that minimal amount of material is removed during the development process. It has been shown that positive photo-resists are capable of finer resolution and unlike negative photoresists do not swell during development[113]. The photo-resist is spin-coated for 30s at 6000 rpm. The coating thickness was measured around ~1.8 micron which is adequate for the etching step as explained later. The

adhesion between chromium and AZ4210 is strong whereas between glass and AZ4210 is weak. Therefore, an adhesion layer of hexamethyldisilazane (HMDS) is spincoated on glass before the photoresist. The photoresist is then soft-baked on a hotplate for 90s at 100° C. This procedure is also known as pre-baking owing to the fact that it is baked before the exposure. Pre-baking minimizes the solvent concentration of photoresist which helps in avoiding mask contamination, sticking to the mask, and improves adhesion. Unlike certain other photoresists, AZ4210 does not require a post-exposure bake.

3.4.2 Exposure

The substrate is allowed to cool down for a couple of minutes before exposing it using the SUSS MJB3 mask aligner. The main challenge in this lithography method is the demanding alignment requirements. However, with the help of properly designed alignment markers (Fig. 3.3), the phase masks were shown to be extremely reproducible with minimal errors. The exposure time depends on the photoresist thickness and the intensity of UV light used. It was found that a 12s exposure using a 160W source was appropriate for the 1.8 micron thick photoresist layer. Exposing the photoresist to UV light causes a chemical change in the photoresist making the exposed regions soluble (using appropriate developer) in the case of a positive photoresist.

3.4.3 Photoresist development

Photoresist development refers to the process of washing away the exposed (or unexposed) regions in case positive (or negative) photoresist. In the case of AZ4210, the appropriate developer is the AZ400K. Development exposes the regions of the substrate that need to be etched in the next step. Hence, it is important to make sure that the photoresist has been completely developed by observing the color contrast between the photoresist and the substrate under an optical microscope. The development time typically depends on the

photoresist thickness, developer concentration and the age of the developer. We found that using a 1:4 concentration of AZ400K and de-ionized water, the development time was 2 minutes. The sample is lightly stirred during development for efficient removal of photoresist.

3.4.4 Etching

In this step, the sample is etched either on the glass side or the chromium side depending on the exposure step. For etching in chromium, a chemical etch is used by submerging the sample in CR-7S and lightly stirring it for ~90s. The sample is observed under the microscope to make sure that no chromium residue is left and a clear circular aperture is obtained.

The glass side is etched by reactive ion etching (RIE) using the RIE II Plasmatherm at CNL. RIE is a dry etching process that uses reactive chemical gases that attack the substrate removing material from it. RIE is an anisotropic etching process meaning that the vertical etch rate \gg horizontal etching rate. Hence straight edges can be etched extremely well using RIE. A mixture of 16 SCCM of CHF₄ and 4 SCCM of CF₃ is used for etching in glass. The etch rate was calibrated to be about 13nm/min and typically doesn't vary over periods of months. It is important to calibrate the etch rate of the photoresist as well to make sure the photoresist doesn't get completely etched exposing the substrate. The etching time depends on the required etching depth and the etching rate. In each consecutive exposure the phase mask is etched to a depth given by $h_{2\pi}/2^M$, where M is the mask number and $h_{2\pi}$ corresponds to an etch depth that imparts a phase difference of 2π , i.e. $h_{2\pi} = \lambda_0 / (n(\lambda_0) - 1)$.

3.4.5 Photoresist stripping

Once the etching process is completed, any remaining photoresist on the substrate is dissolved using acetone followed by isopropanol. The substrate is then cleansed using oxygen plasma to remove any residual organic impurities.

The substrate is now ready for the next exposure and the process is repeated for each of the binary amplitude masks. A major drawback of the binary multi-exposure method lies in the fact etching into the substrate is a permanent process and a single over or under etched step can induce significant errors in the sample. Hence, the binary multiple exposure method needs to be carried out diligently. The total time required for fabricating a single phase mask is around 10 hours but multiple substrates can be exposed and etched as long as they have the same wavelength of operation increasing the total throughput.

3.5 Fabricated mask testing

The procedures developed earlier are followed to manufacture the vortex phase mask that works for a wavelength of 633nm. The depth profile of the fabricated mask is measured using a white light interferometer. The resulting profile is shown in Fig. 3.5. Part (a) shows the actual depth profile shown on the profilometer. The refractive index of quartz at 633nm is ~ 1.542 . Therefore the step height for a 16-level phase mask is given by $633\text{e-}9/(0.542*16) = 73\text{nm}$ which as shown in the part (b) is very close to the measured height of 75nm. Using the obtained depth profile, the corresponding phase variation imparted can be calculated by inverting eq. (3.1) and is shown in Fig. 3.5(c).

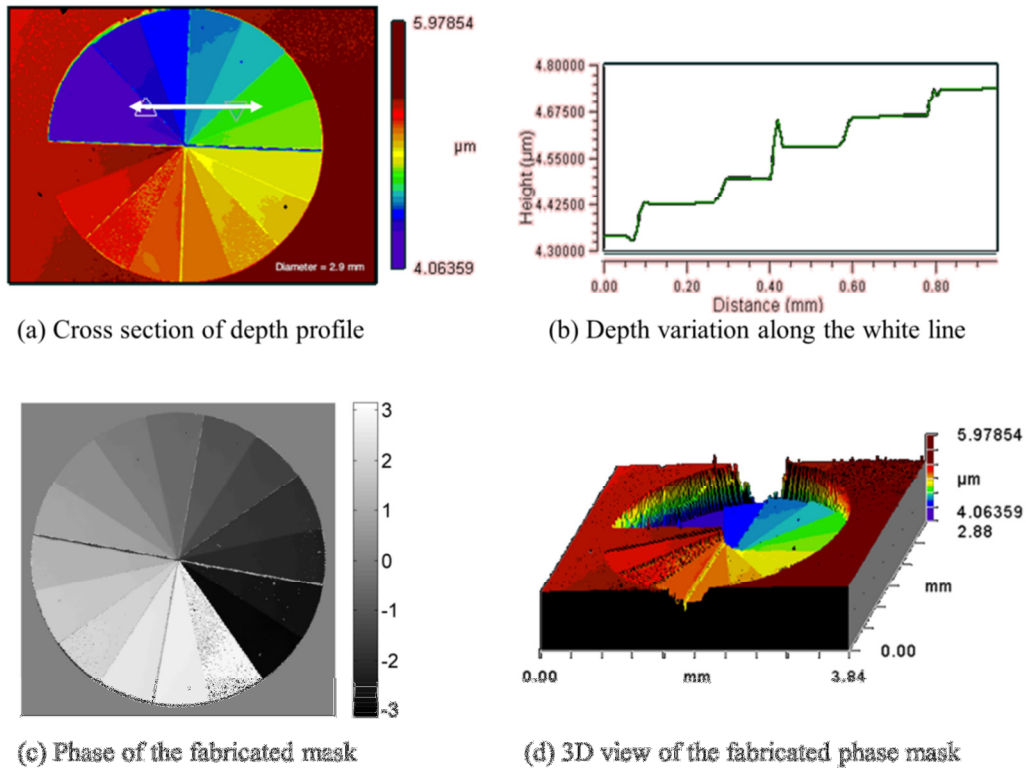


Fig. 3.5 Profilometry measurement of vortex phase mask: A white light interferometer is used to measure the depth profile of the fabricated vortex phase mask. The figure shows (a) 2d cross section of the fabricated mask. (b) The 1d depth variation is shown along the white line in (a). (c) Using the depth profile the relative phase difference is calculated. (d) 3d view of the fabricated phase mask.

The depth profile and the corresponding phase profiles act as test of the fabricated phase mask. Another simple test that measures the quality of the phase mask is the CRLB comparison of the fabricated phase mask compared to the ideal vortex phase mask as shown in Fig. 3.6. The solid angle and volume standard deviations are plotted as a function of polar angle Θ . The red and green curves represent the fabricated and the ideal vortex phase mask respectively. The solid lines represent the single channel total intensity system whereas the dashed lines represent the polarization sensitive two channel system. A strong agreement is seen between the ideal and the fabricated phase mask.

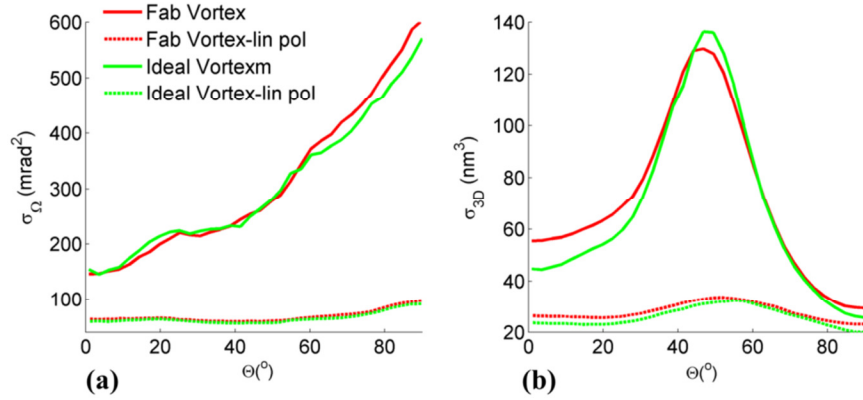


Fig. 3.6 CRLB comparison of the ideal vs. fabricated vortex mask: Lower bounds of the (a) volume standard deviation and (b) solid angle standard deviation for the ideal vortex phase mask (green) and the fabricated vortex mask (red) is shown for the single channel total intensity system (solid) and the linear polarization system (dashed).

3.6 Conclusion

Fabrication of optically efficient phase masks using the binary multi-level exposure method is demonstrated. The diffraction efficiency is maximized by using 16 phase levels to approximate a continuous phase profile. The depth profile of the fabricated phase masks showed strong agreement with the ideal designs. The transmittivity of these phase masks were calculated to be about ~90%.

Chapter 4 Negative Permeability with Arrays of Aperiodic Silver Nanoclusters

4.1 Introduction

In the previous chapter we showed the importance of using electromagnetic optics for computational imaging when the source emission is anisotropic in nature. In this and the following chapter we present an analysis of another degree of freedom of optical imaging systems; i.e. the material used to make optical lenses. The analysis is in regards to materials that are not typically available in nature and are termed as metamaterials.

Metamaterials are artificially structured materials whose properties can be engineered by altering the shape, size and composition of the structural units composing it. In the long wavelength limit; where the wavelength of light is much greater than the periodicity of these units; metamaterials can be assigned macroscopic optical properties. Such materials, if properly designed, can exhibit non-conventional properties, like negative refractive index[49], [114] and ultra-low refractive index[50], [51]. This could lead to applications such as imaging with subwavelength resolution using a flat lens[114], optical nanocircuits[52], and cloaking[53]–[57]. Lately, quasiperiodic and disordered structures have become attractive because they provide additional flexibility in the design of optical material properties[115]–[119].

4.2 Requirements for negative refractive index

The refractive index of a material depends on two material constants, dielectric permittivity $\epsilon = \epsilon' + i\epsilon''$ and magnetic permeability $\mu = \mu' + i\mu''$ and is defined by $n = \sqrt{\mu\epsilon}$. The sufficient condition for obtaining negative refractive index is given by $\epsilon'\mu' + \mu''\epsilon' < 0$ [120], [121] and can be satisfied even if only either the effective permittivity or

effective permeability is negative. However, it can be shown that the figure of merit (FOM) defined as $FOM = |n'|/n''$ which is a performance index for negative index materials, is generally greater for materials having both negative permittivity and permeability and thus are generally better candidates for obtaining negative refractive index.

One of the first solutions to achieve negative μ' was by using a split ring resonator structure[122]. However, operation at optical frequencies requires SRR in the nanometer scale, making the fabrication extremely challenging. Instead an architecture consisting of a periodic array of pairs of thin parallel silver strips has been implemented[123], [124]. Another metamaterial architecture that utilizes the magnetic dipole-like Mie resonance of a cylindrical structure has been proposed recently[125]–[128]. The magnetic response in this architecture is attained by using a TE wave (H field parallel to the axis of the wires) incident upon periodically arranged clusters of silver nanowires, where the wires within the clusters are also placed in a periodic fashion. This architecture is particularly interesting owing to the tunability of the resonance parameters attained by changing the metal filling fraction.

However, all the magnetic resonance structures that have been proposed to date are based on periodic unit cells. Interestingly, owing to the nature of the effective medium approach, the inclusions in a metamaterial structure do not need to be periodic. Here, we show that a (periodic) array of *aperiodic* clusters of silver nanowires can give rise to negative effective permeability in the optical regime. More importantly, we show by a design example that a unit cell composed of aperiodic inclusions can give rise to stronger resonance peaks than their periodic counterparts.

4.3 Design of the aperiodic metamaterial

The basic design of the aperiodic metamaterial was based on the periodic cluster designs proposed in [125], [129]. In order to tune the resonance frequency in the optical region, the nano-

wires chosen were composed of silver, with a radius of $r=5\text{nm}$ and the mean center-to-center spacing as 12nm . In this regime, there is significant field penetration into the metal nanowire and the metal wires support an electric-dipole-like Mie resonance whose resonance frequency falls in the optical frequency region. The Drude model was used for the permittivity of silver, with a plasma frequency $\omega_p/2\pi = 2.18 \times 10^{15}$ Hz and the damping coefficient $\gamma/2\pi = 4.35 \times 10^{12}$ Hz.

4.3.1 Algorithm used to generate the aperiodic island

In order to generate the aperiodic island, we used a normal distribution of nanowires, where the mean of the distribution was 20% (2nm) of the wire diameter and the variance 5% (0.5nm). We start with a wire centered at (0,0) and use the normal distribution condition to find the radial position, and a uniform distribution to find the angle of the next wire relative to current one. The same procedure is followed by randomly selecting a wire from the existing ones. To make sure that no two wires overlap, the distance of every new wire from all other existing wires is verified to be greater than 10nm. Using this algorithm a distribution of over 100 nanowires was generated and all nano-wires in a square region of $55 \times 55 \text{ nm}^2$ around the center were used for the aperiodic island. Different realizations of the aperiodic unit cell were constructed and a particular realization that yielded a strong magnetic resonance was chosen. The top performing aperiodic cluster we consider here consists of 19 silver nanowires whose co-ordinates are given in the Table 4.1.

No.	x (nm)	y (nm)		No.	x (nm)	y (nm)		No.	x (nm)	y (nm)
1	0	0		8	15.88	-13.24		15	-10.3	17.36
2	4.38	-10.17		9	16.68	17.66		16	-0.67	23.72
3	12.05	-2.3		10	22.16	-23.8		17	-15.09	-24.66
4	-7.48	-8.21		11	-15.03	-0.1		18	-20.9	14.36
5	10.07	8.64		12	24.7	-5.9		19	-17.85	-14.6
6	20.69	5.73		13	-5.38	-19.14				
7	7.83	-20.71		14	-0.23	12.8				

Table 4.1 Cartesian co-ordinates (x , y) in nm for the center of each of the 19 nanowires used to generate the aperiodic island

In order to simulate the complete metamaterial structure, periodic boundary conditions were applied to this unit cell of the aperiodic cluster. For a fair comparison, the periodic cluster was then chosen to closely match the aperiodic structure in terms of its spacing and number of wires. The resulting metamaterial structures for the aperiodic and periodic cases are shown in Fig. 4.1(a) and (b) respectively. The aperiodic cluster consists of a cluster of silver nanowires randomly arranged, while these clusters themselves are arranged in a periodic fashion with a period, a , of 70nm. The periodic unit cell consists of 20 silver nanowires arranged in an array of 4x5 matrix. The nanowires are placed 11 nm apart and the clusters have the same periodicity of 70 nm.

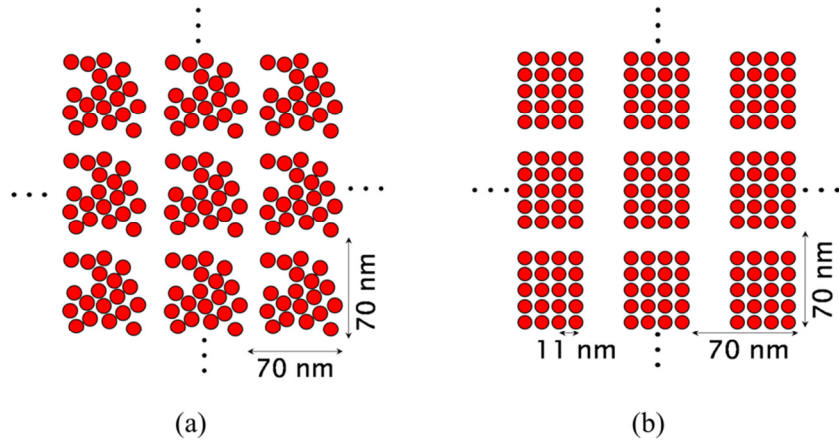


Fig. 4.1 Metamaterial structures for magnetic resonance: The structures compared are (a) Aperiodic unit cell (b) Periodic unit cell. The nanowires have a diameter of 10nm and are composed of silver. The islands in both cases are arranged periodically with a period of 70nm.

4.4 Effective parameter calculation

The effective permeability and permittivity were retrieved using the reflection and transmission coefficients from the far field[130]. With this method we retrieved all four parameters required for an unambiguous and consistent effective medium characterization, namely the real and imaginary parts of the impedance and refractive index. In order to retrieve the effective parameters for a given structure, we first calculate the steady state field distribution using a finite element solver[131] and then calculate the reflection and transmission coefficients in the far field (at distance 900nm for a resonance wavelength λ_{res} of 350nm). Fig. 4.2(a) shows the simulation conditions that were used to compute the steady state field distribution of the metamaterial unit cell. Perfect Electric conductor (PEC) and Periodic boundary conditions (PBC) were respectively used to simulate free space and infinite periodicity in the vertical direction. Low reflection boundary conditions are used on the left and right surfaces of the simulation area to avoid unwanted reflections from the virtual edges. Here, (Rf) and (Tr) represent the planes where the reflection and transmission parameters are evaluated

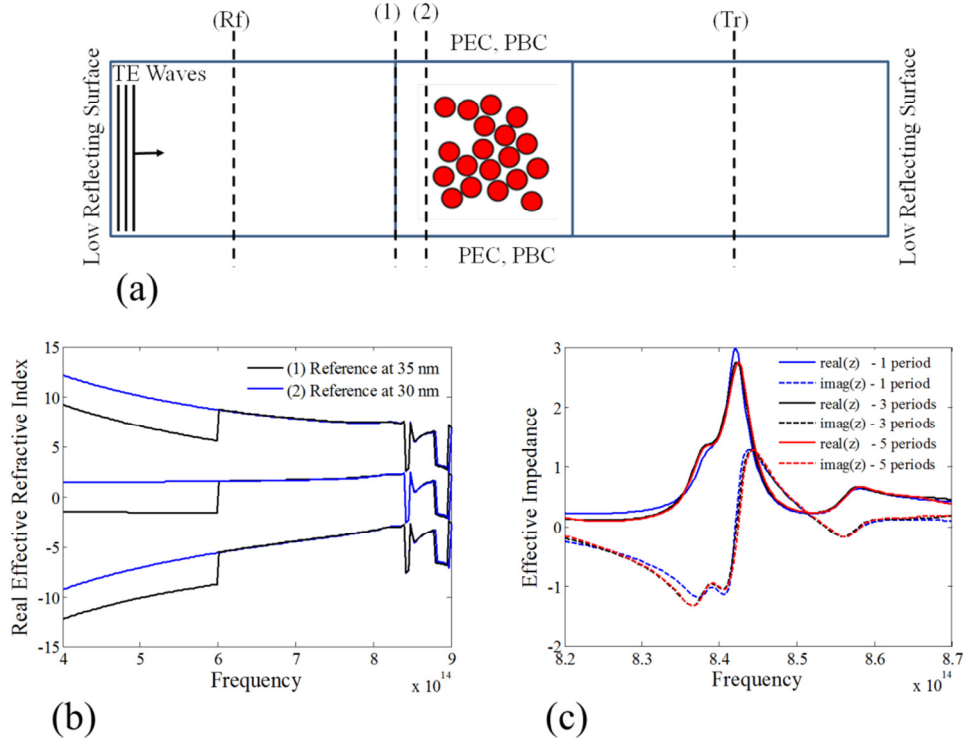


Fig. 4.2 (a) Simulation conditions for the FEM. Perfect Electric Conductor (PEC) and Periodic Boundary Conditions (PBC) are applied to the top and bottom surfaces of the unit cell. (Rf) and (Tr) are the planes in the far field (900nm for a $\lambda_{\text{resonance}}$ of 350nm) where the reflection and transmission coefficients are respectively evaluated. (1) and (2) are two different reference planes used to determine the reflection coefficient and hence the effective refractive index. (b) Real part of the effective refractive index over a broad frequency range for reference plane at distance 35nm (black) and 30nm (blue) from the center of the unit cell for the aperiodic structure (c) Effective impedance for the corresponding aperiodic structure where the number of periods in the propagation direction are 1 (blue), 3 (black) and 5 (red)

Once we calculate the reflection and transmission coefficients, they can be inverted to find the effective index and effective impedance of the structure[130]. Retrieving the impedance and imaginary part of the effective index is trivial, but the real part of the effective index has multiple branches due to the arccosine function. Another complication with retrieving the effective parameters of metamaterials is that they do not have well defined surfaces and thus the reference plane used to calculate the effective parameters is arbitrary. We overcome this obstacle in the following way.

As shown in Fig. 4.2(a), (1) and (2) are two different reference planes used to evaluate the reflection coefficient and hence the effective refractive index. The real part of the effective index is then plotted over a broad frequency range (Fig. 4.2(b)). The resonance occurs around 8.5×10^{14} Hz; thus the effective index curve should be nearly constant and free of any discontinuities for much lower frequencies. Even if the discontinuities do occur, they should be removable by replacing that portion of the curve with a different branch of n (again due to the arccosine function). If this is not the case, we displace the reference plane till we encounter such a situation. In Fig. 4.2(b) it can be seen that a reference plane of 30nm from the center of the unit cell leads to irremovable discontinuities whereas a reference plane of 35nm presents us with a continuous and flat curve. The validity of the reference plane is now verified by applying it to multiple cell simulations and by comparing it to the rigorous band structure. Also as shown in Fig. 4.2(c) the complex impedance for multiple cells (1, 3 and 5) shows a strong agreement with each other.

4.4.1 Anisotropy of the aperiodic structure

The aperiodic unit cell is asymmetric and hence we expect the effective parameters to be anisotropic. Unlike a photonic crystal these properties should also be independent of the periodicity of the unit cell. Accordingly, Fig. 4.3 shows the real part of the effective permeability for a range of incidence angles for a single unit of the aperiodic structure (no periodic boundary conditions). Part (a) shows the effective permeability for angles ranging from 10° to 40° . It can be seen that the magnetic resonance is retained for these incident angles. The lowest effective permeability was observed for normal incidence at 8.47×10^{14} . Part (b) plots the value of the effective permeability for a range of incidence angles at 8.47×10^{14} Hz. It can be seen that the characteristic magnetic resonance is retained for different incident angles but there is a slight

shift in the resonance frequency. Thus at steeper incident angles, the effective permeability becomes non-negative.

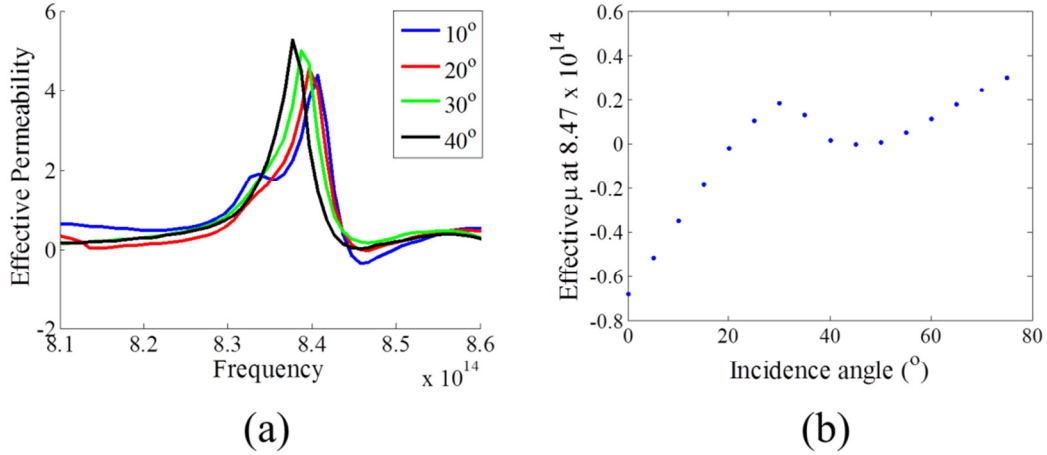


Fig. 4.3 Comparison of the effective permeability of the aperiodic structure for a range of incident angles: (a) Effective permeability as a function of frequency for incidence angles ranging from 10° to 40° in 10° intervals. The resonance feature is retained. (b) Effective permeability at 8.47×10^{14} Hz for incidence angles ranging from 0° to 75° in 5° intervals. The chosen frequency is the one at which the effective permeability is the strongest negative for normal incidence.

4.4.2 Validation of effective medium approach

To validate the effective medium approach and the calculation via reflection/transmission coefficients, the band structure was calculated using two different methods for the aperiodic realization in Fig. 4.1(a). The first approach was based on the rigorous computation of Bloch modes using a finite element method. The second approach used the effective refractive index n , calculated from reflection and transmission parameters to determine the band structure from the relation $ka = 2\pi a \lambda n / c$, where c is the speed of light. As shown in Fig. 4.4(a), the two band structures are in good agreement. This is consistent with previous reports that showed that the effective medium theory has a wide range of validity even near the photonic band gap[128].

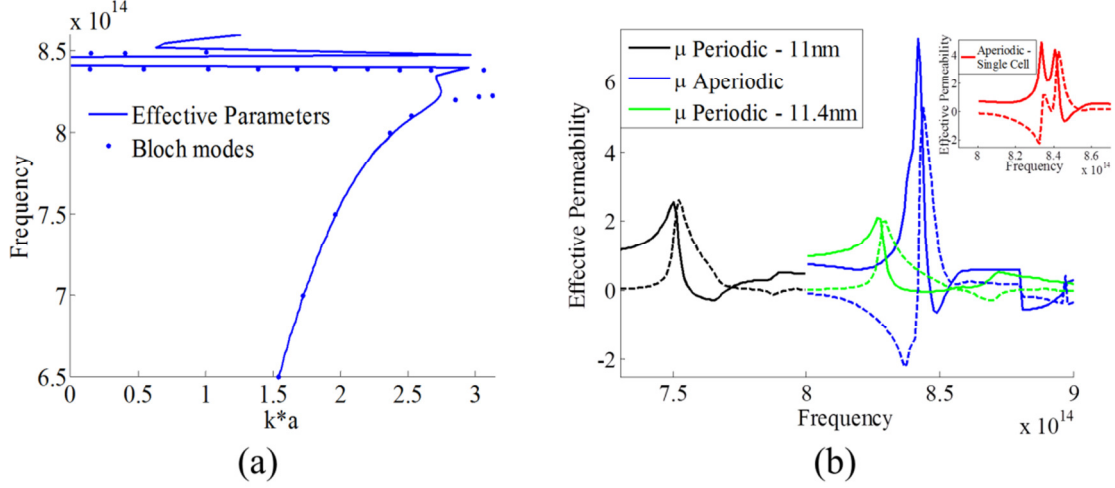


Fig. 4.4 Validation of effective medium approach and comparison of effective permeabilities: (a) Photonic band structure of the aperiodic configuration using effective parameters (blue line) and using rigorous photonic band structure calculation (blue dots). (b) Comparison of effective permeability for the aperiodic structure (blue) and for a periodic structure with wire spacing 11nm (black) and 11.4 nm (green). The inset shows the effective permeability for a single unit cell of the aperiodic structure. Solid(-) and dashed(--) lines represent the real and imaginary parts of the effective permeability respectively.

4.5 Performance comparison of periodic and aperiodic structures

The chosen aperiodic unit-cell metamaterial realization shows a magnetic resonance at 8.49×10^{14} Hz, with $\mu' = -0.65$ and $\mu'' = 1.63$, $\mu' = -4.2$ as shown in Fig. 4.4(b) (blue curve). It can be seen that in certain frequency regions the imaginary component of effective permeability (μ'') becomes negative. But since $n = \sqrt{\mu\epsilon}$, negative μ'' does not represent gain and it can be shown that the imaginary effective index (n'') is still positive. In order to distinguish from the photonic crystal effect and validate the use of effective medium theory, we performed simulations of the aperiodic unit cell without applying periodic boundary conditions. Unlike a photonic crystal, the metamaterial response should be primarily local and the unit cell of a metamaterial should retain the characteristics of the bulk structure. As shown in the inset of Fig. 4.4(b) (red curve) the isolated aperiodic unit cell has a resonance peak of $\mu' = -0.68$ at $8.47 \times$

10^{14} Hz. It is noteworthy that the peak of negative μ' lies above the band gap region. A comparison between periodic and aperiodic systems was made by computing the effective parameters for the aforementioned structures. A negative peak $\mu'_{\text{Per}} = -0.28$ ($\mu''_{\text{Per}} = 0.56$) was observed for the periodic case (black curve) as compared to the $\mu' = -0.65$ for the aperiodic one. We also see that the resonance frequency for the periodic nanocluster has blue shifted to a value of 7.65×10^{14} Hz. To confirm that the aperiodic realization gives a stronger resonance, we match the resonance frequencies of the two structures by changing the wire spacing of the periodic structure to 11.4nm, preserving all the other parameters. As shown in Fig. 4.4(b) (green curve), the modified periodic structure shows a magnetic resonance at 8.45×10^{14} Hz. The negative peak in this case is $\mu' = -0.034$ ($\mu'' = 0.43$), thus confirming that the aperiodic structure shows a stronger resonance than the periodic one. Owing to the varying distances between the inclusions, the aperiodic and periodic structure exhibit weak multiple resonances. This effect can be seen in Fig. 4.4(b) where green (periodic) and blue (aperiodic) curves exhibit weak resonances at higher frequencies.

4.6 Perturbation analysis

Minor changes in the positioning of the nanowires change the strength of the resonance and can critically affect the strength of the magnetic resonance. Hence, the sensitivity of the magnetic properties to nanowire position was analyzed for the periodic and aperiodic structures. The peak effective permeability was calculated for five different perturbation cases. Each nanowire was displaced radially by a distance chosen from a uniform distribution between 0 and P with $P \in \{0.1, 0.2, \dots, 0.5\text{nm}\}$. The direction of the perturbation was chosen using a uniform distribution between $0-2\pi$. Each new realization was verified to make sure that none of the

nanowires overlap and the effective permeability of the resulting structure was computed. The (negative) effective permeability peak was extracted for each of the perturbation distances using 20 realizations for the periodic case and 30 realizations for the aperiodic case. Whenever the resonance frequency coincided with the band gap for the perturbed aperiodic case, the information about the frequency and resonance strength could not be extracted, and such cases were neglected. The results for the periodic and aperiodic structures are plotted in Fig. 4.5(a) and (b) respectively.

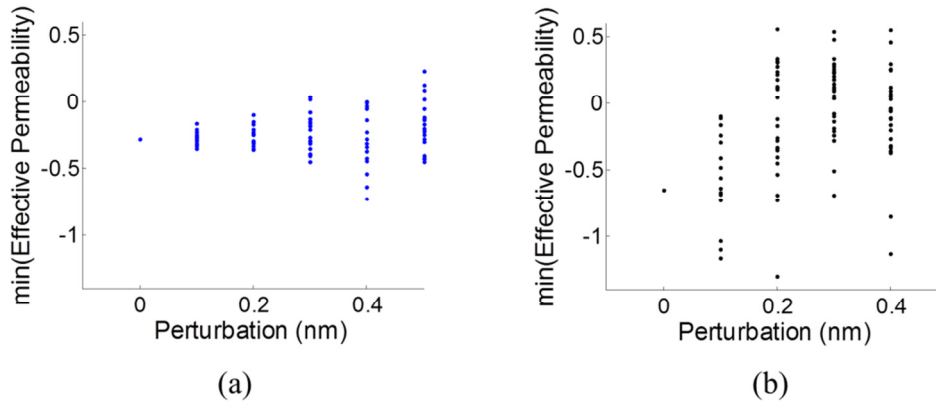


Fig. 4.5 Sensitivity analysis: The plots show the effective permeability at the resonance frequency after perturbation of (a) the structure with the aperiodic unit cell, and (b) the structure with the periodic unit cell (wire spacing is 11 nm).

The average μ' for the aperiodic case is $\langle \mu' \rangle_{\text{Aper}} = -0.005$, whereas the average μ' for the periodic case is $\langle \mu' \rangle_{\text{Per}} = -0.239$. The standard deviations for the aperiodic and periodic case are $\sigma_{\text{Aper}} = 0.34$ and $\sigma_{\text{Per}} = 0.15$ respectively. This shows that the aperiodic metamaterial structure is more sensitive to perturbations than the periodic counterpart.

4.7 Steady state field distributions

The magnetic resonance behavior can also be seen by plotting the steady state field distributions for these structures along with the electric field vector with components (E_x, E_y) . Fig. 4.6(a) and (d) show these plots for the periodic and the aperiodic case, with color representing the relative strength of the magnetic field. The electric field vector loops around the structure in the unit cell and the magnetic field is concentrated within the structure. It can be seen that albeit over a smaller area, the flux of the magnetic field is greater for the aperiodic structure as compared to the periodic one and hence it yields a stronger magnetic resonance. The magnetic field distribution and the electric field vectors for perturbed structures are also shown in Fig. 4.6. The perturbed structures (periodic and aperiodic) that have the strongest magnetic resonance are shown in Fig. 4.6 (b) and (e) whereas (c) and (f) show the perturbed structures with the weakest resonance. These results confirm that the strength of the resonance depends on the flux of the magnetic field within the structure. For the aperiodic case this flux is very sensitive to the relative positioning of the nanowires. However, from Fig. 4.6 it is clear that the perturbed aperiodic structure can yield a resonance strength of up to $\mu' = -1.3$ whereas the periodic metamaterial resonance strength can provide $\mu' = -0.73$.

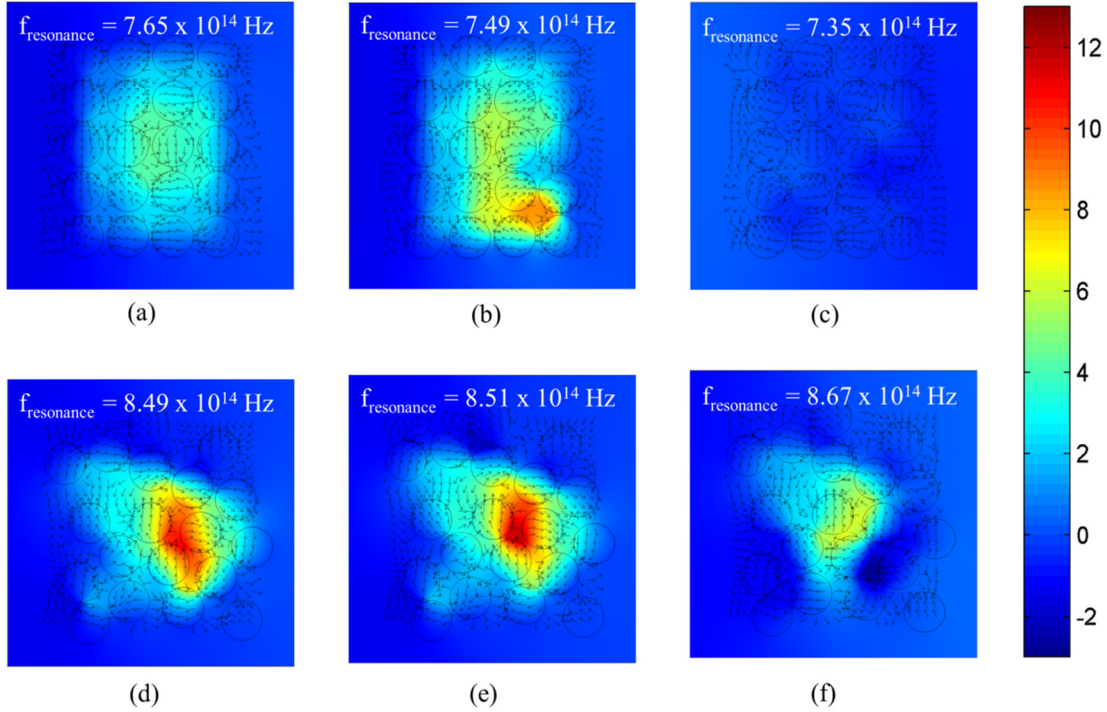


Fig. 4.6 Magnetic field distributions and electric field vector plots for the aperiodic and periodic structures at their respective resonance frequencies ($f_{\text{resonance}}$). The color map represents the relative strength of the magnetic fields. (a), (b) and (c) represent the original, best case (perturbed structure that yields lowest μ'), and worst case (perturbed structure that yields highest μ') designs for the periodic structure whereas (d), (e) and (f) represent the corresponding designs for the aperiodic structure.

4.8 Conclusion

These results suggest that with proper design, aperiodic structures can yield strong magnetic resonance but proper care has to be taken with respect to fabrication tolerances. Furthermore, the fact that the effective medium matches the rigorous calculations suggests that any or all of the unit cells can be replaced by different aperiodic arrangements of nanowires with the same effective medium properties. As a consequence, aperiodic arrays of nanowires where each unit cell is different from the others could be created while still maintaining the same photonic band structure and effective negative permeability.

In conclusion, we have shown that optical metamaterial structures with aperiodic inclusions are strong contenders for negative permeability, and hence negative refractive index. By tailoring the aperiodicity of each cell they have the potential to generate stronger magnetic resonances than periodic structures.

Chapter 5 Infinitely-Refractive Linear material (IRAM): a new optical design paradigm for non-paraxial imaging

5.1 Introduction

In this chapter, we present a new paradigm for optical design based on artificial materials determined by design. During the last years there have been multiple attempts at incorporating metamaterials to improve lens performance, mostly directed at the capture of near field information[23]–[26], [48], [132]–[136]. In far-field imaging it is noteworthy the work by Smith’s group showing the advantages of negative index metamaterial lenses to reduce aberrations[136]. Recent work has also shown that placing a two dimensional thin metallic grating at the interface between two media can help control the direction of rays beyond Snell’s law of refraction[137], an idea that can be applied in lens design[21]. However, even if appealing, these techniques are based on the use of negative refractive index and metal structures, which as shown in the previous chapter, are inherently lossy in the optical regime, and hence limit their applicability.

Here we propose *infinitely refractive-linear artificial materials* (IRAM) to enable three-dimensional or high NA optical elements to maintain a linear relationship between input and output angles of refraction over a large field of view. Because the material properties are dependent on the input angle, IRAMs are intrinsically anisotropic and the wavefront and energy propagation directions are different. Thus, polarization characteristics of light play an important part in the design of IRAM. In section 5.2, we briefly describe the assumptions in Gaussian optics and, using simulations in Zemax, show the effect of increasing incidence angles on the size of the PSF for a singlet lens. In section 5.3, we describe the properties of two different kinds

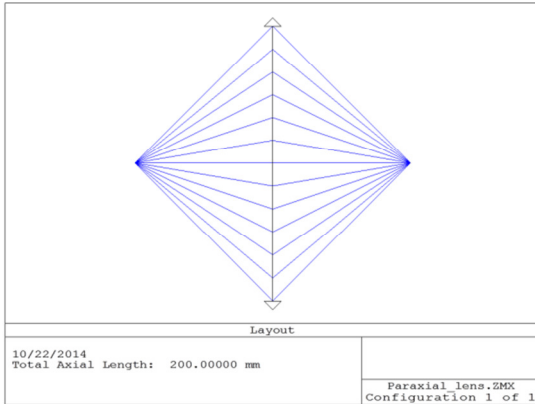
of IRAM that we respectively call phase linear-refraction materials (PLRM) and linear Poynting materials (LPM). We then show that uniaxial materials with appropriate refractive index and birefringence approximate the linearity property of IRAM for incident angles up to 70° as opposed to 30° for isotropic materials using flat-interfaces (Non-planar shaped IRAMs are discussed in Appendix 5B to the chapter). Form birefringence is proposed as a means to achieve arbitrary birefringence within the limits of naturally available refractive indices. Uniaxial materials are then simulated using Zemax in conditions similar to the isotropic singlet and we show that a spot size improvement of over 200% is achieved with singlet lens for on-axis imaging. Lastly, an example of a real-life application of IRAM is demonstrated.

5.2 Gaussian Approximation

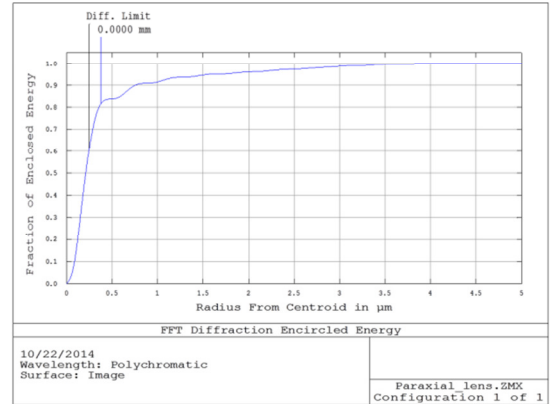
The major assumption in Gaussian optics is that the angle of incidence of the rays on the lens surface is small so that the sine of the angle can be approximated by the angle itself. Thus if a ray is incident from air, Snell's law at the lens surface can be written as $\theta_1 = n \cdot \theta_2$, where θ_1 and θ_2 are respectively the angles of incidence and refraction. This linear relation between the incident and refracted angle turns to simplify all the development of Gaussian optics leading to seemingly perfect imaging without aberrations and is only limited by diffraction. However, this approximation is only valid for incidence angles up to about 30° (using ~5% deviation) for most practical purposes and the Gaussian approximation fails for large incidence angles. In order to exemplify this point further we use an optical ray tracing tool to show the effect of increasing the incidence angle on the PSF. Zemax is a commercially available ray tracing software that can be used for the design and analysis of optical imaging systems. Although ray tracing is valid in the geometrical optics limit, Zemax has some modules that can be used to study the effects of diffraction.

We demonstrate these modules by first modeling an ideal paraxial thin lens as shown in Fig. 5.1. The table, also known as the lens prescription, shows the object and image distances, stops, curvatures and, the lens material. In this example, we choose a lens with focal length of 50 mm and object and image distances at 100mm ($2f$). The resulting layout is shown in Fig. 5.1(a). The diffraction encircled energy plot in Fig. 5.1(b) shows the fraction of energy enclosed as a function of distance from the image centroid. Also shown is the encircled energy of the diffraction limited spot. In an ideal lens the two curves show 100% overlap. The spot diagram, shown in Fig. 5.1(c), is a graph showing where the rays from a point object hit the image surface. An aberration free lens would show a single image point within the numerical limit. Also outlined by the black circle is the relative size of the airy disc. Well-designed systems will have rms spot sizes close to the diffraction limited spot size whereas systems that are dominated by aberrations will have much larger rms spot sizes. The rms spot size of the ideal lens is on the order of 10^{-14} showing that the performance of this lens is limited by diffraction. The cross section of the actual PSF is shown in Fig. 5.1(d).

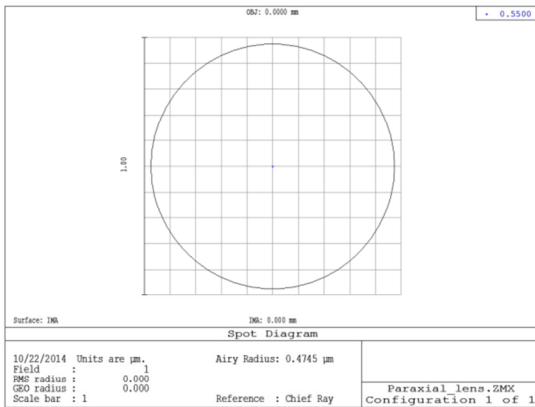
Surf.Type	Comment	Radius	Thickness	Glass	Semi-Diameter	Conic	Par 0 (unused)	Focal Length	OPD Mode
OBJ	Standard	Infinity	100.000		0.000	0.000			
STO	Paraxial	100.000 M			100.000 U			50.000	1
IMA	Standard	Infinity	-		1.421E-014	0.000			



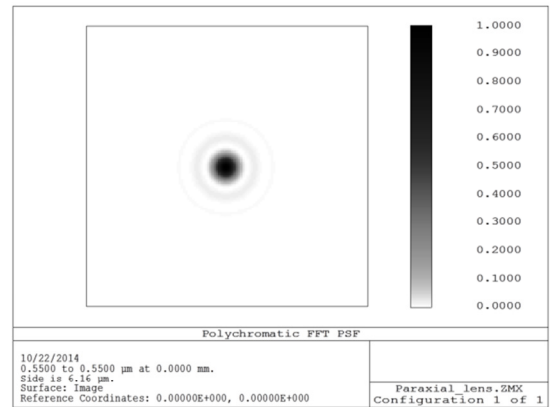
(a) System Layout



(b) Diffraction encircled energy



(c) Spot Diagram with Airy disc



(d) PSF cross-section

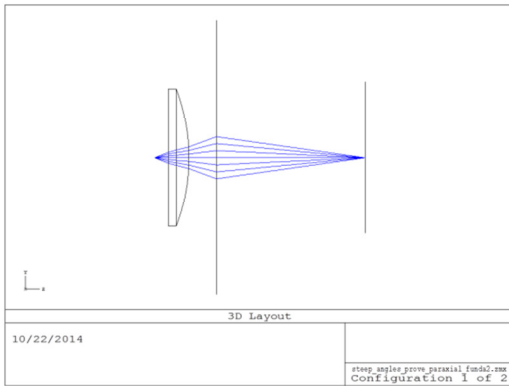
Fig. 5.1 Zemax simulation of a perfect paraxial lens: The lens focal length was chosen to be 50mm. (a) The object and image are $2f$ away from the lens. (b) The diffraction encircled energy shows that all the power is within the diffraction limited spot size. (c) Airy disc is shown in black and the system is not limited by aberrations (d) Cross-section of the diffraction limited PSF.

In what follows, we analyze the performance of a real lens that is susceptible to aberrations. As shown in the lens prescription (Fig. 5.2), the first surface of the lens is chosen to be flat ($R_1 = \infty$) so the incident angles do not depend on the lens curvature. The stop is placed right at the surface. Also, instead of the standard surfaces, birefringent in and birefringent out surfaces were chosen. The reason for choosing birefringent surfaces will be apparent later but Zemax is capable of accurately tracing the ray through birefringent surfaces. The c -axis defined

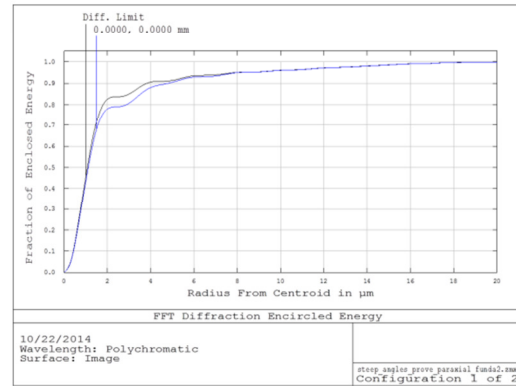
by the X-,Y-,Z-cosine lies along the optical axis and Mode defines whether the ordinary (Mode 0) or the extra-ordinary (Mode 1) ray is being traced. The material used here was added to the Zemax catalog and has ordinary and extraordinary refractive indices of 1.5 and 1.2. However, for the o-ray the index would be a constant 1.5 simulating a generic lens. In order to show the effect of shallow and steep angles on the PSF, the object was placed very close (10 mm) to the first surface. However, this causes the rays to diverge making it harder to study the spot size and the encircled energy. This was overcome by adding the ideal paraxial lens that brings the rays back into focus. Since the ideal lens does not introduce any artifacts, the performance of the system only depends on the real lens.

The surface stop was chosen at 4 mm making the highest incident angle at $\tan^{-1}(4/10) \approx 22^\circ$ which should be close to the paraxial regime. The thickness of the lens was chosen to be 15 mm (small compared to the two surface radii) to emulate a thin lens. The second surface of the lens and the image distance were used as optimization variables to reduce wavefront errors and obtain a strongly focused image. The resulting system layout is shown in Fig. 5.2(a). As seen in the encircled energy plot (Fig. 5.2(b)) and the spot diagram, most of the energy is contained in the diffraction limited spot. The rms spot size is $1.8 \mu\text{m}$ whereas the radius of the airy disc, which depends on the size of the aperture, is about $2.4 \mu\text{m}$. Thus, this exemplifies the well-known fact[60], [138] that for small incident angles, real lenses are limited by diffraction rather than aberrations.

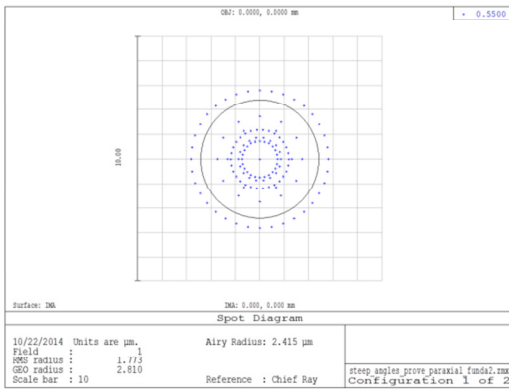
Surf>Type	Comment	Radius	Thickness	Glass	Semi-Diameter	Conic	Draw Axis?	Mode	X-cosine	Y-cosine	Z-cosine
OBJ	Standard	Infinity	10.000		0.000	0.000					
STD	Standard	Infinity	0.000		4.000	0.000					
2*	Birefring..	Infinity	15.000	NO1.5NE1.2	50.000	0.000	0.000	0	0.000	0.000	1.000
3*	Birefring..	-139.660	20.000		50.000	0.000					
4	Paraxial		108.035		100.000			30.000	1		
IMA	Standard	Infinity	-		55.000	0.000					



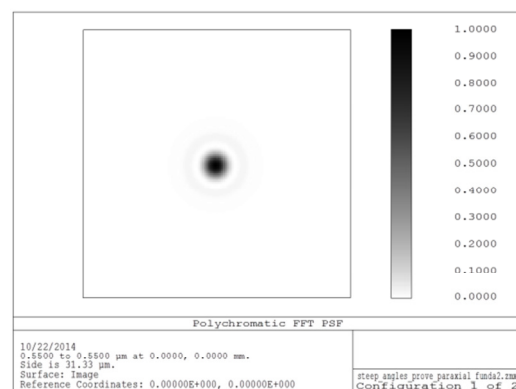
(a) System Layout



(b) Diffraction encircled energy



(c) Spot Diagram with Airy disc



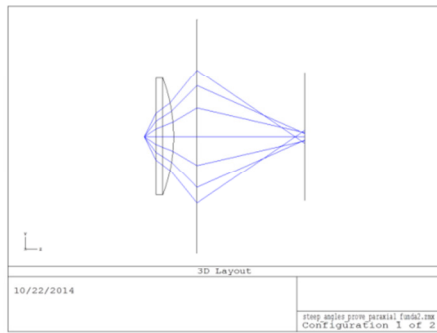
(d) PSF cross-section

Fig. 5.2 Isotropic thin lens in the paraxial regime: The maximum angle of incidence is given by $\tan^{-1}(4/10) \approx 22^\circ$. (b) Most of the energy is contained in the diffraction limited spot which is also seen in (c). The rms spot size is $1.8 \mu\text{m}$ and the airy disc radius is $2.4 \mu\text{m}$

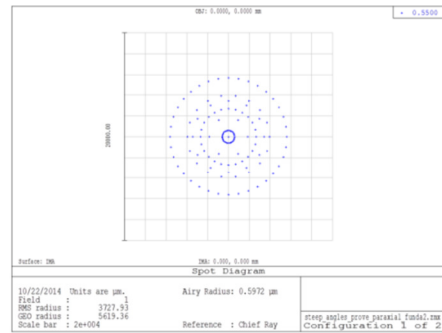
In order to demonstrate the effect of steeper incidence angles, the surface stop is then changed to 20 mm leading to incident angles as large as 63° as shown in Fig. 5.3. Since the object is an on-axis point, the only aberrations encountered by the system are spherical and defocus. These two aberrations are competing and the smallest spot size lies in the plane known as the circle of confusion. The first optimization was performed by keeping the radius of curvature constant and only optimizing the image distance. The results of this optimization are shown in Fig. 5.3(a) and (b). The rms spot size for this optimization is $3727 \mu\text{m}$ which is much

larger than the airy disc size of $0.6 \mu\text{m}$ showing that aberrations clearly dominate the performance of this lens. Also, due to the large size of the PSF the maximum available sampling for the encircled energy and cross section of the PSF were inadequate to represent them and hence are not shown here. For completeness, a second optimization was performed using both the image distance and the surface curvature as variables. The results of the optimization are shown in Fig. 5.3(c) and (d). The rms spot size for this case is $1031 \mu\text{m}$ compared to the $0.73 \mu\text{m}$ radius of the airy disc confirming that PSF is limited by aberrations rather than diffraction.

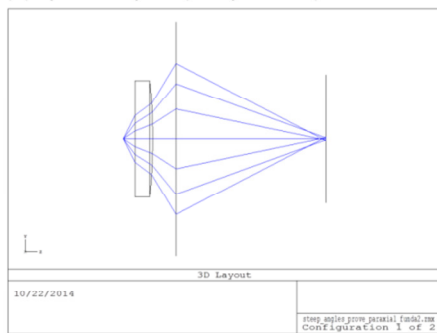
Surf.Type	Comment	Radius	Thickness	Glass	Semi-Diameter	Conic	Draw Axis?	Mode	X-cosine	Y-cosine	Z-cosine
OBJ	Standard	Infinity	10.000		0.000	0.000					
STO	Standard	Infinity	0.000		20.000	0.000					
2*	Birefring..	Infinity	15.000	NOL.SNE1.2	50.000	0.000	0.000	0	0.000	0.000	1.000
3*	Birefring..	-139.640	20.000		50.000	0.000					
4	Paraxial	92.224			100.000	0.000		30.000		1	
IMA	Standard	Infinity			50.000	0.000					



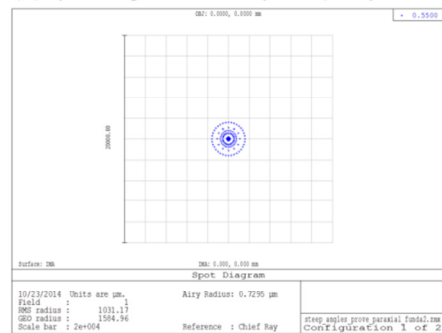
(a) System Layout (Unoptimized)



(b) Spot Diagram with Airy disc (Unoptimized)



(c) System Layout (Optimized)



(d) Spot Diagram with Airy disc (Optimized)

Fig. 5.3 Isotropic lens for large incidence angles (63°). (a) and (b) show the results with only the image distance optimized whereas in (c) and (d) both the surface curvature and the image distance was optimized. The rms spot size (and airy disc size) for the two cases are $3727 \mu\text{m}$ ($0.6 \mu\text{m}$) and $1031 \mu\text{m}$ ($0.73 \mu\text{m}$).

Thus, we have shown how large incidence angles can lead to large aberrations, especially in singlet lens systems. Aberrations are caused due to the failing of the paraxial assumption that

approximates a linear relationship between input and output refraction angles. In the next section, we make a case for a novel material that maintains the linear relationship for all incidence angles.

5.3 IRAM theory

5.3.1 Phase Linear-Refractive Material:

Here, we hypothesize a lens material that always follows a linear relation between the input and the refracted angles [Fig. 5.4(a)]. One might argue that such a lens would always act like a paraxial lens and thus provide a perfectly diffraction limited image. Let us assume for the moment that we can build such a lens and let the linearity constant be K . Without loss of generality, we can assume that the material lies in the $\hat{y}-\hat{z}$ plane with \hat{x} -axis pointing inside the plane of paper and the material interface is perpendicular to the \hat{z} -axis. For a wave incident at an angle θ_i to the surface normal, the wave vector in free space can be written as $\vec{k} = k_0 \cos(\theta_i) \hat{z} + k_0 \sin(\theta_i) \hat{y}$, where k_0 is the free space wavenumber. The Snell's law for a flat interface between air and the phase-linear material can be written as

$$\sin(\theta_i) = n \cdot \sin(\theta_i/K) \quad (5.1)$$

In order for this condition to be satisfied, the refractive index has to depend on the incident angle and can be written as

$$n_{\text{in}}(\theta_i) = \frac{\sin(\theta_i)}{\sin(\theta_i/K)} \quad (5.2)$$

A material following this equation is termed a Phase Linear-Refractive Material (PLRM) because it produces linearity in terms of the k -vector direction, which is normal to the phase fronts. As θ_i approaches 0, the index of refraction tends to K . Since the refractive index of commonly used optically transparent materials ranges between 1 and 3, we take the constant K

between these values and plot the angle dependence of the refractive index as shown in Fig. 5.4(b). These plots show the prescription for index variation as a function of incident angle for a PLRM. It is clear from the above discussion that IRAMs are inherently anisotropic. To visualize the effective index surface (k -surface) we write eq. (5.2) in terms of the phase-refraction angle

$$n_{\text{lin}}(\theta_r) = \frac{\sin(K\theta_r)}{\sin(\theta_r)} \quad (5.3)$$

The refractive index as a function of the phase-refraction angle and the corresponding effective index surface are shown in Fig. 5.4(c) and Fig. 5.4(d). The medium surrounding the IRAMs is air and the maximum refraction angle occurs for grazing incidence i.e. $\max(\theta_r) = 90^\circ/K$. Therefore, the refractive index and the effective index plots are shown up to the maximum phase-refraction angle.

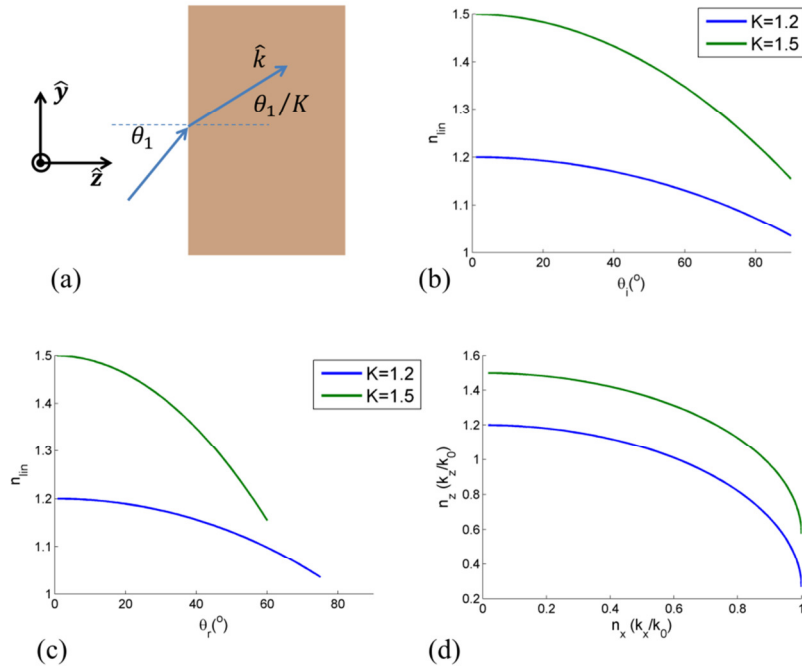


Fig. 5.4 Phase Linear-Refractive Material (PLRM) – (a) Schematic of the linear relationship between the angles of incidence and refraction. (b) Variation of the refractive index for a PLRM with respect to the incident angle (θ_i) for two different linearity constants. (c) Refractive index variation as a function of phase-refraction angle (θ_r). (d) The effective index surfaces for these materials. PLRMs guarantee that the direction of the refracted k -vector is in a linear angular relationship with the incident k -vector.

It is clear that, for a flat PLRM surface, the curvature of the effective index surface increases with increase in the value of the linearity constant K . Interestingly, it can be seen that for a small incidence angles, the index surface cross-section (Fig. 5.4(d)) resembles an ellipse similar to that traced by the extra-ordinary index of an anisotropic birefringent material with c -axis along \hat{z} for a negative uniaxial material or along \hat{y} for a positive uniaxial material.

PLRMs guarantee that the direction of the refracted k -vector is in a linear angular relationship with the incident k -vector. However, PLRMs are clearly anisotropic and hence the direction of energy flow given by the Poynting vector is not aligned with the k -vector. Further, the Poynting vector direction is provided by the normal to the index surfaces for a given incident vector. Thus we define a linear Poynting material (LPM) as a material with the Poynting vector direction linearly related to the incident Poynting vector for all angles of incidence.

5.3.2 Linear Poynting Material:

The direction of energy flow in an anisotropic material is along the normal to the momentum-surface at a given point which typically is different from the direction of phase front propagation. Here we derive the equation for a material with the direction of energy flow linear with respect to the incidence angle. Assuming that such a momentum surface exists, we could plot $k_z (n_z)$ as a function of $k_x (n_x)$ for $k_y = 0$ (without loss of generality) as shown in Fig. 5.5(b).

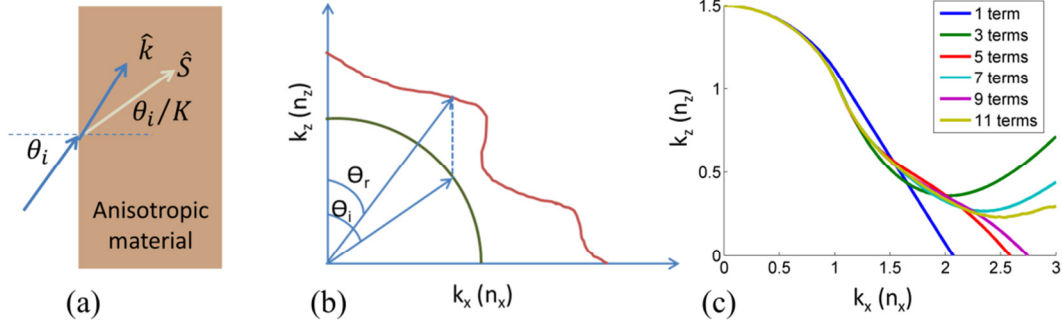


Fig. 5.5: Linear Poynting material (LPM). (a) Schematic of the relationship between angle of incidence and angle of Poynting vector (b) Schematic of a hypothetical k -surface relationship between air (green curve) and an LPM (red curve). The dotted lines represent conservation of transverse momentum (k_x) (c) The index curves for LPM calculated at increasing approximation and showing convergence to the solution.

The green curve represents the k -surface of air and the red curve represents the k -surface of an LPM. Using Snell's law we have

$$n \cdot \sin(\theta_r) = 1 \cdot \sin(\theta_i) \quad (5.4)$$

where $n = \sqrt{n_x^2 + n_z^2}$. The angle of the normal to the curve, Φ , as measured from the n_z axis is given by,

$$\tan \Phi = -\frac{dn_z}{dn_x} \quad (5.5)$$

For linearity Φ should be a linear function of θ_i so

$$-\frac{dn_z}{dn_x} = \tan\left(\frac{\theta_i}{K}\right) \quad (5.6)$$

Substituting eq. (5.4) in eq. (5.6) we get,

$$-\frac{dn_z}{dn_x} = \tan\left(\frac{1}{K} \sin^{-1}(n \cdot \sin(\theta_r))\right) \quad (5.7)$$

But, the refraction angle is related to the projection of effective index along \hat{x} and \hat{z} by $\tan \theta_r = n_x/n_z$. Substituting back we get

$$-\frac{dn_z}{dn_x} = \tan\left(\frac{1}{K} \sin^{-1}\left(n \cdot \sin\left(\tan^{-1}\left(\frac{n_x}{n_z}\right)\right)\right)\right) \quad (5.8)$$

Noting that $\tan^{-1}\left(\frac{n_x}{n_z}\right) = \sin^{-1}\left(\frac{n_x}{n}\right)$ leads to

$$-\frac{dn_z}{dn_x} = \tan\left(\frac{1}{K} \sin^{-1}(n_x)\right) \quad (5.9)$$

Integrating eq. (5.9) we get,

$$n_z = \int -\tan\left(\frac{1}{K} \sin^{-1}(n_x)\right) dn_x \quad (5.10)$$

This remarkable simple equation defines the desired material property. Unfortunately it is not easily integrable, so we use the following approximation for the tan series

$$\tan(y) = y + \frac{y^3}{3} + \frac{2y^5}{15} + \frac{17y^7}{315} \dots \quad (5.11)$$

A ray that is incident normal to the surface of the lens has k_x as 0. Thus the index observed by the ray is n_z and causes a change in the momentum but not the direction. Thus we can assume that when n_x is 0, n_z tends to K which can be used to find the integration constant. In Fig. 5.5(c) we plot this momentum surface for increasing number of terms in the tan() series. All the curves start at the chosen n_z of 1.5 (picked on purpose for this solution). For small angles all the curves follow the same trend, while at large angles, the curves deviate but show clear convergence as the number of terms increases.

It is clear that the refractive index properties of PLRM and LPM are different but nevertheless; we term these new classes of materials as infinitely refraction-linear artificial material (IRAM). As mentioned earlier, a striking feature of IRAM is the similarity of the refractive index properties to birefringence materials. Although naturally occurring birefringent materials such as calcite could emulate IRAM reasonably well (see Appendix 5C to the chapter), the space of birefringent materials is explored here using materials by design. Almost arbitrary

birefringence (within certain limits) can be attained using periodic nanostructures[140]–[144]. Given a 1-D periodic array of two materials of indices n_1 and n_2 with periods a and b , the structure effectively behaves like a birefringent material with the following indices [145] (in the long wavelength limit):

$$\begin{bmatrix} n_o \\ n_e \end{bmatrix} = \frac{1}{(a+b)^{1/2}} \begin{bmatrix} n_1 \cdot a^{1/2} \\ n_2 \cdot b^{1/2} \end{bmatrix} \quad (5.12)$$

Thus the ordinary and extra-ordinary indices can be tailored by the refractive indices of the constituent materials and their relative periodicities. In particular the use of form birefringence[140]–[142] is an attractive approach to approximate the ideal IRAM.

5.4 Uniaxial crystals as PLRM:

In section 5.3.1, we saw that the effective index curve for PLRM resembles an ellipse where the refractive index is a decreasing function of the incidence and hence the refraction angle. This is equivalent to the effective index curve of a negative uniaxial crystal with c -axis along the surface normal or a positive uniaxial crystal with c -axis perpendicular to the surface normal. For simplicity, we only consider the case of negative uniaxial crystal, keeping in mind that the positive crystal will yield the same results with the o- and eo- refractive indices switched. It can be shown that even for c -axis approximately parallel to the surface-normal, the effective index curves would match closely. However, only transcendental solutions exist for cases where the c -axis does not lie parallel or perpendicular to the interface (see Appendix 5A). Therefore, we consider the case where the angle between the c -axis and the surface normal is 0° as shown in Fig. 5.6. The angle of phase-refraction and the Poynting vector for the eo-ray are denoted by θ_e and θ_s respectively.

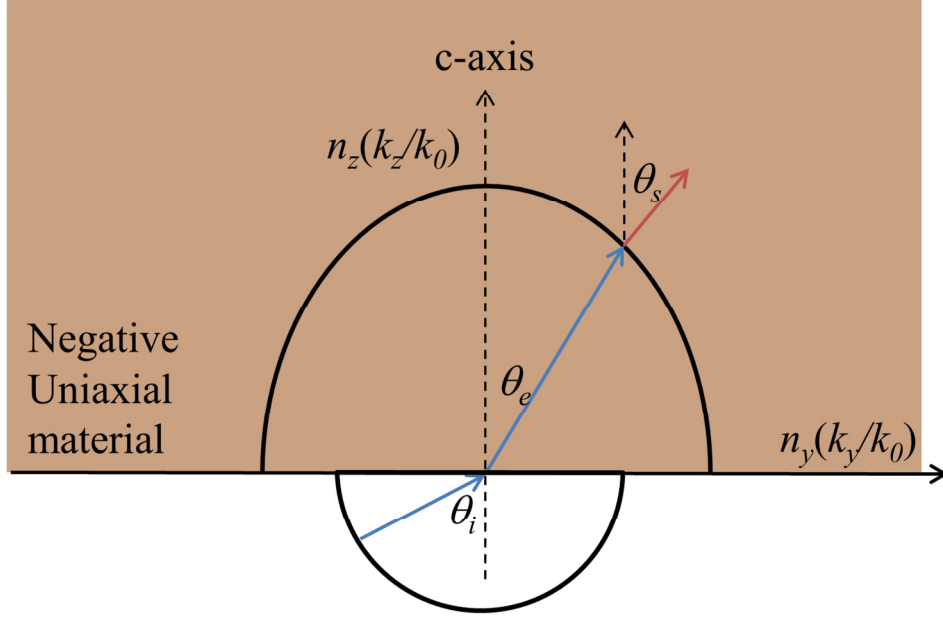


Fig. 5.6 Index ellipse of the eo-ray refracted at an angle θ_e . The c -axis is along the surface normal.

Following the development in Appendix 5A, the generalized Snell's law for this case can be written as

$$\sin(\theta_i) = \frac{n_o n_e}{\sqrt{n_o^2 \sin^2(\theta_e) + n_e^2 \cos^2(\theta_e)}} \sin(\theta_e) \quad (5.13)$$

Inverting and squaring the above equations we get, for $\theta_i > 0$

$$\frac{n_o^2 \sin^2(\theta_e) + n_e^2 \cos^2(\theta_e)}{n_o^2 n_e^2 \sin^2(\theta_e)} = \frac{1}{\sin^2(\theta_i)} \quad (5.14)$$

When the wave is incident normal to the surface, i.e. $\theta_i = 0$, eq. (5.13) can be directly used to get $\theta_e = 0$. For non-normal incidences, eq. (5.14) can be written as,

$$\frac{\cot^2(\theta_e)}{n_o^2} = \frac{1}{\sin^2(\theta_i)} - \frac{1}{n_e^2} \quad (5.15)$$

This equation can be further simplified as,

$$\theta_e = \cot^{-1} \left(\frac{n_o}{n_e \sin(\theta_i)} \sqrt{n_e^2 - \sin^2(\theta_i)} \right) \quad (5.16)$$

This simple analytical equation can be used to calculate the phase refraction angle of the eo-wave for c -axis along the surface normal. The direction of energy propagation is given by the surface normal to the effective index curve at the point where the transverse momentum is conserved (see Fig. 5.6). The two components of the index ellipse n_z and n_y are just projections of the effective index on the \hat{z} - and \hat{y} -axis respectively, i.e.

$$\begin{aligned} n_y &= n_{\text{eff}} \sin(\theta_e) \\ n_z &= n_{\text{eff}} \cos(\theta_e) \end{aligned} \quad (5.17)$$

Thus, the index ellipse can also be written in the following form

$$\frac{n_z^2}{n_o^2} + \frac{n_y^2}{n_e^2} = 1 \quad (5.18)$$

It can easily be shown that the direction of Poynting vector is related to the derivative of the index ellipse by the following equation,

$$\tan(\pi/2 - \theta_s) = \cot(\theta_s) = -\frac{dn_y}{dn_z} \quad (5.19)$$

Differentiating eq. (5.18), we get

$$-\frac{dn_y}{dn_z} = \frac{n_z}{n_y} \frac{n_e^2}{n_o^2} \quad (5.20)$$

Substituting eq. (5.17) in eq. (5.20), we get

$$-\frac{dn_y}{dn_z} = \frac{n_{\text{eff}} \cos(\theta_e)}{n_{\text{eff}} \sin(\theta_e)} \frac{n_e^2}{n_o^2} = \frac{n_e^2}{n_o^2} \cot(\theta_e) \quad (5.21)$$

Substituting eq. (5.21) in eq. (5.19), we get the equation for direction of Poynting vector of the extra-ordinary ray in terms of its phase-refraction angle or in terms of the incidence angle (using eq. (5.16)) as follows

$$\theta_s = \cot^{-1} \left(\frac{n_e^2}{n_o^2} \cot(\theta_e) \right) = \cot^{-1} \left(\frac{n_e}{n_o \sin(\theta_i)} \sqrt{n_e^2 - \sin^2(\theta_i)} \right) \quad (5.22)$$

The relation between the Poynting vector and incidence angle for the eo-ray is similar in form to that between the phase-refraction angle and incidence angle. A similar procedure can be

used to determine the direction of energy propagation inside an ideal PLRM. The effective refractive index of an ideal PLRM as a function of the refraction angle θ_r is given by eq. (5.3).

The components n_x and n_z can then be written as

$$\begin{aligned} n_y &= n_{lin} \sin(\theta_r) = \frac{\sin(K\theta_r)}{\sin(\theta_r)} \sin(\theta_r) = \sin(K\theta_r) = \sin(\theta_i) \\ n_z &= n_{lin} \cos(\theta_r) = \frac{\sin(K\theta_r)}{\sin(\theta_r)} \cos(\theta_r) = \sin(\theta_i) \cot(\theta_i/K) \end{aligned} \quad (5.23)$$

The equation for n_y is just Snell's law. Using a similar procedure as before, the direction of Poynting vector θ_s for a PLRM is given by

$$\theta_s = \tan^{-1} \left(-\frac{dn_z}{dn_y} \right) = \tan^{-1} \left(\frac{\tan(\theta_i)}{K \sin^2(\theta_i/K)} - \cot(\theta_i/K) \right) \quad (5.24)$$

Again, the angle of Poynting vector for the case of a PLRM is given by a simple analytical function of the incidence angle and the linearity constant. Equipped with these equations, we can now compare the properties of a negative uniaxial material to that of an ideal PLRM.

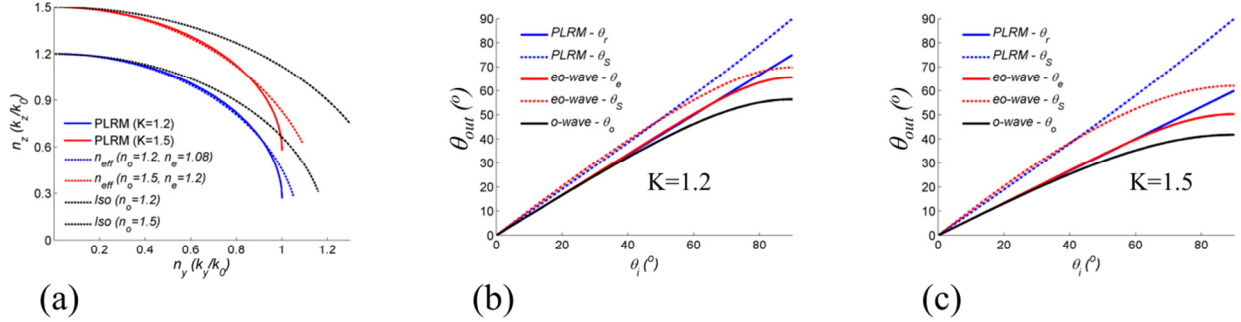


Fig. 5.7 PLRM vs. negative uniaxial material: (a) Comparison of the effective index curve for PLRM (solid blue and red) with effective index of the eo-wave (dashed blue and red) and o-wave (dashed black) of a uniaxial material. The linearity constants considered for PLRM are $K=1.2$ (blue) and $K=1.5$ (red). The o- and eo- refractive index are chosen to roughly match the index of PLRM. The phase-refraction (solid) and Poynting vector angles (dashed) for PLRM (blue) and the o- (black) and eo-wave (red) for the uniaxial material are shown in (b) $K=1.2$ and (c) $K=1.5$.

The effective index curves for an ideal PLRM and for the o-wave and eo-wave of a negative uniaxial material are shown in Fig. 5.7(a). For consistency, we again consider the two PLRM cases with linearity constants $K=1.2$ (solid blue) and $K=1.5$ (solid red). The effective-index of the o-wave (solid black) is a sphere with refractive index equal to the linearity constant. The eo- refractive indices are chosen to match the effective index of the eo-wave (dashed blue and red) with PLRM. A strong overlap is seen between the effective index curves of the ideal PLRM and that of the eo-wave of the chosen negative uniaxial crystal making them strong contenders for the realization of IRAM. However, a good measure of the performance of IRAM candidates is the comparison of the refraction angles as a function of incidence angle. The phase-refraction (solid) and the Poynting vector (dashed) angles for an ideal PLRM (blue) and the o- (black) and eo-wave (red) of the negative uniaxial crystal are shown as functions of the incident in Fig. 5.7(b) for $K=1.2$ and Fig. 5.7(c) for $K=1.5$. The Poynting and phase refraction angles for the o-wave are equal and also represent the performance of an isotropic material with refractive index n_o . It is noteworthy that even though the PLRM was designed for linear phase refraction, the direction of Poynting energy also shows a strong linear behavior albeit with a different linearity constant than K . This owes to the fact that the curvature of the effective index curve is in a linear relationship to the input and phase-refracted angles. Also as expected, the chosen negative uniaxial material does a good job of approximating the ideal PLRM. For both $K=1.2$ and $K=1.5$, the chosen material shows linearity between the input and output phase angles for incidence angles of up to 75° (using $\sim 5\%$ deviation) in contrast to isotropic material that stays linear for incidence angles of up to 40° . As for the Poynting angles, the self-consistency of isotropic materials makes them linear for up to 40° as well. On the contrary, the Poynting vector of the uniaxial material shows linearity up to angles of 50° with a slight kink for incidence angles

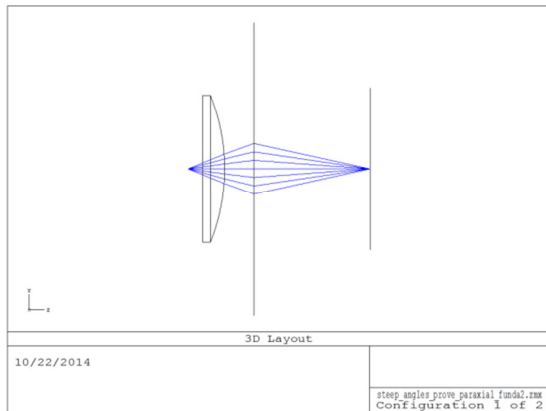
between 10° and 30° . These results conform well with our original hypothesis that negative (or positive with c -axis perpendicular to surface normal) uniaxial materials are a good approximation for the IRAM behavior. In the next section, we will test our hypothesis by comparing the performance of uniaxial lenses to the conventional lenses in Zemax using the lens system described earlier. It should be noted that lenses require at least one curved surface to be able focus the rays. The development of curved PLRM surfaces is more involved and is presented separately in Appendix 5B to the chapter. It is clear that anisotropy provides us with a degree of freedom to explore the space of ideal refraction linear materials. Similarly chirality can be utilized as another degree of freedom to further steer materials towards the perfect IRAMs. The properties of chiral materials and the chirality values required for IRAM are discussed in Appendix 5C to the chapter. In the next few sections, we present simulations of uniaxial lenses using Zemax.

5.4.1 Uniaxial material IRAM lens

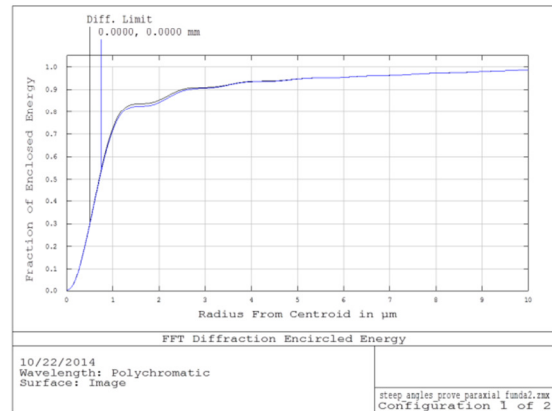
In section 5.2, we showed that the paraxial approximation fails at steeper angles leading to extremely large and aberrated PSFs. A uniaxial material on the other hand closely follows an IRAM for angles that are twice as large as that for an isotropic material. Hence we expect the performance of uniaxial material lenses to be superior to conventional lenses in terms of the size of the PSF. Following our earlier development in Zemax, we now trace the extra-ordinary ray by switching to Mode 1 and re-optimizing the image distance to account for the change in marginal ray angles as shown in Fig. 5.8. We also saw that a uniaxial material with ordinary and extra-ordinary refractive indices of 1.5 and 1.2 is a strong candidate for the IRAM approximation and is the material of choice for the uniaxial lens. The maximum incidence angle is on the order of 22° keeping the system in the paraxial regime. After the optimization it can be seen that the encircled energy is completely contained within the diffraction limited spot size. Moreover, the

rms spot size in the case of the uniaxial lens is $0.57 \mu\text{m}$ compared to the rms spot size of $1.8 \mu\text{m}$ (Fig. 5.2(c)) for the conventional isotropic lens. Clearly the uniaxial lens shows better performance owing to the approximate linearity property between the input and refracted angles.

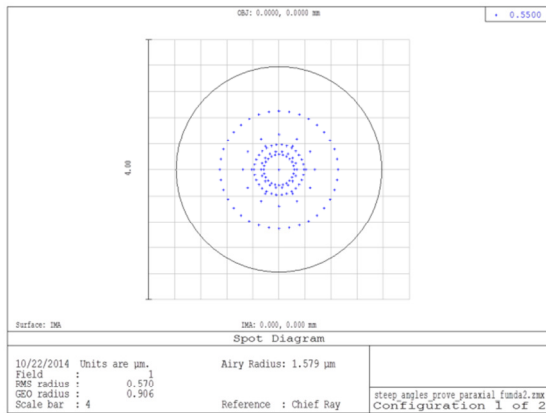
Surf>Type	Comment	Radius	Thickness	Glass	Semi-Diameter	Conic	Draw Axis?	Mode	X-cosine	Y-cosine	Z-cosine
OBJ	Standard	Infinity	10.000		0.000	0.000					
STO	Standard	Infinity	0.000		4.000 U	0.000					
2*	Birefring..	Infinity	15.000	NO1.SNE1.2	50.000 U	0.000	0.000	1	0.000	0.000	1.000
3*	Birefring..	-133.673 V	20.000		50.000 U	0.000					
4	Paraxial		79.082 V		100.000 U			30.000	1		
IMA	Standard	Infinity	-		55.000 U	0.000					



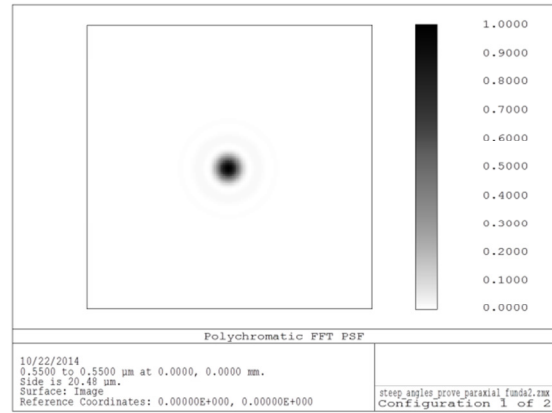
(a) System Layout



(b) Diffraction encircled energy



(c) Spot Diagram with Airy disc



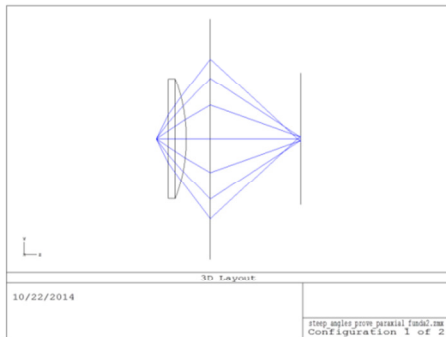
(d) PSF cross-section

Fig. 5.8 Uniaxial thin lens in the paraxial regime: The maximum angle of incidence is given by $\tan^{-1}(4/10) \approx 22^\circ$. (b) Most of the energy is contained in the diffraction limited spot which is also seen in (c). The rms spot size is $0.57 \mu\text{m}$ and the airy disc radius is $1.579 \mu\text{m}$

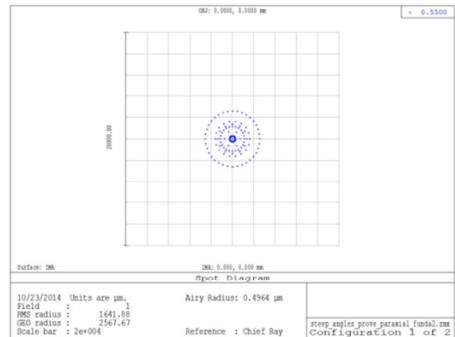
We will now show that even outside the paraxial regime, the uniaxial material shows smaller PSF sizes than their isotropic counterparts. As shown in Fig. 5.9, the stop size is changed

to 20mm increasing the angle of incidence to 63° . The system was optimized in two different ways: keeping surface curvature constant and optimizing the image distance (Fig. 5.9(a) and (b)) and optimizing the curvature and image distance simultaneously (Fig. 5.9(c) and (d)). In the optimization using only the image distance, the rms spot size was $1641 \mu\text{m}$ as compared to the rms spot size of $3727 \mu\text{m}$ for the conventional case (Fig. 5.3(b)). When both the curvature and image distance were optimized, the rms spot size was seen to be $495 \mu\text{m}$ as compared to $1031 \mu\text{m}$ in the conventional case (Fig. 5.3(d)). **Thus the uniaxial lens shows about a 200% improvement in spot size as compared to the conventional lenses.**

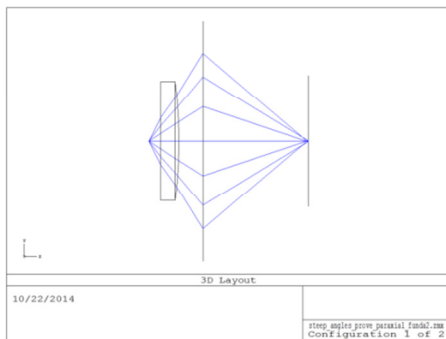
SurfType	Comment	Radius	Thickness	Glass	Semi-Diameter	Conic	Draw Axis?	Mode	X-cosine	Y-cosine	Z-cosine
OBJ	Standard	Infinity	10.000			0.000					
STC	Standard	Infinity	0.000		20.000	0.000					
2*	Spherefring...	Infinity	15.000	NO1.5NE1.2	50.000	0.000	0.000	1	0.000	0.000	1.000
3*	Spherefring...	-392.678	20.000		50.000	0.000					
4	Paraxial	87.837			100.000	0.000		30.000	1		
IMC	Standard	Infinity			95.000	0.000					



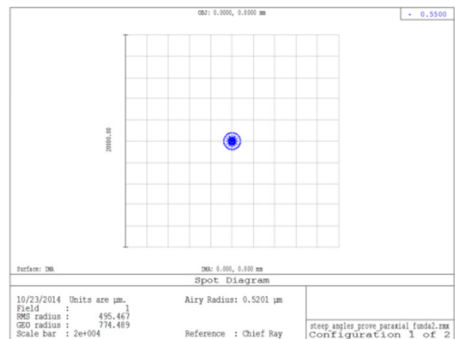
(a) System Layout (Unoptimized)



(b) Spot Diagram with Airy disc (Unoptimized)



(c) System Layout (Optimized)



(d) Spot Diagram with Airy disc (Optimized)

Fig. 5.9 Uniaxial thin lens for large incidence angles (63°): (a) and (b) show the results with only the image distance optimized whereas in (c) and (d) both the surface curvature and the image distance were optimized. The rms spot size (and airy disc size) for the two cases are $1641 \mu\text{m}$ ($0.49 \mu\text{m}$) and $495 \mu\text{m}$ ($0.52 \mu\text{m}$).

5.4.2 Uniaxial IRAM lens behavior for off-axis field points

In the last section we saw the effect of using a uniaxial lens with $n_o=1.5$ and $n_e=1.2$ when imaging an on-axis point. In order to further evaluate the performance of uniaxial materials we calculate the rms spot size of uniaxial lenses with increasing birefringence for on-axis as well as off-axis field points. The range of possible birefringence was increased by choosing a high ordinary refractive index of 2.7. For each new birefringent material, we optimize the wavefront using the radii of the two surfaces as parameters for optimization. In addition, the lenses are optimized for an object placed at infinity and the image plane constrained at 100mm from the lens surface. Only the on-axis point was given a weight during optimization. After optimization we extract the spot size for image heights up to 40mm for both the ordinary and extraordinary rays.

Fig. 5.10 shows the variation of the spot size as a function of image height for different birefringent materials. It can be noted that as the birefringence is increased, the spot size decreases. At the image height of 40mm, for a material with indices 2.7 and 1.5, the spot size shows a 33% improvement relative to the isotropic lens with index 2.7. We also show the spot size for the ordinary ray of the optimized lens design, showing about 20% improvement for an image height of 40mm. This is remarkable as both polarization images can be improved for wide angles.

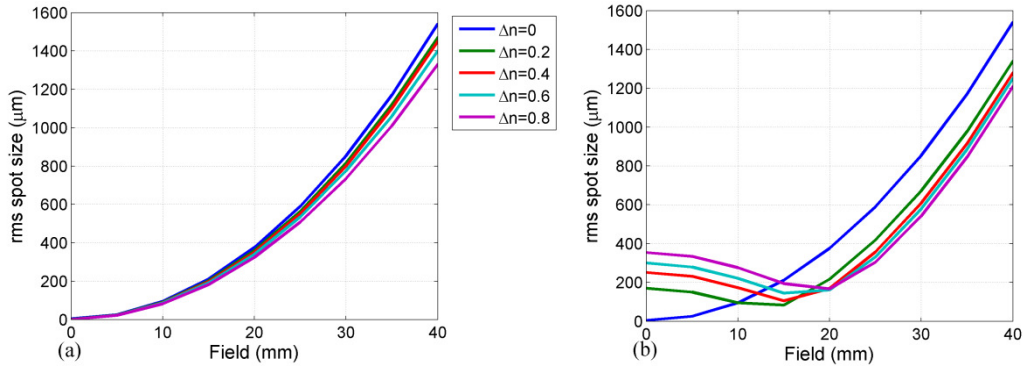


Fig. 5.10 Artificial dielectric lenses improve spot size for highly nonparaxial rays. The left plot shows the extraordinary rays rms spot size as a function of the difference between ordinary and extraordinary indices Δn . The right plots show the spot size for the ordinary rays. Interestingly, both rays improve spot size for large fields of view.

In Fig. 5.11 we also show the spot size as a function of relative birefringence, which we define as $\Delta\varepsilon/\varepsilon$, where ε is the permittivity of the material. Each curve represents a different image height and the spot size is normalized according to the spot size observed for the isotropic lens ($\Delta\varepsilon=0$) for the respective field height. Since each of the birefringent materials were optimized for the on-axis point (Field=0mm), the blue curve shows a very drastic change in the spot size at a relative birefringence of 0.2 and then remains constant henceforth. All the other image heights show a similar trend for spot size reduction. The figure on the right shows these curves for the ordinary ray. For field heights up to 15mm, the spot size seems to grow with increase in birefringence but for larger field heights, the ordinary ray starts to show a similar behavior to the extra-ordinary ray. This suggests that even though birefringent materials are very polarization sensitive, with proper design, they can yield a better performance than their isotropic counterparts irrespective of the polarization state of the ray used.

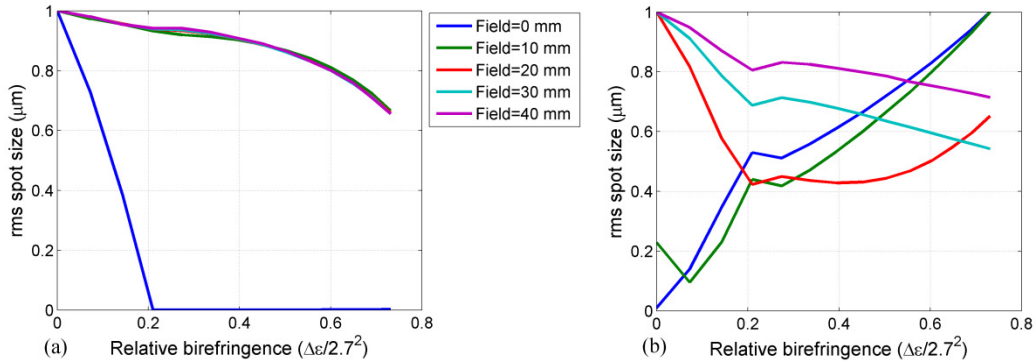


Fig. 5.11 RMS spot size as a function of relative birefringence: Left plots are for extraordinary rays while right plots are for ordinary rays.

Apart from a smaller spot size, a good lens is characterized by the lack of aberrations. A good measure for the various lens aberrations are the Seidel coefficients. Fig. 5.12 shows the following Seidel coefficients as a function of relative birefringence: Spherical (blue curve), Coma (green curve), Astigmatism (red curve), and Distortion (magenta curve). This type of study is critical for the optimal design of specific imaging systems. Systems that have Seidel coefficients close to zero are less prone to aberrations. The region where all the coefficients are low is between relative birefringence of 0.3 and 0.4. But if distortion is not a concern, then relative birefringence between 0.1 and 0.2 show a superior performance. Thus, Seidel coefficients provide another metric to evaluate the performance of IRAM lenses.

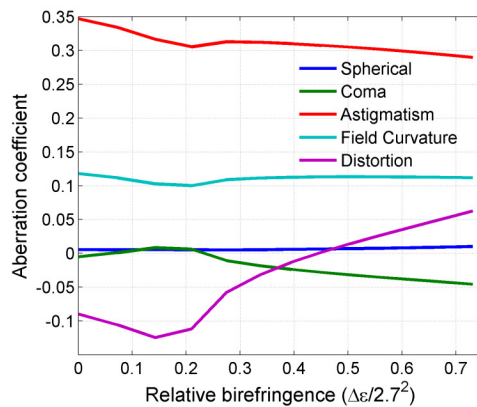


Fig. 5.12 Seidel aberrations as a function of relative birefringence

5.4.3 Real life, high impact application of the IRAM paradigm

The calculations and simulations so far show that artificial material lenses, owing to the superior performance of its extraordinary polarization have the potential to reduce the complexity of multi-lens systems. We test this hypothesis by trying to match or improve the design of a high end lens. For this purpose we pick one of the lenses used on the Mars rover Curiosity[146]. The lens is primarily used in navigation camera. These lenses have been carefully designed so any gain in performance, size, or weight could have a strong impact.

The original lens works for a range of wavelengths, ranging from 0.6 to 0.8 micron but after observation of the rms spot size, it shows best performance at 0.7 micron. For a fair comparison, we used the 0.7 micron wavelength to optimize the spot size. Also, the original Zemax design of the lens consisted of an on-axis and an off-axis object point at 30mm. Two additional off-axis object points at 10 and 20 mm were added for a more complete analysis.

The lens setup is shown in part A of Fig. 5.13. It consists of two filters in the front and then a 4-lens system. Also shown is the spot size of the four fields. The image distance was optimized to account for the addition two off-axis field points.

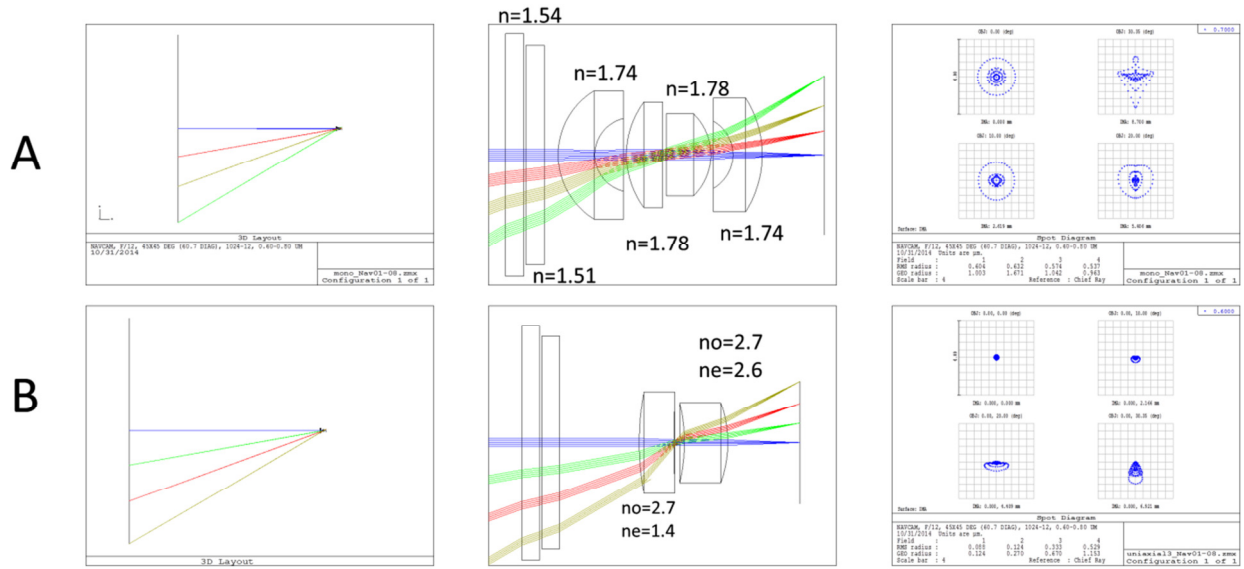


Fig. 5.13 Comparison of Mars rover navigation lens with alternative IRAM lens: The three columns show the full view, zoomed view of the lens system and the spot diagram for the navigation lens on the Mars Rover. Row A shows the original configuration consisting of four lenses. Row B shows the configuration that uses two IRAM lenses instead. A reduction in spot size is observed using the alternative IRAM configuration.

As shown in part (B), the IRAM design using a modified uniaxial setup replaces the 4-lens system with a 2-lens system with the radii of the lens optimized to get the lowest spot for the given field of view. By comparing the spot diagrams it can be seen that the modified uniaxial lens has a tighter focus for on-axis and off-axis fields. Table 5.1 shows the various spot sizes for both configurations at different field points. Improvement in the rms spot size is observed over the whole field of view with highest reduction of about 6 times observed for the on-axis field point.

Lens/field	Field 1 (μm)	Field 2(μm)	Field 3(μm)	Field 4(μm)
Mars rover	0.6	0.57	0.53	0.63
Uniaxial IRAM	0.088	0.12	0.33	0.52

Table 5.1 Comparison of R.M.S. spot size of the original Mars rover lens system to the reduced element IRAM design. The four field points represent object heights at 0, 10, 20 and 30 mm respectively

It is remarkable that a very preliminary design can perform better with a much simpler system in terms of number of surfaces. It should be emphasized that still great efforts should be invested before such a lens can even be prototyped. Further, the original lens could have been optimized with respect to other (unknown to us) constraints, so this comparison should be considered only as an illustration and not construed as an absolute statement that an IRAM solution will be always the best. However, we believe this example serves as strong motivation for the capabilities of IRAM for simpler and better lens designs based on the added degrees of freedom in material design.

5.5 Conclusion

In conclusion we have shown that approximations to infinitely refraction linear materials exist via proper use of anisotropies. We have further emphasized the distinction between k -vector linearity and Poynting vector linearity and found analytical expressions. We also established that properly designed IRAM lenses indeed show better performance with simpler and lighter designs that outperform current state-of-the-art isotropic multi-element options. Further, in some situations both polarization states can be optimized to create very efficient lenses. By using the example of a known lens, we showed that IRAM lenses have the potential to simplify complex lens systems while improving performance. While this approach is clearly unconventional, it provides an opportunity to explore a new way of thinking both in optical and material design.

APPENDIX 5A PROPERTIES OF UNIAXIAL CRYSTALS

In this section we briefly describe the properties of a uniaxial anisotropic material. Unlike isotropic media, the characteristics of an electromagnetic wave in an anisotropic media depend

on the direction of propagation. Anisotropy in crystals arises due to the unequal response of the optical material to the incident electric field along the different crystal axes. This implies that the material properties (permittivity and permeability) that define the constitutive relations are no longer scalar quantities and the constitutive relations are described tensors. The displacement vector and the electric field vector are related by the following equation

$$\overline{D} = \epsilon_0 \overline{\epsilon} \overline{E} \quad (5.25)$$

where $\overline{\epsilon}$ is a 3x3 tensor that relates the components of the displacement vector to each component of the electric field vector. We will only concern ourselves with non-magnetic materials and thus the relation between magnetic flux \overline{B} and the magnetic field \overline{H} is a scalar one. It can be shown that by appropriately choosing the axes, the permittivity tensor can be diagonalized leading to the following relation

$$\begin{pmatrix} D_x \\ D_y \\ D_z \end{pmatrix} = \epsilon_0 \begin{pmatrix} \epsilon_x & 0 & 0 \\ 0 & \epsilon_y & 0 \\ 0 & 0 & \epsilon_z \end{pmatrix} \begin{pmatrix} E_x \\ E_y \\ E_z \end{pmatrix} \quad (5.26)$$

This new set of axes is called the principal axes and ϵ_x , ϵ_y , and ϵ_z are the principal dielectric constants. When the three principal dielectric constants are equal, i.e. $\epsilon_x = \epsilon_y = \epsilon_z$ we get back the scalar constitutive relation of an isotropic material, whereas when $\epsilon_x \neq \epsilon_y \neq \epsilon_z$, the material is known as a biaxial material. The intermediate case when $\epsilon_x = \epsilon_y \neq \epsilon_z$ is known as a uniaxial material where, without loss of generality, the principal axes can always be chosen to make the dielectric constant along \hat{z} different from the constants along \hat{x} and \hat{y} . In the case of uniaxial materials, we can write $\epsilon_x = \epsilon_y = \epsilon_t = (n_o)^2$ and $\epsilon_z = (n_e)^2$, where ϵ_t is also known as the transverse dielectric permittivity and n_o and n_e denote the ordinary and extra-ordinary refractive indices of the uniaxial crystal. From here on we will only consider the case of uniaxial crystals. The crystals where $n_o < n_e$ are termed as positive and the ones where $n_o > n_e$ are termed as negative

uniaxial crystals. Therefore, electromagnetic waves that are polarized along the \hat{z} -axis, also known as the c -axis, propagate with a phase velocity of c/n_e , whereas the ones polarized perpendicular to the c -axis propagate with a phase velocity of c/n_o , c being the speed of light in vacuum. Consider now the case when the electromagnetic wave propagates at an angle θ to the optical axis. Note that in the case of uniaxial materials, the properties of the wave only depend on the polar angle it subtends with the c -axis. Therefore, without loss of generality we can consider the plane of propagation to lie in the $\hat{y}-\hat{z}$ plane. The two Eigen solutions of such a wave are known as the ordinary wave (o-wave) and the extraordinary wave (eo-wave). The polarization of the o-wave always lies perpendicular to the c -axis (i.e. along \hat{x}) and the refractive index observed by the o-wave is n_o . The polarization of the eo-wave is at an angle to the c -axis and the refractive index observed is given by

$$\frac{1}{n_{eff}^2(\theta)} = \frac{\cos^2(\theta)}{n_o^2} + \frac{\sin^2(\theta)}{n_e^2} \quad (5.27)$$

where $n_{eff}(\theta)$ is the effective refractive index and θ is the angle that the wave vector makes with the c -axis. It is clear from eq. (5.27) that effective index curve traces an ellipse with the major and minor axis equal to the ordinary and extra-ordinary refractive indices of the crystal. For waves propagating parallel to the c -axis, the angle $\theta = 0^\circ$ and refractive index of both the eo-and o-wave is equal to n_o ; whereas for waves propagating perpendicular to the c -axis, eo-wave propagates with refractive index $n_{eff} = n_e$.

Now consider the case when an arbitrarily polarized wave is obliquely incident at the interface between air and a uniaxial material. As shown in Fig. 5.14, the angle of incidence, the normal to the interface and the refracted angle lie in the $\hat{y}-\hat{z}$ plane. Without loss of generality we can assume that the \hat{z} -axis is perpendicular to the uniaxial surface. The incident wave at an

angle θ_i , gives rise to two refracted waves, the o-wave at angle θ_o and the eo-wave at angle θ_e respectively. The c -axis of the uniaxial material is assumed to lie at an angle θ_c .

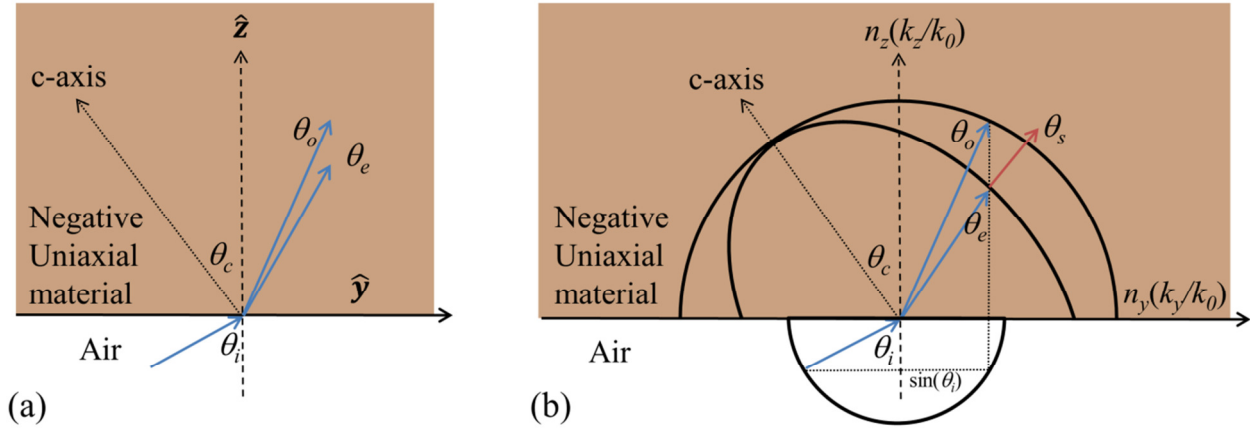


Fig. 5.14 Refraction at the interface of a negative uniaxial material: (a) Schematic of the incident and refraction angles at the interface between air and a negative uniaxial material. (b) k -space diagram at the interface. This is also used as a graphical solution to find the phase-refraction angles and the direction of energy propagation.

In order to find the refracted angles θ_o and θ_e we apply conservation of transverse momentum (Snell's law) for the o-wave and eo-wave at the interface giving,

$$\begin{aligned} \sin(\theta_i) &= n_o \sin(\theta_o) \\ \sin(\theta_i) &= n_{eff}(\theta) \sin(\theta_e) \end{aligned} \quad (5.28)$$

The refractive index seen by o-wave equals the ordinary refractive index of the material and thus follows the linear Snell's law. As for the eo-wave, the effective refractive index is given by the index ellipse in eq. (5.27), where θ is the angle between the propagation direction and the c -axis. This relationship is not necessarily linear in $\sin(\theta_i)$ and $\sin(\theta_e)$ and is known as the generalized Snell's law. Since the c -axis is at an angle θ_c to the \hat{z} -axis, the effective index is now a function of the refraction angle θ_e and the c -axis angle θ_c . In the case shown in Fig. 5.14, θ_c is positive for c -axis lying on the same side of normal as the incident angle and negative when it is

on the other side of normal. Therefore the effective angle for the index ellipsoid for the case considered is given by $\theta = \theta_c + \theta_e$. and n_{eff} is given by

$$\frac{1}{n_{eff}^2(\theta)} = \frac{1}{n_{eff}^2(\theta_c, \theta_e)} = \frac{\cos^2(\theta_c + \theta_e)}{n_o^2} + \frac{\sin^2(\theta_c + \theta_e)}{n_e^2} \quad (5.29)$$

Substituting back in eq. (5.28), with a few algebraic manipulations, we get,

$$\sin(\theta_i) = \frac{n_o n_e}{\sqrt{n_o^2 \sin^2(\theta_e + \theta_c) + n_e^2 \cos^2(\theta_e + \theta_c)}} \sin(\theta_e) \quad (5.30)$$

The above equation is a transcendental equation in θ_i and θ_e which cannot always be solved analytically. The graphical solution for the case considered is shown in Fig. 5.14(b). The k -surface for the waves in free-space and for the o-wave and the eo-wave in the uniaxial medium are shown. The c -axis is at the point of intersection of the k -surfaces for the o and eo-wave. We know that in any given medium, the k -vector of the wave is proportional to the refractive index seen by the wave, i.e. $k = nk_0$, where k_0 is the free space wave-number. Therefore the graphical solution is obtained by plotting the effective index surfaces. For a refractive index that is independent of the angle of incidence or refraction, the surfaces are spheres (circles in cross-section) with radius proportional to the refractive index. As for the k -surface of the eo-wave, it is the index ellipsoid (ellipse in cross-section) described in eq. (5.30). Therefore, to find the solution graphically, we find the transverse momentum of the incident wave by finding the projection of k -vector along the \hat{y} -axis, which in case of air is proportional to $\sin(\theta)$. Using conservation of transverse momentum, a straight line, parallel to the \hat{z} -axis, is drawn from the intersection of the k -vector with the unity circle in air to the k -surfaces in the material. The o- and eo- refraction angles can be found from the intersection of the momentum conservation line with the k -surfaces in the medium. It should be noted that the angles θ_o and θ_e in the medium represent the phase-refraction angles i.e. they define the direction perpendicular to the phase-

fronts. The direction of energy propagation, which is also along the Poynting vector, is given by the surface normal to the k -surface at the point where the phase-angle intersects the k -surface. For isotropic k -surfaces, the direction of phase and energy propagation is the same, but for anisotropic surface, these two directions might differ and hence we denote the direction of energy propagation as θ_s . In general, the direction of energy propagation for the o-wave and eo-wave is different and this leads to a phenomenon known as birefringence (also known as double-refraction). Birefringence causes two images of the same object to be seen when we look through a non-opaque uniaxial material (ex: calcite). This difference in direction of energy and phase propagation can lead to a phenomenon known as spatial walk-off, where even for normal-incidence, the eo-ray travels at an oblique angle to the propagation direction for crystals where the c -axis is neither parallel nor perpendicular to the direction of propagation[139].

APPENDIX 5B CURVED UNIXIAL SURFACES AS IRAM

The calculations for uniaxial materials as IRAM candidates shown in section 5.2 are valid for a planar interface. However, most lenses have at least one surface that is curved. For a curved surface the angle of incidence is a function of the origin of the rays and the normal to the surface at the point of incidence. The equations for curved surfaces can be derived in a similar fashion as the equations for planar surfaces by taking into account the curvature. As shown in Fig. 5.15, consider a ray incident from an on-axis point at an angle θ_i towards a curved surface with radius R . Let the distance of the on-axis point from the surface be f and the angle subtended by the normal to the surface at the point of incidence be normal be θ_R . The situation for a convex and a concave surface are shown in Fig. 5.15(a) and (b) respectively.

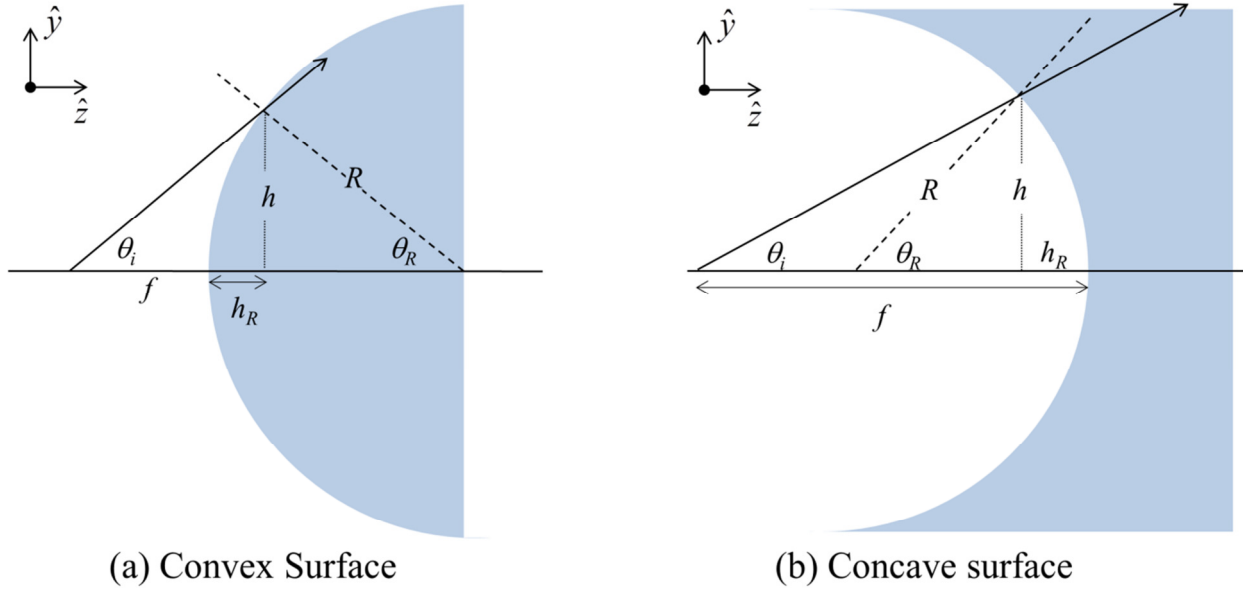


Fig. 5.15 Schematic of convex and concave spherical surfaces: The source is considered to be on-axis at a distance f from the surface. The angle of incidence at the surface is $\theta_i + \theta_R$ for the convex surface and $|\theta_i - \theta_R|$ for the concave surface. The normal from the point of incidence to the optical axis has a height of h and the distance between the surface and the normal is h_R .

It is clear from the above schematic that when the radius of curvature and the distance of the source from the surface are comparable, the curvature of the surface cannot be neglected anymore and the thin lens approximation fails. The angle of incidence at the convex (concave) surface is given by $\theta_i + \theta_R$ ($|\theta_i - \theta_R|$). In order to find θ_R given f and R , a normal to the optical axis, h , is drawn from the point of incidence. Let the distance from the normal to the surface along the optical axis be h_R . We will derive the equations for the convex case and then apply the results for the concave case. Using simple trigonometry we have, for the convex case

$$\tan(\theta_i) = \frac{h}{f + h_R} \tag{5.31}$$

The distance h_R can be written in terms of the R and h as $h_R = R - \sqrt{R^2 - h^2}$. Substituting in eq. and with some algebraic manipulation, we can obtain a quadratic equation in h as

$$h^2 \operatorname{cosec}^2(\theta_i) - 2(f + R) \cot(\theta_i) h + (f^2 + 2Rf) = 0 \tag{5.32}$$

One of the factors important for calculating the properties of the curved surface is the ratio of the radius of the lens surface (R) to the distance between the surface and the on-axis object point (f), which we call α . Dividing eq. by R , we get

$$\frac{h^2}{R^2} \operatorname{cosec}^2(\theta_i) - 2(\alpha + 1) \cot(\theta_i) \frac{h}{R} + (\alpha^2 + 2\alpha) = 0 \quad (5.33)$$

Therefore, we now have a quadratic equation in (h/R) which is also the sine of angle θ_R .

The two solutions for the above equation are given by

$$\frac{h}{R} \pm = \sin(\theta_i) \left((1 + \alpha) \cos(\theta_i) \pm \sqrt{1 - \sin^2(\theta_i)(1 + \alpha)^2} \right) \quad (5.34)$$

It is clear from Fig. 5.15 that if the incident ray does not miss the convex surface, it will intersect the surface at two different points. It can be shown that the first intersection point is given by the (-) solution in the above equation. Thus angle θ_R is given by

$$\theta_R^{\text{convex}} = \sin^{-1} \left(\sin(\theta_i) \left((1 + \alpha) \cos(\theta_i) - \sqrt{1 - \sin^2(\theta_i)(1 + \alpha)^2} \right) \right) \quad (5.35)$$

By using a similar procedure for the concave case, it can be shown that

$$\theta_R^{\text{concave}} = \sin^{-1} \left(\sin(\theta_i) \left((\alpha - 1) \cos(\theta_i) + \sqrt{1 - \sin^2(\theta_i)(1 - \alpha)^2} \right) \right) \quad (5.36)$$

In order to simplify notation, the curvature angle for the two surfaces can be written as

$$\theta_R^\pm = \sin^{-1} \left(\sin(\theta_i) \left((\alpha \pm 1) \cos(\theta_i) + \sqrt{1 - \sin^2(\theta_i)(1 \pm \alpha)^2} \right) \right) \quad (5.37)$$

Where + denotes the convex surface and - denotes the concave surface. Thus the angle of incidence at the two surfaces can be written as $\theta_{CS} = |\theta_i \pm \theta_R^\pm|$. It should be noted that the angle θ_R is real if the discriminant is non-negative, i.e. $1 - \sin^2(\theta_i)(1 + \alpha)^2 \geq 0$ for the convex case and $1 - \sin^2(\theta_i)(1 - \alpha)^2 \geq 0$ for the concave case. This implies that, for a given α , there is a maximum allowable incidence angle that does not miss the curved surface. Thus, for a given convex surface, α is related to the numerical aperture of the surface. An important assumption

here is that the surfaces are not limited by an external aperture in which case the angle of incidence will depend on the aperture size. From the above equation, the maximum allowable angle for the two cases are given by

$$\max(\theta_i^\pm) = \sin^{-1}\left(\frac{1}{|1 \pm \alpha|}\right) \quad (5.38)$$

The solutions of the above equations are graphically depicted in Fig. 5.16. The increasing value of α is equivalent to either the source moving away from the surface and/or a decrease in radius of curvature R . As expected, for the convex case, as alpha increases, the maximum allowable angle decreases continuously. However, for the concave case, the maximum allowable angle only starts to decrease after alpha ≥ 2 . This implies that for a source closer to the surface, the concave surface can accept steeper angles of incidence than the convex surface.

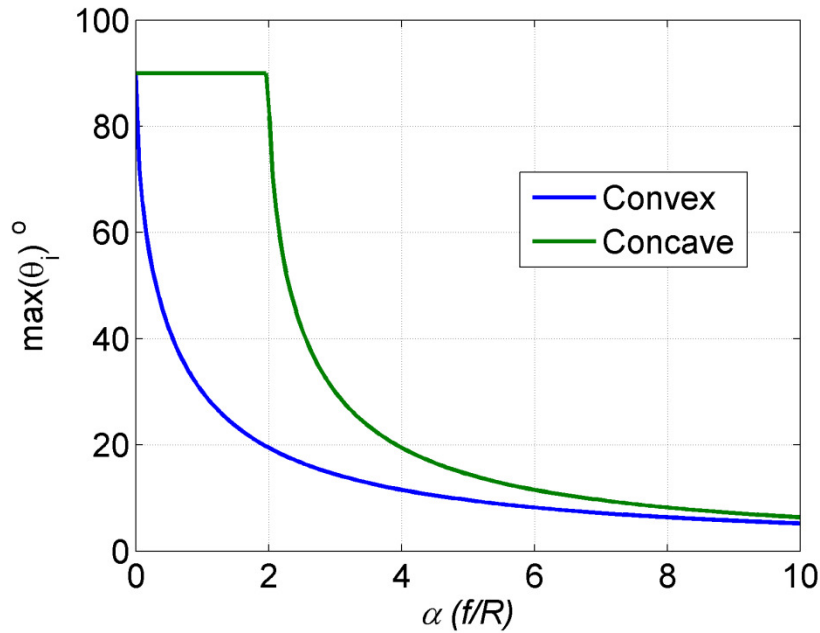


Fig. 5.16 Maximum allowable incidence angle θ_i that is refracted as a function of parameter α for the convex (blue) and the concave (green) case .

Using the equations developed above, we can compare the phase refraction angles for an ideal PLRM and the o-wave and the eo-wave of the uniaxial material. By the definition of

PLRM, the phase refraction angle is proportional to the angle of incidence. Thus the phase refraction angle for the convex and concave case is given by $|\theta_i \pm \theta_R^\pm|/K$. However, in the case of a uniaxial material, the refractive index seen by the eo-wave is a function of the angle subtended by refracted wave on the c -axis of the crystal. In order to ensure that every cone of rays emanating at an angle observe the same effective refractive index, the c -axis was chosen to lie along the optical axis. The angle between the c -axis and the surface curvature is also given by θ_R . Denoting the phase refraction angle by θ_e and using eq. (5.30), the generalized Snell's law at the interface of the convex surface can be written as

$$\sin(\theta_i + \theta_R^+) = \frac{n_o n_e}{\sqrt{n_o^2 \sin^2(\theta_e - \theta_R^+) + n_e^2 \cos^2(\theta_e - \theta_R^+)}} \sin(\theta_e) \quad (5.39)$$

Thus, the phase refraction angle can be calculated by solving the above transcendental equation. Since for the convex case, the c -axis lies on the same side of the surface normal as the refracted angle, the angle between the c -axis and refracted angle can be calculated as $|\theta_e - \theta_R|$. The absolute function can be dropped since these angles appear in squares of trigonometric functions. In case of the concave surface, the transcendental equation can be written as

$$\sin(|\theta_i - \theta_R^-|) = \begin{cases} \frac{n_o n_e}{\sqrt{n_o^2 \sin^2(\theta_e - \theta_R^-) + n_e^2 \cos^2(\theta_e - \theta_R^-)}} \sin(\theta_e), & \alpha > 1 \\ \frac{n_o n_e}{\sqrt{n_o^2 \sin^2(\theta_e + \theta_R^-) + n_e^2 \cos^2(\theta_e + \theta_R^-)}} \sin(\theta_e), & \alpha < 1 \end{cases} \quad (5.40)$$

When $\alpha=1$, the source lies on the center of curvature and angle of incidence $|\theta_i - \theta_R|=0$ and thus the refracted angle is $|\theta_e - \theta_R|=0$. However, depending on whether the source lies to the left or right of the center of curvature, the c -axis lies on the same or opposite side of the phase-refracted angle respectively. This is taken into account by applying the appropriate sign in eq.

(5.40). The phase-refraction angle for the ordinary wave is calculated using the ordinary refractive index in Snell's law.

For a typical thin lens, the focal length of a single surface is given by $R = (n-1)f$, thus for a typical glass lens, $\alpha \approx 0.5$. However for completeness we also consider two other extremes where $\alpha = 0.1$ and $\alpha = 5$. The resultant phase refraction angles are shown in Fig. 5.17. As before, we consider two uniaxial materials with $n_o=1.2$, $n_e=1.08$ (top row) and $n_o=1.5$, $n_e=1.2$ (bottom row). The black and blue curves represent the convex and concave surfaces respectively. The dots (.) represent the phase refraction angle of an ideal PLRM; whereas the solid (-) and the dashed (--) lines represent the refraction angles of the eo-wave and o-wave of the negative uniaxial material.

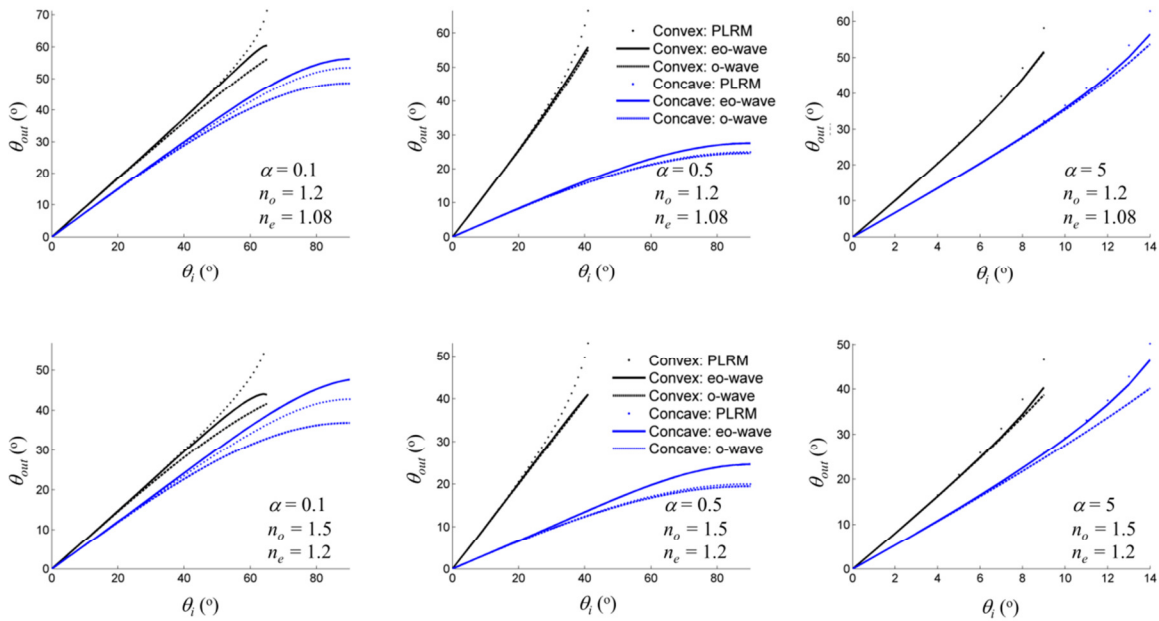


Fig. 5.17 Linear refraction performance at a spherical interface with a birefringent material. The c-axis is along the propagation direction both convex (black) and concave (blue) curved surfaces are considered. Three different ratios of source distance to the radius of the lens $\alpha = 0.1$, 0.5 and 5 (left to right) are shown. The uniaxial materials considered are $n_o=1.2$, $n_e=1.08$ (top row) and $n_o=1.5$, $n_e=1.2$ (bottom row). The dots (.) represent ideal PLRM, the solid (-) lines represent the eo-wave phase vector direction for the uniaxial material and the dashed (--) lines represent the o-wave phase vector direction.

It is clear from eq. (5.40), that the relationship between the output refraction angles with α and o- and eo- refractive indices of a uniaxial material is a complicated one. However, for all the cases considered, it is clear that the eo-wave of the uniaxial material follows the ideal PLRM much more closely than an isotropic material. These calculations show that, even with curved surfaces, a uniaxial material is a strong candidate for IRAM.

APPENDIX 5C CALCITE AS AN IRAM

One of the most common anisotropic materials used in optics is Calcite owing to its transparency, large birefringence and its ubiquitousness. In this section, we explore the properties of calcite as an IRAM, specifically as a PLRM. The ordinary and extra-ordinary refractive indices for calcite are $n_o=1.58$ and $n_e=1.486$ [145]. As shown in Fig. 5.18, performance of flat interface of calcite with c -axis perpendicular to the interface is compared to an ideal PLRM. The linearity constant for the ideal PLRM is chosen to be equal to the ordinary index of calcite. The effective index curves in Fig. 5.18 (a) show that although the eo-ray of calcite follows PLRM more closely than the o-ray, the overlap is not as significant as the arbitrary birefringent materials chosen in the chapter. Fig. 5.18 (b) shows the phase-refraction and Poynting vector angles as functions of incidence angles confirming the results shown by the effective index curves.

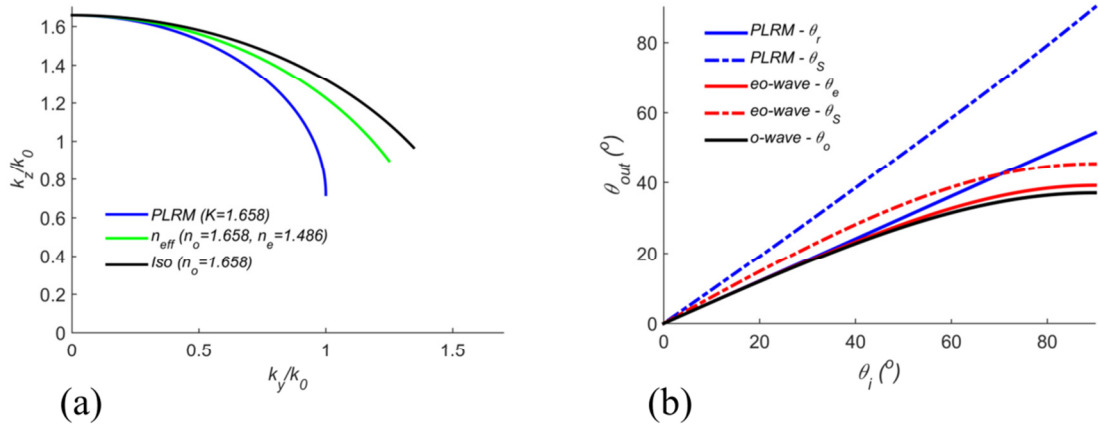


Fig. 5.18 PLRM vs. calcite (Flat interface): (a) Comparison of the effective index curve for an ideal PLRM (solid blue) with effective index of the eo-wave (green) and o-wave (black) of calcite. The ordinary and extra-ordinary refractive indices of calcite are $n_o=1.658$ and $n_e=1.486$. The linearity constant considered for PLRM is $K=1.658$ (blue) (b) The phase refraction angles (solid) and Poynting vector angles (dashed) for an ideal PLRM (blue), o-ray (black) and eo-ray (red) for calcite.

Next we compare the properties of curved calcite surfaces with c-axis along the optical axis. The equations for curved surfaces were developed in Appendix 5b. The parameter α represents the ratio of the source distance to the radius of curvature and also defines the maximum incidence angles that do not miss the curved surface. Three different values of α (0.1, 0.5 and 5) were chosen as shown in Fig. 5.19. Curved surfaces naturally help maintain the linearity between incidence and phase-refracted angles. However, the eo-ray of calcite does show a greater overlap than the o-ray.

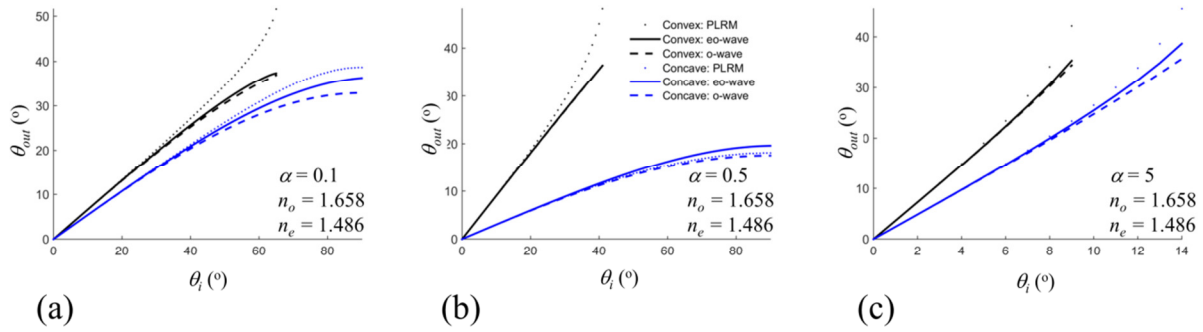


Fig. 5.19 Linear refraction performance at a spherical interface with calcite. The c -axis is along the propagation direction for both convex (black) and concave (blue) curved surfaces. Three different ratios of source distance to the curvature of the surface, $\alpha = 0.1, 0.5$ and 5 (left to right) are shown. The dots (.) represent ideal PLRM, the solid (-) lines represent the eo-wave phase vector direction for calcite and the dashed (--) lines represent the o-wave phase vector direction.

Finally, a singlet calcite lens is simulated in Zemax and the performance is compared with a standard single and a doublet lens. The object is at infinity and the image is formed at a distance of about 100mm from the lens. The lens diameter is 40mm, making it an $f/2.5$ lens. To compare the performance over a large field of view, the image heights are assumed to be at focus, at 15 mm and, at 30 mm from the optical axis. In order to achieve best performance for each lens, the radii of curvature of the lens were optimized using the local optimization algorithm in Zemax. The wavefront is optimized for the on-axis image point. The table below shows the relative spot size for the different lenses for three different image heights. It can be seen that at focus, the birefringent lens has a smaller spot size than the singlet lens but larger than the doublet. As the image height increases, the spot size of the birefringent lens gets smaller compared to that of the singlet and doublet lenses.

Spherical lens type	c -axis	spot size at 0mm	spot size at 15mm	spot size at 30mm
Singlet lens	-	15 μm	228 μm	913 μm
Doublet lens	-	3.4 μm	243 μm	942 μm
Birefringent lens	z	9.5 μm	207 μm	821 μm

Table 5.2 Comparison of R.M.S. spot size of conventional singlet, doublet and a birefringent lens made of calcite.

It is clear that calcite has favorable properties for emulating an IRAM. However, the large space of form-birefringent material presents with a degree of freedom to control the amount of birefringence making them stronger candidates for realization of IRAM.

APPENDIX 5D IRAM IMPLEMENTATION USING CHIRAL MATERIALS

In our previous discussions we saw that anisotropy provides a degree of freedom that can be exploited to tune the k -surface of the anisotropic material to satisfy or approximate the IRAM condition. Similarly, the chirality of a material provides an additional degree of freedom to specify the elements of the permittivity tensor. In this section we explore chiral materials as potential candidates for realizing the IRAM condition. By definition chirality implies non-superimposable mirror images of the material substructure[147]. The eigen-polarizations of an isotropic chiral material are the right hand circular (RHC) and left hand circular (LHC) polarization states[148]. This implies that an input linear polarization can be decomposed in its orthogonal circular polarizations where the phase difference between LHC and RHC causes rotation of the linear polarization. This phenomena associated with chiral media is known as optical activity[147].

An isotropic chiral material is also known as a bi-isotropic medium. A more general linear medium, however, is the bi-anisotropic medium whose constitutive parameters are

uniaxial dyadic. In what follows, we will explore the BI and uniaxial bi-anisotropic medium as possible candidates for IRAM. In each case, the interface between air and the chiral medium is considered to be flat.

Bi-Isotropic material

A bi-isotropic material is an isotropic chiral medium with no preferred direction for the chirality. The constitutive parameters for such a medium are scalars. It can be show that, for a non-magnetic bi-isotropic material, the effective refractive index of the material is given by[148]–[151]

$$n_{\pm} = n(1 \pm \kappa) \quad (5.41)$$

Where n represents the refractive index of the host-medium, κ is the chirality constant and \pm represent the two eigen-polarizations. Clearly, a BI medium is an isotropic medium with two different refractive indices for the two eigen-polarizations. Thus, a BI medium does not provide any additional degree of freedom for IRAM approximation.

Bi-anisotropic medium

A bi-anisotropic medium can be realized, for example, by randomly distributing metal helices[148] in a host medium where the axes of the helical insertions can either be parallel to the z -axis or perpendicular to the z -axis with random orientations in the transverse plane. For simplicity we assume that the medium under consideration is only axially bi-anisotropic, i.e. the axes of the helical inclusions are along the z -axis. The constitutive relationship for a lossless, reciprocal and axially bi-anisotropic chiral medium can be written as[148]

$$\begin{aligned} \bar{D} &= \left[\varepsilon_t \bar{I}_t + \varepsilon_z \hat{z}\hat{z} \right] \cdot \bar{E} + i\kappa \sqrt{\varepsilon_0 \mu_0} \hat{z}\hat{z} \cdot \bar{H} \\ \bar{B} &= \left[\mu_t \bar{I}_t + \mu_z \hat{z}\hat{z} \right] \cdot \bar{H} - i\kappa \sqrt{\varepsilon_0 \mu_0} \hat{z}\hat{z} \cdot \bar{E} \end{aligned} \quad (5.42)$$

where ε_t , ε_z , μ_t , and μ_z are the transverse and axial permittivities and permeabilities and κ is the transverse chirality. It can be shown that at the interface of the uniaxial bi-anisotropic

medium, the relationship between the incident and the phase refraction angle is given by[148], [152], [153]

$$\sin \theta_i^\pm = \frac{n_o \sin \theta_r^\pm}{\sqrt{\cos^2 \theta_r^\pm + \sin^2 \theta_r^\pm / \rho_\pm}} \quad (5.43)$$

where, θ_i and θ_r are the incident and phase-refracted angles respectively and $n_o(\sqrt{\epsilon_t})$ and $n_e(\sqrt{\epsilon_z})$ represent the ordinary and extra-ordinary refractive indices respectively. Here, \pm represent the two eigen modes and the term ρ_\pm is known as the self-dual parameter that depends on the axial impedance (and hence admittance) of the material and aids in finding the two plane eigen-wave solutions of the bi-anisotropic medium. The proof of the above equation can be found in Chapter 8 of reference [148]. The above equation is the generalized Snell's law for a bi-anisotropic medium. The non-linearity arises due to the fact that the effective refractive index for the extra-ordinary ray of a uniaxial material is a non-linear function of the sine of refraction angle. The expression for the self-dual parameter in a non-magnetic media ($\mu_t, \mu_z=1$) is given by[148], [152], [153]

$$\rho_\pm = \frac{1}{2} \left[\frac{n_e^2}{n_o^2} + 1 \pm \sqrt{\left(\frac{n_e^2}{n_o^2} - 1 \right)^2 + \frac{4\kappa^2}{n_o^2}} \right] \quad (5.44)$$

For an achiral uniaxial material, eq. (5.43) reduces to the well-known cases of the uniaxial material. By substituting $\kappa=0$ in eq. (5.44) we get, for the two eigen modes, $\rho_+ = n_e^2/n_o^2$ and $\rho_-=1$. Substituting back in equation (5.43), we get

$$\sin \theta_i^+ = \frac{\sin \theta_r^+}{\sqrt{\cos^2 \theta_r^+ / n_o^2 + \sin^2 \theta_r^+ / n_e^2}} = n_{\text{eff}}(\theta_r^+) \sin \theta_r^+ \quad (5.45)$$

$$\sin \theta_i^- = n_o \sin \theta_r^- \quad (5.46)$$

As expected, the two eigen modes represent the extra-ordinary and ordinary rays and Snell's law for the two are consistent with that of a uniaxial material with c-axis along the axial

direction. Also, for an isotropic medium this relationship reduces to the linear Snell's law and the two eigen modes collapse into a single sphere.

Here we analyze a more general case of anisotropic chiral medium. The phase-refraction angle for this medium is shown as a function of the incidence angle in Fig. 5.20. Note that only the mode that approximates IRAM well is shown in the figure. The other mode deviates from an ideal IRAM with increasing chirality. Similar to the case of the achiral uniaxial medium, we consider two different host mediums for a bi-anisotropic material. The o- and eo- refractive indices for the first host medium (Fig. 5.20 (a)) are $n_o=1.2$ and $n_e=1.15$ and for the second host medium are $n_o=1.5$ and $n_e=1.25$ (Fig. 5.20 (b)). Slightly higher values of the eo-index are chosen to demonstrate the effect of increasing chirality. For completeness we also include the curve for the isotropic case where the refractive index is equal to n_o . Interestingly, the phase-refraction angle tends faster towards the ideal IRAM with increasing chirality. However, a similar effect can be observed by tuning the eo-refractive index n_e . This can be shown by equating the parameter ρ_+ for a uniaxial media with that of a bi-anisotropic media keeping the ordinary index n_o same, i.e.

$$\frac{n'_e}{n_o} = \sqrt{\frac{1}{2} \left[\frac{n_e^2}{n_o^2} + 1 + \sqrt{\left(\frac{n_e^2}{n_o^2} - 1 \right)^2 + \frac{4\kappa^2}{n_o^2}} \right]} \quad (5.47)$$

This can be further simplified to,

$$n'_e = \sqrt{\frac{n_e^2 + n_o^2 + \sqrt{(n_e^2 - n_o^2)^2 + 4\kappa^2 n_o^2}}{2}} \quad (5.48)$$

Therefore, the improvement seen by using a bi-anisotropic medium can be achieved by increasing the birefringence of a uniaxial material. Nevertheless, chirality can be utilized in conjunction with the birefringence to fine tune the effective anisotropy of the material to approximate IRAM behavior.

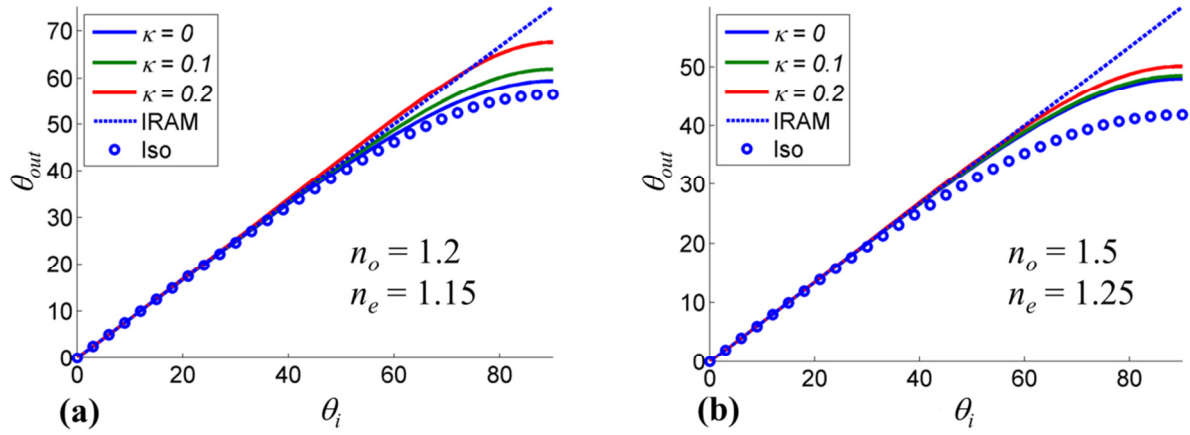


Fig. 5.20 Linear refraction performance at a planar interface with a uniaxial bi-anisotropic material: Phase-refraction angle as a function of angle of incidence with increasing chirality for (a) $n_o=1.2$, $n_e=1.15$ and (b) $n_o=1.5$, $n_e=1.25$.

Chapter 6 Conclusion and Outlook

The aim of this work was to demonstrate the power of electromagnetic approaches in modern computational optical imaging systems. It was shown that by jointly optimizing the electromagnetic optical elements of a computational imaging system, it is possible to improve upon the current techniques used for far-field and near-field super-resolution microscopy and in minimizing aberrations. The commonly used scalar model of optics was extended to include effects of polarization sensitive sources and systems with the help of the more rigorous electromagnetic optics approach.

It was concluded that if the anisotropic nature of emission from fixed dipole emitters is ignored, systematic errors are introduced in super-resolution microscopy leading to localization errors of up to 100s of nanometers. The dipole was therefore modeled using a complete vectorial approach to account for the asymmetric emission patterns. The Green's tensor response of the dipole input was engineered by addition of polarization optics and phase modulating elements. The *CRLB* was used as a metric to measure the performance of engineered systems and it was concluded that polarization based systems that use the double-helix or the vortex phase mask are attractive candidates for the 5D imaging of dipoles. These systems typically show a threefold improvement in dipole localization and a fourfold improvement in orientation estimation over the commonly used polarization insensitive standard systems. In order to facilitate efficient information transfer, the phase modulating elements were fabricated on a quartz substrate using the binary multi-level exposure method. The diffraction efficiency of a 16-level mask is around 99% and for mask fabricated on the quartz substrate a transmission efficiency of ~90% was observed. Thus, phase masks used as diffractive optical elements are extremely promising for efficiently engineering the Green's tensor in the photon-limited environment of single molecule

imaging. Experimental validation of improvement in estimation parameters using the polarization sensitive DHPSF was also demonstrated. By correcting each localization based on an estimated orientation, an improvement in standard deviations in lateral localization from $\sim 2\times$ worse than photon-limited precision (48 nm vs. 25 nm) to within 5 nm of photon-limited precision is observed. This research has opened up a myriad of new possibilities for engineering the response of Green's tensor response to efficiently extract the dipole localization and orientation parameters leading to 5D super-resolution microscopy in the far-field.

In the near-field, however, the super-lensing effect of negative refractive index metamaterials has become prevalent in the past decade. Aperiodic metamaterial structures that give rise to strong magnetic resonance to realize negative refractive index in metamaterials were analyzed. These aperiodic structures were shown to have stronger a magnetic resonance than their periodic counterparts but were found to be more sensitive to fabrication errors. Nevertheless, aperiodic metamaterials provide an alternative approach to NIM design by relaxing the periodicity requirements.

Apart from the fundamental limit imposed by the diffraction limit, the resolution of imaging systems suffers due to aberrations introduced by the assumption of linearity between the incident and refracted angle in the small angle approximation. A new class of artificial materials termed as infinitely refraction-linear artificial material (IRAM) whose properties are designed to match the linear relationship for large incident angles was proposed. The first-order approximation of IRAMs was provided by using negative uniaxial materials. Simulations of IRAM lenses in Zemax show a 200% improvement in spot size for on-axis imaging and about 30% improvement for large field of views over conventional lenses. IRAMs also have the

potential to reduce complex multi-element lens structures to simple single element lenses reducing the need to optimize over a multitude of parameters.

Thus, it was shown that computational optical imaging has played an important role in achieving nanometer accuracies in super-resolution microscopy and in the design and simulation of artificial materials for imaging, etc. It was demonstrated that electromagnetic optics is an important tool that should be utilized whilst studying this modern paradigm of imaging to avoid inaccuracies and extend its applicability.

Bibliography

- [1] A. Ashok and M. A. Neifeld, "Pseudorandom phase masks for superresolution imaging from subpixel shifting," *Appl. Opt.*, vol. 46, no. 12, p. 2256, 2007.
- [2] G. Häusler, "A method to increase the depth of focus by two step image processing," *Opt. Commun.*, vol. 6, no. 1, pp. 38–42, Sep. 1972.
- [3] K. J. Barnard, "High-resolution image reconstruction from a sequence of rotated and translated frames and its application to an infrared imaging system," *Opt. Eng.*, vol. 37, no. 1, p. 247, Jan. 1998.
- [4] E. Ben-Eliezer, E. Marom, N. Konforti, and Z. Zalevsky, "Radial mask for imaging systems that exhibit high resolution and extended depths of field," *Appl. Opt.*, vol. 45, no. 9, p. 2001, 2006.
- [5] W. T. Cathey, B. R. Frieden, W. T. Rhodes, and C. K. Rushforth, "Image gathering and processing for enhanced resolution," *J. Opt. Soc. Am. A*, vol. 1, no. 3, p. 241, Mar. 1984.
- [6] K. Kubala, E. Dowski, and W. Cathey, "Reducing complexity in computational imaging systems," *Opt. Express*, vol. 11, no. 18, p. 2102, Sep. 2003.
- [7] M. G. L. Gustafsson, "Surpassing the lateral resolution limit by a factor of two using structured illumination microscopy. SHORT COMMUNICATION," *J. Microsc.*, vol. 198, no. 2, pp. 82–87, May 2000.
- [8] B. Bailey, D. L. Farkas, D. L. Taylor, and F. Lanni, "Enhancement of axial resolution in fluorescence microscopy by standing-wave excitation.," *Nature*, vol. 366, no. 6450, pp. 44–8, Nov. 1993.
- [9] L. Novotny and B. Hecht, *Principles of Nano-Optics*. Cambridge University Press, 2006, p. 558.
- [10] D. J. Brady, *Optical Imaging and Spectroscopy*. Wiley-OSA; 1 edition, 2009, p. 510.
- [11] W. S. Boyle and G. E. Smith, "Charge Coupled Semiconductor Devices," *Bell Syst. Tech. J.*, vol. 49, no. 4, pp. 587–593, Apr. 1970.
- [12] E. Abbe, "Beiträge zur Theorie des Mikroskops und der mikroskopischen Wahrnehmung," *Arch. für Mikroskopische Anat.*, vol. 9, no. 1, pp. 413–418, Dec. 1873.
- [13] Rayleigh, "XV. On the theory of optical images, with special reference to the microscope," *Philos. Mag. Ser. 5*, vol. 42, no. 255, pp. 167–195, Aug. 1896.
- [14] W. E. Moerner, "Microscopy beyond the diffraction limit using actively controlled single molecules.," *J. Microsc.*, vol. 246, no. 3, pp. 213–20, Jun. 2012.

- [15] S. W. Hell, “Microscopy and its focal switch.,” *Nat. Methods*, vol. 6, no. 1, pp. 24–32, Jan. 2009.
- [16] E. Betzig, G. H. Patterson, R. Sougrat, O. W. Lindwasser, S. Olenych, J. S. Bonifacino, M. W. Davidson, J. Lippincott-Schwartz, and H. F. Hess, “Imaging intracellular fluorescent proteins at nanometer resolution.,” *Science*, vol. 313, no. 5793, pp. 1642–5, Sep. 2006.
- [17] S. T. Hess, T. P. K. Girirajan, and M. D. Mason, “Ultra-high resolution imaging by fluorescence photoactivation localization microscopy.,” *Biophys. J.*, vol. 91, no. 11, pp. 4258–72, Dec. 2006.
- [18] M. J. Rust, M. Bates, and X. Zhuang, “Sub-diffraction-limit imaging by stochastic optical reconstruction microscopy (STORM).,” *Nat. Methods*, vol. 3, no. 10, pp. 793–5, Oct. 2006.
- [19] A. Sharonov and R. M. Hochstrasser, “Wide-field subdiffraction imaging by accumulated binding of diffusing probes.,” *Proc. Natl. Acad. Sci. U. S. A.*, vol. 103, no. 50, pp. 18911–6, Dec. 2006.
- [20] T. Ha, T. Enderle, S. Chemla, R. Selvin, and S. Weiss, “Single Molecule Dynamics Studied by Polarization Modulation.,” *Phys. Rev. Lett.*, vol. 77, no. 19, pp. 3979–3982, Nov. 1996.
- [21] F. Aieta, P. Genevet, M. A. Kats, N. Yu, R. Blanchard, Z. Gaburro, and F. Capasso, “Aberration-free ultrathin flat lenses and axicons at telecom wavelengths based on plasmonic metasurfaces.,” *Nano Lett.*, vol. 12, no. 9, pp. 4932–6, Sep. 2012.
- [22] J. Chen, C. Radu, and A. Puri, “Aberration-free negative-refractive-index lens,” *Appl. Phys. Lett.*, vol. 88, no. 7, p. 071119, Feb. 2006.
- [23] S. A. Cummer, “Simulated causal subwavelength focusing by a negative refractive index slab,” *Appl. Phys. Lett.*, vol. 82, no. 10, p. 1503, Mar. 2003.
- [24] A. Lakhtakia, “On Perfect Lenses and Nihilism,” p. 5, Dec. 2001.
- [25] R. Merlin, “Analytical solution of the almost-perfect-lens problem,” *Appl. Phys. Lett.*, vol. 84, no. 8, p. 1290, Feb. 2004.
- [26] C. G. Parazzoli, R. B. Greegor, J. A. Nielsen, M. A. Thompson, K. Li, A. M. Vetter, M. H. Tanielian, and D. C. Vier, “Performance of a negative index of refraction lens,” *Appl. Phys. Lett.*, vol. 84, no. 17, p. 3232, Apr. 2004.
- [27] B. Huang, W. Wang, M. Bates, and X. Zhuang, “Three-dimensional super-resolution imaging by stochastic optical reconstruction microscopy.,” *Science*, vol. 319, no. 5864, pp. 810–3, Feb. 2008.

- [28] H. P. Kao and A. S. Verkman, "Tracking of single fluorescent particles in three dimensions: use of cylindrical optics to encode particle position.," *Biophys. J.*, vol. 67, no. 3, pp. 1291–300, Sep. 1994.
- [29] A. Greengard, Y. Y. Schechner, and R. Piestun, "Depth from diffracted rotation," *Opt. Lett.*, vol. 31, no. 2, p. 181, Jan. 2006.
- [30] S. R. P. Pavani and R. Piestun, "High-efficiency rotating point spread functions," *Opt. Express*, vol. 16, no. 5, p. 3484, Mar. 2008.
- [31] S. Ghosh, S. A. Quirin, G. Grover, R. Piestun, and C. Preza, "Double helix PSF engineering for computational fluorescence microscopy imaging," in *SPIE BiOS*, 2012, p. 82270F–82270F–7.
- [32] E. R. Dowski and W. T. Cathey, "Extended depth of field through wave-front coding.," *Appl. Opt.*, vol. 34, no. 11, pp. 1859–66, Apr. 1995.
- [33] J. Enderlein, E. Toprak, and P. R. Selvin, "Polarization effect on position accuracy of fluorophore localization," *Opt. Express*, vol. 14, no. 18, p. 8111, Sep. 2006.
- [34] J. Engelhardt, J. Keller, P. Hoyer, M. Reuss, T. Staudt, and S. W. Hell, "Molecular orientation affects localization accuracy in superresolution far-field fluorescence microscopy.," *Nano Lett.*, vol. 11, no. 1, pp. 209–13, Jan. 2011.
- [35] W. E. Moerner, "New directions in single-molecule imaging and analysis.," *Proc. Natl. Acad. Sci. U. S. A.*, vol. 104, no. 31, pp. 12596–602, Jul. 2007.
- [36] E. Toprak and P. R. Selvin, "New fluorescent tools for watching nanometer-scale conformational changes of single molecules.," *Annu. Rev. Biophys. Biomol. Struct.*, vol. 36, pp. 349–69, Jan. 2007.
- [37] S. R. P. Pavani, M. A. Thompson, J. S. Biteen, S. J. Lord, N. Liu, R. J. Twieg, R. Piestun, W. E. Moerner, S. Rama, and P. Pavani, "Three-dimensional, single-molecule fluorescence imaging beyond the diffraction limit by using a double-helix point spread function.," *Proc. Natl. Acad. Sci. U. S. A.*, vol. 106, no. 9, pp. 2995–9, Mar. 2009.
- [38] M. Böhmer, J. Enderlein, and M. Bo, "Orientation imaging of single molecules by wide-field epifluorescence microscopy," *J. Opt. Soc. Am. B*, vol. 20, no. 3, p. 554, Mar. 2003.
- [39] K. I. Mortensen, L. S. Churchman, J. A. Spudich, and H. Flyvbjerg, "Optimized localization analysis for single-molecule tracking and super-resolution microscopy.," *Nat. Methods*, vol. 7, no. 5, pp. 377–81, May 2010.
- [40] M. A. Lieb, J. M. Zavislan, and L. Novotny, "Single-molecule orientations determined by direct emission pattern imaging," *J. Opt. Soc. Am. B*, vol. 21, no. 6, p. 1210, Jun. 2004.

- [41] M. R. Foreman, C. M. Romero, and P. Török, “Determination of the three-dimensional orientation of single molecules,” *Opt. Lett.*, vol. 33, no. 9, p. 1020, Apr. 2008.
- [42] A. Agrawal, S. Quirin, G. Grover, and R. Piestun, “Limits of 3D Dipole Localization and Orientation Estimation with Application to Single-Molecule Imaging - OSA Technical Digest (CD),” in *Computational Optical Sensing and Imaging*, 2011, p. CWA4.
- [43] A. Agrawal, S. Quirin, G. Grover, and R. Piestun, “Limits of 3D dipole localization and orientation estimation for single-molecule imaging: towards Green’s tensor engineering,” *Opt. Express*, vol. 20, no. 24, pp. 26667–26680, Nov. 2012.
- [44] M. Backlund, M. D. Lew, A. S. Backer, S. J. Sahl, G. Grover, A. Agrawal, R. Piestun, and W. E. Moerner, “The Double-Helix Microscope Enables Precise and Accurate Measurement of 3D Single-Molecule Orientation and Localization Beyond the Diffraction Limit,” in *Optics in the Life Sciences*, 2013, p. NM2B.2.
- [45] M. P. Backlund, M. D. Lew, A. S. Backer, S. J. Sahl, G. Grover, A. Agrawal, R. Piestun, and W. E. Moerner, “Simultaneous, accurate measurement of the 3D position and orientation of single molecules,” *Proc. Natl. Acad. Sci. U. S. A.*, vol. 109, no. 47, pp. 19087–92, Nov. 2012.
- [46] M. P. Backlund, M. D. Lew, A. S. Backer, S. J. Sahl, G. Grover, A. Agrawal, R. Piestun, and W. E. Moerner, “The double-helix point spread function enables precise and accurate measurement of 3D single-molecule localization and orientation,” in *SPIE BiOS*, 2013, p. 85900L–85900L–11.
- [47] M. D. Lew, M. P. Backlund, A. S. Backer, S. J. Sahl, G. Grover, A. Agrawal, R. Piestun, and W. E. Moerner, “Measuring the 3D Position and Orientation of Single Molecules Simultaneously and Accurately with the Double Helix Microscope,” in *CLEO: 2013*, 2013, p. CTu3N.3.
- [48] J. B. Pendry, “Negative Refraction Makes a Perfect Lens,” *Phys. Rev. Lett.*, vol. 85, no. 18, pp. 3966–3969, Oct. 2000.
- [49] V. G. Veselago, “The electrodynamics of substances with simultaneously negative values of ϵ and μ ,” *Physics-Uspokhi*, vol. 10, no. 4, pp. 509–514, Apr. 1968.
- [50] N. Garcia, E. V. Ponizovskaya, and J. Q. Xiao, “Zero permittivity materials: Band gaps at the visible,” *Appl. Phys. Lett.*, vol. 80, no. 7, p. 1120, Feb. 2002.
- [51] B. T. Schwartz and R. Piestun, “Dynamic properties of photonic crystals and their effective refractive index,” *J. Opt. Soc. Am. B*, vol. 22, no. 9, p. 2018, 2005.
- [52] N. Engheta, “Circuits with light at nanoscales: optical nanocircuits inspired by metamaterials,” *Science*, vol. 317, no. 5845, pp. 1698–702, Sep. 2007.

- [53] D. Schurig, J. J. Mock, B. J. Justice, S. A. Cummer, J. B. Pendry, A. F. Starr, and D. R. Smith, "Metamaterial electromagnetic cloak at microwave frequencies.," *Science*, vol. 314, no. 5801, pp. 977–80, Nov. 2006.
- [54] J. H. Lee, J. Blair, V. A. Tamma, Q. Wu, S. J. Rhee, C. J. Summers, and W. Park, "Direct visualization of optical frequency invisibility cloak based on silicon nanorod array," *Opt. Express*, vol. 17, no. 15, p. 12922, Jul. 2009.
- [55] J. Valentine, J. Li, T. Zentgraf, G. Bartal, and X. Zhang, "An optical cloak made of dielectrics.," *Nat. Mater.*, vol. 8, no. 7, pp. 568–71, Jul. 2009.
- [56] L. H. Gabrielli, J. Cardenas, C. B. Poitras, and M. Lipson, "Silicon nanostructure cloak operating at optical frequencies," *Nat. Photonics*, vol. 3, no. 8, pp. 461–463, Jul. 2009.
- [57] T. Ergin, N. Stenger, P. Brenner, J. B. Pendry, and M. Wegener, "Three-dimensional invisibility cloak at optical wavelengths.," *Science*, vol. 328, no. 5976, pp. 337–9, Apr. 2010.
- [58] A. Agrawal, W. Park, and R. Piestun, "Negative permeability with arrays of aperiodic silver nanoclusters," *Appl. Phys. Lett.*, vol. 101, no. 8, p. 083109, May 2012.
- [59] A. Agrawal, W. Park, and R. Piestun, "Negative Permeability Using Arrays of Aperiodic Silver Nanoclusters - OSA Technical Digest (CD)," in *Conference on Lasers and Electro-Optics/International Quantum Electronics Conference*, 2009, p. JThE109.
- [60] V. N. Mahajan, *Optical Imaging and Aberrations: Part I. Ray Geometrical Optics (SPIE Press Monograph Vol. PM45)*. SPIE Publications, 1998, p. 500.
- [61] "Optics & Photonics News - Surface Finishing of Complex Optics." [Online]. Available: http://www.osa-opn.org/home/articles/volume_18/issue_10/departments/optical_engineering/surface_finishing_of_complex_optics/#.UJLrVMWHLhc. [Accessed: 01-Nov-2012].
- [62] V. Nguyen, S. Larouche, N. Landy, J. S. Lee, and D. R. Smith, "Quantitative comparison of gradient index and refractive lenses," *J. Opt. Soc. Am. A*, vol. 29, no. 11, p. 2479, Oct. 2012.
- [63] *Micro-Optics: Elements, Systems And Applications*. CRC Press, 1997, p. 600.
- [64] M. F. Juette, T. J. Gould, M. D. Lessard, M. J. Mlodzianoski, B. S. Nagpure, B. T. Bennett, S. T. Hess, and J. Bewersdorf, "Three-dimensional sub-100 nm resolution fluorescence microscopy of thick samples.," *Nat. Methods*, vol. 5, no. 6, pp. 527–9, Jun. 2008.

- [65] S. Ram, J. Chao, P. Prabhat, E. S. Ward, and R. J. Ober, “A novel approach to determining the three-dimensional location of microscopic objects with applications to 3D particle tracking,” *Processing*, vol. 6443, pp. 0–7, 2007.
- [66] S. R. P. Pavani, J. G. DeLuca, and R. Piestun, “Polarization sensitive, three-dimensional, single-molecule imaging of cells with a double-helix system,” *Opt. Express*, vol. 17, no. 22, p. 19644, Oct. 2009.
- [67] G. Grover, S. Quirin, C. Fiedler, and R. Piestun, “Photon efficient double-helix PSF microscopy with application to 3D photo-activation localization imaging.,” *Biomed. Opt. Express*, vol. 2, no. 11, pp. 3010–20, Nov. 2011.
- [68] G. Grover, S. Rama, P. Pavani, R. Piestun, and S. R. P. Pavani, “Performance limits on three-dimensional particle localization in photon-limited microscopy,” *Opt. Lett.*, vol. 35, no. 19, p. 3306, Sep. 2010.
- [69] F. Aguet, S. Geissbühler, I. Märki, T. Lasser, M. Unser, S. Geissb, and M. Iwan, “Super-resolution orientation estimation and localization of fluorescent dipoles using 3-D steerable filters,” *Opt. Express*, vol. 17, no. 8, p. 6829, Apr. 2009.
- [70] S. Quirin, S. R. P. Pavani, and R. Piestun, “Optimal 3D single-molecule localization for superresolution microscopy with aberrations and engineered point spread functions.,” *Proc. Natl. Acad. Sci. U. S. A.*, vol. 109, no. 3, pp. 675–9, Jan. 2012.
- [71] D. Patra, I. Gregor, and J. Enderlein, “Image Analysis of Defocused Single-Molecule Images for Three-Dimensional Molecule Orientation Studies,” *J. Phys. Chem. A*, vol. 108, no. 33, pp. 6836–6841, Aug. 2004.
- [72] A. P. Bartko and R. M. Dickson, “Imaging Three-Dimensional Single Molecule Orientations,” *J. Phys. Chem. B*, vol. 103, no. 51, pp. 11237–11241, Dec. 1999.
- [73] S. Stallinga and B. Rieger, “Accuracy of the Gaussian Point Spread Function model in 2D localization microscopy,” *Opt. Express*, vol. 18, no. 24, p. 24461, Nov. 2010.
- [74] T. J. Gould, M. S. Gunewardene, M. V. Gudheti, V. V. Verkhusha, S.-R. Yin, J. A. Gosse, and S. T. Hess, “Nanoscale imaging of molecular positions and anisotropies.,” *Nat. Methods*, vol. 5, no. 12, pp. 1027–30, Dec. 2008.
- [75] S. A. Rosenberg, M. E. Quinlan, J. N. Forkey, and Y. E. Goldman, “Rotational motions of macro-molecules by single-molecule fluorescence microscopy.,” *Acc. Chem. Res.*, vol. 38, no. 7, pp. 583–93, Jul. 2005.
- [76] H. Sosa, E. J. Peterman, W. E. Moerner, and L. S. Goldstein, “ADP-induced rocking of the kinesin motor domain revealed by single-molecule fluorescence polarization microscopy.,” *Nat. Struct. Biol.*, vol. 8, no. 6, pp. 540–4, Jun. 2001.

- [77] E. J. Peterman, H. Sosa, L. S. Goldstein, and W. E. Moerner, “Polarized fluorescence microscopy of individual and many kinesin motors bound to axonemal microtubules.,” *Biophys. J.*, vol. 81, no. 5, pp. 2851–63, Nov. 2001.
- [78] E. J. G. Peterman, H. Sosa, and W. E. Moerner, “Single-molecule fluorescence spectroscopy and microscopy of biomolecular motors.,” *Annu. Rev. Phys. Chem.*, vol. 55, pp. 79–96, Jan. 2004.
- [79] B. Sick, B. Hecht, and L. Novotny, “Orientational Imaging of Single Molecules by Annular Illumination,” *Phys. Rev. Lett.*, vol. 85, no. 21, pp. 4482–4485, Nov. 2000.
- [80] E. Toprak, J. Enderlein, S. Syed, S. A. McKinney, R. G. Petschek, T. Ha, Y. E. Goldman, and P. R. Selvin, “Defocused orientation and position imaging (DOPI) of myosin V.,” *Proc. Natl. Acad. Sci. U. S. A.*, vol. 103, no. 17, pp. 6495–9, Apr. 2006.
- [81] M. R. Foreman and P. Török, “Fundamental limits in single-molecule orientation measurements,” *New J. Phys.*, vol. 13, no. 9, p. 093013, Sep. 2011.
- [82] H. H. Barrett, C. Dainty, and D. Lara, “Maximum-likelihood methods in wavefront sensing: stochastic models and likelihood functions,” *J. Opt. Soc. Am. A*, vol. 24, no. 2, p. 391, Feb. 2007.
- [83] M. A. Thompson, M. D. Lew, M. Badieirostami, and W. E. Moerner, “Localizing and tracking single nanoscale emitters in three dimensions with high spatiotemporal resolution using a double-helix point spread function.,” *Nano Lett.*, vol. 10, no. 1, pp. 211–8, Jan. 2010.
- [84] M. Badieirostami, M. D. Lew, M. A. Thompson, and W. E. Moerner, “Three-dimensional localization precision of the double-helix point spread function versus astigmatism and biplane.,” *Appl. Phys. Lett.*, vol. 97, no. 16, p. 161103, Oct. 2010.
- [85] H.-L. D. Lee, S. J. Sahl, M. D. Lew, and W. E. Moerner, “The double-helix microscope super-resolves extended biological structures by localizing single blinking molecules in three dimensions with nanoscale precision.,” *Appl. Phys. Lett.*, vol. 100, no. 15, pp. 153701–1537013, Apr. 2012.
- [86] S. R. P. Pavani, J. G. DeLuca, and R. Piestun, “Polarization Sensitive Three-Dimensional Nanoscopy with a Double-Helix Microscope,” in *Biomedical Optics and 3-D Imaging*, 2010, p. BMD2.
- [87] S. M. Kay, *Fundamentals of Statistical Signal Processing, Volume I: Estimation Theory (v. 1)*. Prentice Hall, 1993, p. 625.
- [88] S. J. Lord, Z. Lu, H. Wang, K. A. Willets, P. J. Schuck, H. D. Lee, S. Y. Nishimura, R. J. Twieg, and W. E. Moerner, “Photophysical properties of acene DCDHF fluorophores:

- long-wavelength single-molecule emitters designed for cellular imaging.,” *J. Phys. Chem. A*, vol. 111, no. 37, pp. 8934–41, Sep. 2007.
- [89] M. P. Backlund, M. D. Lew, A. S. Backer, S. J. Sahl, G. Grover, A. Agrawal, R. Piestun, and W. E. Moerner, “Simultaneous, accurate measurement of the 3D position and orientation of single molecules.,” *Proc. Natl. Acad. Sci. U. S. A.*, vol. 109, no. 47, pp. 19087–92, Nov. 2012.
- [90] S. R. P. Pavani and R. Piestun, “Three dimensional tracking of fluorescent microparticles using a photon-limited double-helix response system,” *Opt. Express*, vol. 16, no. 26, p. 22048, Dec. 2008.
- [91] G. Grover, K. DeLuca, S. Quirin, J. DeLuca, and R. Piestun, “Super-resolution photon-efficient imaging by nanometric double-helix point spread function localization of emitters (SPINDLE).,” *Opt. Express*, vol. 20, no. 24, pp. 26681–95, Nov. 2012.
- [92] T. A. Klar and S. W. Hell, “Subdiffraction resolution in far-field fluorescence microscopy,” *Opt. Lett.*, vol. 24, no. 14, p. 954, Jul. 1999.
- [93] A. Kaplan, N. Friedman, and N. Davidson, “Optimized single-beam dark optical trap,” *J. Opt. Soc. Am. B*, vol. 19, no. 6, p. 1233, Jun. 2002.
- [94] T. Kuga, Y. Torii, N. Shiokawa, T. Hirano, Y. Shimizu, and H. Sasada, “Novel Optical Trap of Atoms with a Doughnut Beam,” *Phys. Rev. Lett.*, vol. 78, no. 25, pp. 4713–4716, Jun. 1997.
- [95] D. W. Zhang and X.-C. Yuan, “Optical doughnut for optical tweezers,” *Opt. Lett.*, vol. 28, no. 9, p. 740, May 2003.
- [96] M. Friese, J. Enger, H. Rubinsztein-Dunlop, and N. Heckenberg, “Optical angular-momentum transfer to trapped absorbing particles,” *Phys. Rev. A*, vol. 54, no. 2, pp. 1593–1596, Aug. 1996.
- [97] H. He, M. Friese, N. Heckenberg, and H. Rubinsztein-Dunlop, “Direct Observation of Transfer of Angular Momentum to Absorptive Particles from a Laser Beam with a Phase Singularity,” *Phys. Rev. Lett.*, vol. 75, no. 5, pp. 826–829, Jul. 1995.
- [98] S. Quirin, “QUANTITATIVE OPTICAL IMAGING AND SENSING BY JOINT DESIGN OF POINT SPREAD FUNCTIONS AND ESTIMATION ALGORITHMS,” *Dissertation*, 2011.
- [99] T. Li, “Super-Resolution using Regularized Orthogonal Matching Pursuit based on compressed sensing theory in the wavelet domain,” in *2009 IEEE International Symposium on Computational Intelligence in Robotics and Automation - (CIRA)*, 2009, pp. 234–239.

- [100] F. Bergeaud and S. Mallat, “Matching pursuit of images,” in *Proceedings., International Conference on Image Processing*, 1995, vol. 1, pp. 53–56.
- [101] A. Small and S. Stahlheber, “Fluorophore localization algorithms for super-resolution microscopy,” *Nat. Methods*, vol. 11, no. 3, pp. 267–79, Feb. 2014.
- [102] L. Zhu, W. Zhang, D. Elnatan, and B. Huang, “Faster STORM using compressed sensing,” *Nat. Methods*, vol. 9, no. 7, pp. 721–723, Apr. 2012.
- [103] A. Barsic, G. Grover, and R. Piestun, “Sparse reconstructions of overlapping three-dimensional point spread functions using overcomplete dictionaries,” Aug. 2013.
- [104] A. Pertsinidis, Y. Zhang, and S. Chu, “Subnanometre single-molecule localization, registration and distance measurements,” *Nature*, vol. 466, no. 7306, pp. 647–51, Jul. 2010.
- [105] M. A. Thompson, J. M. Casolari, M. Badieirostami, P. O. Brown, and W. E. Moerner, “Three-dimensional tracking of single mRNA particles in *Saccharomyces cerevisiae* using a double-helix point spread function,” *Proc. Natl. Acad. Sci. U. S. A.*, vol. 107, no. 42, pp. 17864–71, Oct. 2010.
- [106] M. Lew, M. A. Thompson, M. Badieirostami, and W. E. Moerner, “Localization Precision of Three-Dimensional Superresolution Fluorescence Imaging Using a Double-Helix Point Spread Function,” in *Frontiers in Optics 2009/Laser Science XXV/Fall 2009 OSA Optics & Photonics Technical Digest*, 2009, p. CThA4.
- [107] R. J. Ober, S. Ram, and E. S. Ward, “Localization accuracy in single-molecule microscopy,” *Biophys. J.*, vol. 86, no. 2, pp. 1185–200, Feb. 2004.
- [108] C. McKenna, K. Walsh, M. Crain, and J. Lake, “Maskless Direct Write Grayscale Lithography for MEMS Applications,” in *2010 18th Biennial University/Government/Industry Micro/Nano Symposium*, 2010, pp. 1–4.
- [109] S. M. Shank, “Multiple-level phase gratings fabricated using focused ion-beam milling and electron-beam lithography,” *J. Vac. Sci. Technol. B Microelectron. Nanom. Struct.*, vol. 12, no. 6, p. 3643, Nov. 1994.
- [110] M. Bass and O. S. of America, *Handbook of Optics: Fundamentals, techniques, and design, Volume 1*. McGraw-Hill, 1994, p. 1664.
- [111] W. T. Plummer, “Unusual optics of the Polaroid SX-70 Land camera,” *Appl. Opt.*, vol. 21, no. 2, pp. 196–208, Jan. 1982.
- [112] W. B. Swanson, Gary J. Veldkamp, “Diffractive Optical Elements For Use In Infrared Systems,” *Opt. Eng.*, vol. 28, no. 6, p. 286605, Jun. 1989.

- [113] S. L. Hurst, *VLSI Custom Microelectronics: Digital, Analog, and Mixed-Signal*, vol. 1998. CRC Press, 1998, p. 496.
- [114] J. B. Pendry, “Negative Refraction Makes a Perfect Lens,” *Phys. Rev. Lett.*, vol. 85, no. 18, pp. 3966–3969, Oct. 2000.
- [115] S. John, “Strong localization of photons in certain disordered dielectric superlattices,” *Phys. Rev. Lett.*, vol. 58, no. 23, pp. 2486–2489, Jun. 1987.
- [116] S. Preble, M. Lipson, and H. Lipson, “Two-dimensional photonic crystals designed by evolutionary algorithms,” *Appl. Phys. Lett.*, vol. 86, no. 6, p. 061111, Feb. 2005.
- [117] A. Ledermann, L. Cademartiri, M. Hermatschweiler, C. Toninelli, G. A. Ozin, D. S. Wiersma, M. Wegener, and G. von Freymann, “Three-dimensional silicon inverse photonic quasicrystals for infrared wavelengths,” *Nat. Mater.*, vol. 5, no. 12, pp. 942–5, Dec. 2006.
- [118] M. Florescu, S. Torquato, and P. J. Steinhardt, “Designer disordered materials with large, complete photonic band gaps,” *Proc. Natl. Acad. Sci. U. S. A.*, vol. 106, no. 49, pp. 20658–63, Dec. 2009.
- [119] T. D. Gerke and R. Piestun, “Aperiodic volume optics,” *Nat. Photonics*, vol. 4, no. 3, pp. 188–193, Feb. 2010.
- [120] R. A. Depine and A. Lakhtakia, “A new condition to identify isotropic dielectric-magnetic materials displaying negative phase velocity,” *Microw. Opt. Technol. Lett.*, vol. 41, no. 4, pp. 315–316, May 2004.
- [121] M. W. McCall, A. Lakhtakia, and W. S. Weiglhofer, “The negative index of refraction demystified,” *Eur. J. Phys.*, vol. 23, no. 3, pp. 353–359, May 2002.
- [122] J. B. Pendry, A. J. Holden, D. J. Robbins, and W. J. Stewart, “Magnetism from conductors and enhanced nonlinear phenomena,” *IEEE Trans. Microw. Theory Tech.*, vol. 47, no. 11, pp. 2075–2084, 1999.
- [123] H.-K. Yuan, U. K. Chettiar, W. Cai, A. V. Kildishev, A. Boltasseva, V. P. Drachev, and V. M. Shalaev, “A negative permeability material at red light,” *Opt. Express*, vol. 15, no. 3, p. 1076, 2007.
- [124] S. Xiao, U. K. Chettiar, A. V. Kildishev, V. Drachev, I. C. Khoo, and V. M. Shalaev, “Tunable magnetic response of metamaterials,” *Appl. Phys. Lett.*, vol. 95, no. 3, p. 033115, Jul. 2009.
- [125] W. Park and Q. Wu, “Negative effective permeability in metal cluster photonic crystal,” *Solid State Commun.*, vol. 146, no. 5–6, pp. 221–227, May 2008.

- [126] Q. Wu and W. Park, "Negative index materials based on metal nanoclusters," *Appl. Phys. Lett.*, vol. 92, no. 15, p. 153114, Apr. 2008.
- [127] J. H. Lee, Q. Wu, and W. Park, "Metal nanocluster metamaterial fabricated by the colloidal self-assembly," *Opt. Lett.*, vol. 34, no. 4, p. 443, Feb. 2009.
- [128] V. A. Tamma, J.-H. Lee, Q. Wu, and W. Park, "Visible frequency magnetic activity in silver nanocluster metamaterial.," *Appl. Opt.*, vol. 49, no. 7, pp. A11–7, Mar. 2010.
- [129] W. Park and Q. Wu, "Optical Frequency Magnetic Activity in Metal Nanocluster Photonic Crystal," *J. Comput. Theor. Nanosci.*, vol. 5, no. 4, p. 7, 2008.
- [130] D. R. Smith and S. Schultz, "Determination of effective permittivity and permeability of metamaterials from reflection and transmission coefficients," *Phys. Rev. B*, vol. 65, no. 19, p. 195104, Apr. 2002.
- [131] "COMSOL Multiphysics®." [Online]. Available: <http://www.comsol.com/>. [Accessed: 20-Mar-2014].
- [132] G. Shvets, "Photonic approach to making a material with a negative index of refraction," *Phys. Rev. B*, vol. 67, no. 3, Jan. 2003.
- [133] V. A. Podolskiy and E. E. Narimanov, "Near-sighted superlens," *Opt. Lett.*, vol. 30, no. 1, p. 75, Jan. 2005.
- [134] G. W. Milton, N.-A. P. Nicorovici, R. C. McPhedran, and V. A. Podolskiy, "A proof of superlensing in the quasistatic regime, and limitations of superlenses in this regime due to anomalous localized resonance," *Proc. R. Soc. A Math. Phys. Eng. Sci.*, vol. 461, no. 2064, pp. 3999–4034, Dec. 2005.
- [135] D. R. Smith, D. Schurig, M. Rosenbluth, S. Schultz, S. A. Ramakrishna, and J. B. Pendry, "Limitations on subdiffraction imaging with a negative refractive index slab," *Appl. Phys. Lett.*, vol. 82, no. 10, p. 1506, Mar. 2003.
- [136] D. Schurig and D. Smith, "Negative index lens aberrations," *Phys. Rev. E*, vol. 70, no. 6, Dec. 2004.
- [137] N. Yu, P. Genevet, M. a Kats, F. Aieta, J.-P. Tetienne, F. Capasso, and Z. Gaburro, "Light propagation with phase discontinuities: generalized laws of reflection and refraction.," *Science*, vol. 334, no. 6054, pp. 333–7, Oct. 2011.
- [138] E. Hecht, *Optics*. Addison-Wesley, 2002, p. 698.
- [139] M. Born and E. Wolf, *Principles of Optics: Electromagnetic Theory of Propagation, Interference and Diffraction of Light*. Cambridge University Press, 1999, p. 952.

- [140] I. Richter, P.-C. Sun, F. Xu, and Y. Fainman, "Design considerations of form birefringent microstructures," *Appl. Opt.*, vol. 34, no. 14, p. 2421, May 1995.
- [141] L. Feng, Z. Liu, V. Lomakin, and Y. Fainman, "Form birefringence metal and its plasmonic anisotropy," *Appl. Phys. Lett.*, vol. 96, no. 4, p. 041112, Jan. 2010.
- [142] L. Peng, L. Ran, and N. A. Mortensen, "Achieving anisotropy in metamaterials made of dielectric cylindrical rods," *Appl. Phys. Lett.*, vol. 96, no. 24, p. 241108, Jun. 2010.
- [143] D. Smith, W. Padilla, D. Vier, S. Nemat-Nasser, and S. Schultz, "Composite Medium with Simultaneously Negative Permeability and Permittivity," *Phys. Rev. Lett.*, vol. 84, no. 18, pp. 4184–4187, May 2000.
- [144] W. Yan, M. Yan, and M. Qiu, "Generalized nihility media from transformation optics," *J. Opt.*, vol. 13, no. 2, p. 024005, Feb. 2011.
- [145] A. Yariv and P. Yeh, "Electromagnetic propagation in periodic stratified media II Birefringence, phase matching, and x-ray lasers," *J. Opt. Soc. Am.*, vol. 67, no. 4, p. 438, Apr. 1977.
- [146] "The Mars Rover Lenses." [Online]. Available: <http://zemax.com/support/knowledgebase/the-mars-rover-camera-lenses>. [Accessed: 25-Mar-2014].
- [147] R. T. Morrison and R. N. Boyd, *Organic chemistry*. Prentice-Hall International, 1992, p. 1279.
- [148] A. H. Sihvola, A. J. Viitanen, I. V. Lindell, and S. A. Tretyakov, *Electromagnetic Waves in Chiral and Bi-Isotropic Media (Artech House Antenna Library)*. Artech Print on Demand, 1994, p. 352.
- [149] J. B. Pendry, "A chiral route to negative refraction.," *Science*, vol. 306, no. 5700, pp. 1353–5, Nov. 2004.
- [150] B. Wang, J. Zhou, T. Koschny, M. Kafesaki, and C. M. Soukoulis, "Chiral metamaterials: simulations and experiments," *J. Opt. A Pure Appl. Opt.*, vol. 11, no. 11, p. 114003, Nov. 2009.
- [151] S. Zhang, Y.-S. Park, J. Li, X. Lu, W. Zhang, and X. Zhang, "Negative Refractive Index in Chiral Metamaterials," *Phys. Rev. Lett.*, vol. 102, no. 2, p. 023901, Jan. 2009.
- [152] Q. Cheng and T. J. Cui, "Reflection and refraction properties of plane waves on the interface of uniaxially anisotropic chiral media," *J. Opt. Soc. Am. A*, vol. 23, no. 12, p. 3203, Dec. 2006.

- [153] Q. Cheng and T. Cui, “Negative refractions in uniaxially anisotropic chiral media,” *Phys. Rev. B*, vol. 73, no. 11, p. 113104, Mar. 2006.